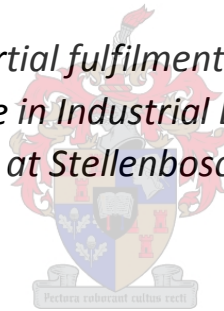# Through Spindle Cooling:

A Study of the Feasibility of Split Tool Titanium Machining

by

C. Prins

This thesis presented in partial fulfilment of the requirements for the degree of Master of Science in Industrial Engineering in the Faculty of Engineering at Stellenbosch University.

Department of Industrial Engineering,
University of Stellenbosch,
Private Bag X1, Matieland 7602, South Africa

Supervisors:

Mnr N.F. Treurnicht

Prof A.F. van der Merwe

March 2015

DECLARATION

I, the undersigned, hereby declare that the work contained in this thesis is my own original work and that I have not previously in its entirety or in part submitted it at any university for a degree.

Signature:

Date: 29-09-2014

ACKNOWLEDGEMENTS

OPSOMMING

Doeltreffende masjinering van titaan allooie bied `n wêreldwye uitdaging. Moeilik-om-te-sny super allooie soos Ti-6Al-4V word as die "werksesel" materiaal vir lugvaart komponente beskou. Gedurende die masjinering van lugvaart komponente word 80% - 90% van die materiaal verwyder. Dit is hiérdie behoefte wat die innovering van masjien -en snygereedskap dryf om dit meer doeltreffend en finansieël vatbaar te maak. Die Suid Arikaanse behoefte vir doeltreffende snygereedskap vir Ti-6Al-4V masjinering stem ooreen met hierdie internationale behoefte. Die geskiedkundige Suid Afrikaanse praktyk om onverwerkte, waardevolle minerale soos Ilmeniet, rutiel en leucoxene uit te voer, kniehalter die land se kans om winste uit verwerkte titaan allooi produkte te geniet. Die "Titanium Centre of Competence" (TiCoC) se mikpunt is om `n Suid Afrikaanse titaanproduk vervaardigingsmark op die been te bring teen 2020. Stellenbosch Universiteit se funksie, binne hierdie strategiese raamwerk, fokus op hoë spoed masjinering van Ti-6Al-4V lugvaart komponente.

Die hitte geleidingsvermoë van Ti-6Al-4V is noemenswaardig laer as die van ander "werksesel" materiale soos byvoorbeeld staal of alumium. Om hierdie rede word hitte in die freesbeitelpunt gedurende hoë spoed masjinering opgeberg. Dit verkort gereedskap leeftyd en verhoog masjinerings kostes. Daarvandaan deurlopende ontwikkelinge in verkoelingsmetodes vir hoë spoed masjinering. Die mees onlangse ontwikkeling in hoë druk verkoeling is "split tools" wat koelmiddel na die snyoppervlak deur middel van langwerpige gleufies in die hark gesig van die beitelpunt lewer. Hierdie tegnologie is op die mark beskikbaar, maar slegs deur `n enkele verskaffer. Daar is ook geen akademiese publikasies wat oor Ti-6Al-4V masjinering met "split tools" handel nie. Die verrigtings vermoë en toepassings gebied vir die gereedskap is steeds onbekend.

'n Dinamometer is gebruik om die tangensiale snykragte tydens 11 sny eksperimente te meet. Die eksperiment ontwerp is faktoriaal van aard en bevat drie faktore en drie middelpunte oor twee vlakke. `n Kwadratiese model is geskik om die data op 95% vertroue vlak voor te stel en voorspellings mee te maak. Die voorspellingsmodel is ontwikkel in terme van: (1) Diepte van snit, (2) voertempo, en (3) Snyspoed. Die invloed van die drie parameters op die tangentiale snykrag, asook invloed met mekaar word ondersoek. Verdere data in verband met materiaal verwydering, oppervlak afwerking en beitel slytasie word ook bespreek.

Praktiese werk is met behulp van `n bedryfsvennoot gedoen om vas te stel: (1) die impak van 'n analitiese benadering en ontwikkelings proses op die uitrof van lugvaart komponente, (2) en om die lewensvatbaarheid van implementering van "split tools" aan 'n bestaande proses te bepaal. `n Noemenswaardige besparing is sodoende behaal. Dit is verder bevind dat "split tools" nie `n geskikte plaasvervanger vir die huidige snygereedskap is nie. Die rede daarvoor is gedeeltelik omdat die huidige

OPSOMMING

freesmasjien by die bedryfsvennoot nie aan die kritiese operasionele vereistes van die gereedskap vervaardiger voldoen nie.

ABSTRACT

Efficient face milling of titanium alloys provides a global challenge. Difficult-to-cut super alloys such as Ti-6Al-4V is considered the "workhorse" material for aerospace components. During the machining of aerospace components, 80% – 90% of the material is removed. This requirement drives the innovation for machines and tooling to become more efficient, while driving down costs. In South Africa, this requirement is no different. Due to the historic practice of exporting valuable minerals such as Ilmenite, leucoxene and rutile, South Africa does not enjoy many of financial benefits of producing value added titanium alloy products. The Titanium Centre of Competence (TiCoC) is aimed at creating a South African titanium manufacturing industry by the year 2020. More specifically, the roughing of Ti-6Al-4V aerospace components has been identified as an area for improvement.

The thermal conductivity of Ti-6Al-4V is significantly lower than that of other "workhorse" metals such as steel or aluminium. Therefore, heat rapidly builds up in the tool tip during high speed machining resulting in shortened tool life and increased machining costs. Hence the ongoing developments in the field of cooling methods for high speed machining. The latest development in high pressure cooling (HPC) is split tools that deliver coolant into the cutting interface via flat nozzles in the rake face of the insert. Although it has been released recently and limited to a single supplier, this cooling method is commercially available, yet little is known about its performance or application conditions.

The operational characteristics of split tools are studied by answering set research questions. A dynamometer was used to measure the tangential cutting forces during 11 cutting experiments that follow a three-factor factorial design at two levels and with three centre points. A second-order model for predicting the tangential cutting force during face milling of Ti-6Al-4V with split tools was fit to the data at 95% confidence level. A predictive cutting force model was developed in terms of the cutting parameters: (1) Axial depth of cut (ADOC), (2) feed per tooth and, (3) cutting speed. The effect of cutting parameters on cutting force including their interactions are investigated. Data for chip evacuation, surface finish and tool wear are examined and discussed.

Practical work was done at a selected industry partner to determine: (1) impact of an analytical approach to perform process development for aerospace component roughing, (2) determine the feasibility of implementing split tools to an existing process. A substantial time saving in the roughing time of the selected aerospace component was achieved through analytical improvement methods. Furthermore it was found that the split tools were not a suitable replacement for current tooling. It was established that certain critical operational requirements of the split tools are not met by the existing milling machine at the industry partner.

TABLE OF CONTENTS

TABLE OF CONTENTS

TABLE OF CONTENTS

LIST OF FIGURES

LIST OF FIGURES

LIST OF TABLES

LIST OF ACRONYMS

ANOVA	Analysis of Variance
a_p or ADOC	Depth of Cut
BUE	Built-up Edge
CAM	Computer-aided Manufacturing
CF	Catastrophic Failure
CH 1	Uniform Chipping
CH 2	Non-uniform Chipping
CH 3	Localized Chipping
CH 4	Chipping of the non-active part of the major cutting edge
CR 1	Comb Cracks
CR 2	Parallel Cracks
CR 3	Irregular Cracks
CV	Coefficient of Variation
DAQ	Data Acquisition System
DF	Degrees of Freedom
DOS	Direct Oil Drop Supply System
DST	The Department of Science and Technology
FEM	Finite Element Method
$FeTiO_3$	Ilmenite
FL	Flaking
f_z	Feedrate/Feed per Tooth
HPC	High Pressure Cooling
HPE	High Pressure Emulsion
HPTSC	High Pressure, Through Spindle Cooling
HPTSC-ST	High Pressure, Through Spindle Cooling with Split Tool Inserts
KT 1	Crater Wear
KT 2	Stair-formed Face Wear
LAM	Laser Assisted Machining
LN_2	Liquid Nitrogen
LN_2/MQL	Cryogenic Through Spindle, Through Tool Cooling
MQL	Minimal Quantity of Lubricant
MRR	Material Removal Rate
MS	Mean Square
MSE	Mean Square Error
PD	Plastic Deformation
PRESS	Prediction Error Sum of Squares
Ra	Surface Roughness
RSM	Response Surface Methodology
SS	Sum of Squares

LIST OF ACRONYMS

TiAlN	Titanium Aluminium Nitride
TiCoC	Titanium Centre of Competence
TiO$_2$	Rutile
VB	Flank Wear
VB 1	Uniform Flank Wear
VB 2	Non-uniform Flank Wear
VB 3	Localized Flank Wear

CHAPTER 1

INTRODUCTION

1.1 THE SOUTH AFRICAN TITANIUM CENTRE OF COMPETENCE

South Africa is the world's second largest producer of the titanium bearing minerals, Ilmenite ($FeTiO_3$) and Rutile (TiO_2) as it contributes 18% of the global supply. Geological surveys estimate that South African titanium mineral deposits constitute 11% of global reserves [1]. Despite the regional abundance of this precious mineral, South Africa does not necessarily benefit from downstream profits. South Africa manufactures negligible volumes of finished titanium metal products, when compared to world production leaders such as China, Japan, Russia, United States, Ukraine and Kazakhstan [2].

Henceforth, in 2003, the South African Government accepted an Advanced Manufacturing Technology Strategy, proposed by The Department of Science and Technology (DST). A feasibility study conducted by the DST in 2008, generated confidence in a national strategy that aims to establish a South African titanium manufacturing industry by the year 2020. As a result the TiCoC was established to determine building blocks for the realisation of this strategy [3]. The DST funds technology development and research for the TiCoC strategy in proportion according to Figure 1.
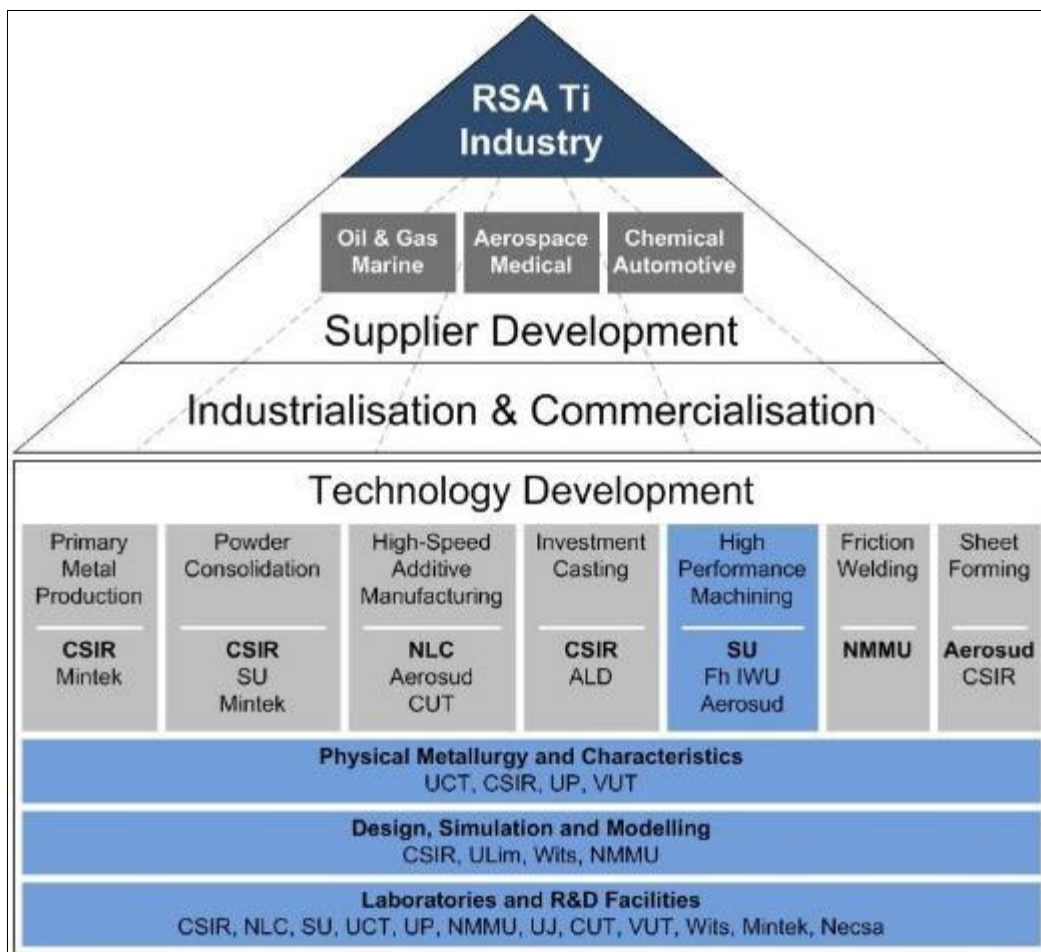
Figure 1: Titanium Centre of Competence [3]

CHAPTER 1: INTRODUCTION

Stellenbosch University's research contract with DST involves a research framework that focuses on high performance machining and incorporates a number of local industry partners. This arrangement is aimed at applying the research results to add value to the titanium industrial partner. The Department of Industrial Engineering at Stellenbosch University maintains a co-beneficial relationship with Daliff Engineering, that is situated in Cape Town's Airport Industrial area, as one of the partners. This relationship promotes a research and development platform that draws from industry and academic inputs.

The TiCoC building blocks define the role of Stellenbosch University within the 2020 strategy: Develop high performance machining methods for industry and commercial benefits. Tool life and accompanying costs are currently some of the biggest challenges in the titanium machining industry. Novel manufacturing techniques that have not been used on a commercial level in South Africa are researched and expanded. Research knowledge is shared with industry in order to facilitate the broader strategy of the DST for the year 2020. In conclusion, there is an inherent opportunity for Stellenbosch University to further develop its involvement with regards to research contribution to the South African Industry.

1.2 BACKGROUND

The price of titanium can be up to nine times more than steel due to a considerably more demanding process from ore to component [4]. Melting is done in either a vacuum or an inert atmosphere at nominally 1600 degrees Celsius compared to steel melting at nominally 1500 degrees Celsius in a normal atmosphere environment [5] [6]. Similarly machining properties are also challenging, classifying titanium as a difficult to machine super alloy [7].

These properties cause cutting tools to overheat and fail after only a few minutes of high performance machining, potentially resulting in extended changeover time and increased tool cost [8] [9]. Recent technological advancements, specifically the combination of high pressure, through spindle cooling (HPTSC) and split tools, claim to provide vast machining improvements [10] [11].

1.3 INDUSTRY PRACTICE AND PREVIOUS STUDIES

HPTSC, in combination with cryogenic cooling is currently being successfully applied in aerospace industry. Although some research papers have been published on cryogenic, through spindle cooling it is common to find manufacturers implementing technologies that are on a more advanced level than those published in open, academic literature [12] [13]. This is due to the limitations on intellectual property within the industry. As a result, unique specialist applications are kept secret for as long as possible by manufacturing technology companies.

In terms of research, previous studies conducted in this field have proved that HPTSC provides improvements in tool life due to a reduction in tool wear over time [9]. Still, increasing cooling in titanium machining can result in negative effects of tool wear, such as thermal shock and chip adhesion to the tool

surface [9]. These are important factors that have not been researched in depth in articles or publications relating to industry practice, yet need to be taken into account for the purpose of determining overall feasibility.

Split tooling is a recent development and an example of second generation derivative technologies that followed after the success of HPTSC. Indications are that the early adopters are embracing the technology, but no scientific results are being released [14].

1.4 PROBLEM STATEMENT

The feasibility and application conditions of split tool technology needs to be explored for the South African titanium component manufacturing industry to enable competitiveness on an international level.

1.5 RESEARCH OBJECTIVES AND QUESTIONS

The purpose of this research project is to determine whether split tooling can benefit existing titanium manufacturing operations. The study objective involves the establishment of a machinability index or model, which aids in the transfer of information to the industry partner. A machinability model has certain requirements that have to be met, thus certain machining productivity and quality related questions need to be answered:

1.5.1	Can tangential cutting forces for Ti-6Al-4V split tool milling be predicted by a model?
1.5.2	What are the significant factors affecting cutting forces during experiments?
1.5.3	Are split tools able to perform semi finishing of Ti-6Al-4V during face milling?
1.5.4	What types of tool failures are characteristic during split tool milling of Ti-6Al-4V?
1.5.5	Can Ti-6Al-4V machining productivity be enhanced by the application of analytical techniques?

1.6 RESEARCH ROADMAP

The introduction, problem background, problem statement and research objectives are discussed in this chapter. The literature review commences with chapter two and provides an overview of cooling techniques. Conventional cooling methods such as flood cooling, HPC, near dry machining, liquid nitrogen (LN$_2$) cooling and high pressure through spindle cooling (HPTSC) as well as advancements in industry solutions such as cryogenic through spindle, through tool cooling and through spindle cooling with split tools are covered.

The literature review continues with chapter three and discusses the factors contributing to the machinability of titanium alloys during face milling. Factors such as surface finish and integrity, chip control, tool wear, cutting forces and tool geometries are explained in terms of their measurement criteria. In addition, specific considerations for face milling and inherent complexities associated with the modeling of milling systems are considered.

CHAPTER 1: INTRODUCTION

Chapter four describes the methodology followed for the face milling experiments. The machine tool, milling tool and insert specifications and cutting strategy are explained. Material characteristics are determined by means of testing and the statistical experiment design is discussed. This chapter includes an in-depth design of the face milling experiments, according to the ISO standards for tool life testing in end milling and face milling.

Chapter five evaluates experiment results and proceeds with the modeling of tangential cutting forces. The suitability of a first and second-order model is determined, based on each model's prediction ability at the 95% confidence level and the interactions of cutting parameters on tangential cutting force are shown. The response surface for the model is explored. Additional experimental results from surface finish measurements, tool wear inspection and chip formation are discussed at the end of the chapter.

Chapter six is a detailed report on the application of a nonlinear program approach to contribute productivity savings at the selected industry partner. The cutting parameters for an existing cutting process were examined. Experiments were conducted with new parameters from the nonlinear program and results interpreted with the aid of microscope analysis of the inserts. The split tool was also implemented during this project.

Chapter seven concludes the study by determining whether the research objectives were met in terms of the results from experiments, industry partner work and the predictive cutting force model.

CHAPTER 2

OVERVIEW OF ADVANCED COOLING TECHNIQUES FOR TITANIUM ALLOY MACHINING IN AEROSPACE APPLICATIONS

2.1 INTRODUCTION

The most common and extensively studied cooling strategies are dry cutting, flood cooling, HPC, and HPTSC; the strategy and technique used depends on the material and parameters surrounding the machining process.

Recent advances in cooling technology for aerospace manufacturing, specifically the combination of HPTSC and split tools, are claimed to yield improved machining productivity for difficult-to-cut materials.

New advancements are highly specialised as they are usually made in-house by means of a partnership between the manufacturer and the tool supplier with a high premium on confidentiality. The cooling methods are designed for specific applications within the production process and usually comprises a finely tuned hybrid between some of the aforementioned conventional cooling systems.

2.2 OVERVIEW OF CONVENTIONAL COOLING METHODS

2.2.1 Flood Cooling

Flood cooling with soluble oil is widely used in industry. Flood cooling, best described as an uninterrupted flow of an abundant quantity of coolant, from a source external to the tool, cools the tool and removes chips by a flushing action. With flood cooling, thermal shock on milling tools are minimised, and the ignition of chips is eliminated [9].
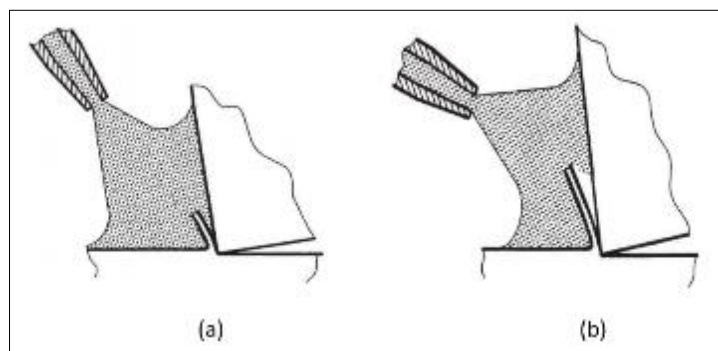
Figure 2: Extreme directional effects of flood cooling [15]

This method is often a benchmark for experiments due to its extensive use in standard machining applications. Flood cooling is inadequate in some cases, one of which is titanium alloy machining.

Flood cooling is not based on the principle of precise directional application of the coolant stream. Two extreme cases are shown in Figure 2. In the most extreme case, where the titanium alloy's short contact

area between chip and tool is approximated, the chip prevents the coolant from being applied to the tool chip interface (b). The cutting edge therefore experiences a large thermal load resulting in poor tool life [8].

2.2.2   High Pressure Cooling (HPC)

HPC became the standard in industry as soon as flood cooling methods were found less effective for high speed machining of hard metals. During high speed machining the performance levels of modern machinery generate so much heat that normal flood cooling is unable to remove chips quick enough and pierce through the vapour barrier. Long, thick and unmanageable chips form, as result [16].

The Leidenfrost phenomenon can be observed in cases where a vapour barrier is formed. In Figure 3, Bernardin and Mudawar's time based graph for initial vapour barrier formation versus time is depicted [17].
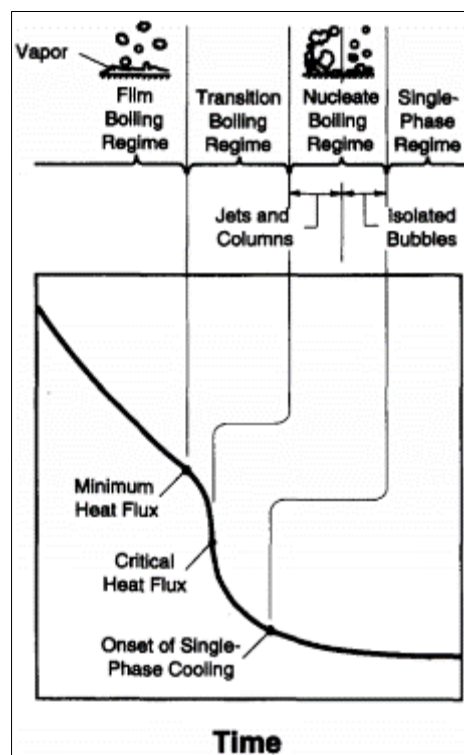
Figure 3: Boiling regimes associated with bath quenching a small metallic mass [17]

This initial barrier "film boiling regime" prohibits the flood coolant to come into contact with the hot tool-chip interface as the vapour barrier persists [16] [17] [18]. Penetration and removal of the vapour barrier is only achieved through high pressure nozzles to direct coolant at the hot surface. High pressure cooling also enables the formation of short chips, which prohibits the re-cut of chips, thus increasing tool life [16].

Ezugwu [19] found that high pressure cooling demonstrates the potential for improvements in tool life when machining Ti-6Al-4V with carbide (coated and uncoated) tools at higher cutting speeds. Figure 4 shows notable tool life extension under HPC, compared to flood cooling methods [19]. Particular attention to the greater potential of the HPC over flood cooling, referred to as conventional cooling in Ezugwu's

work, should be noted, specifically at higher cutting speeds. Tool life usually increases with higher coolant pressures as the cutting speed increases [19].
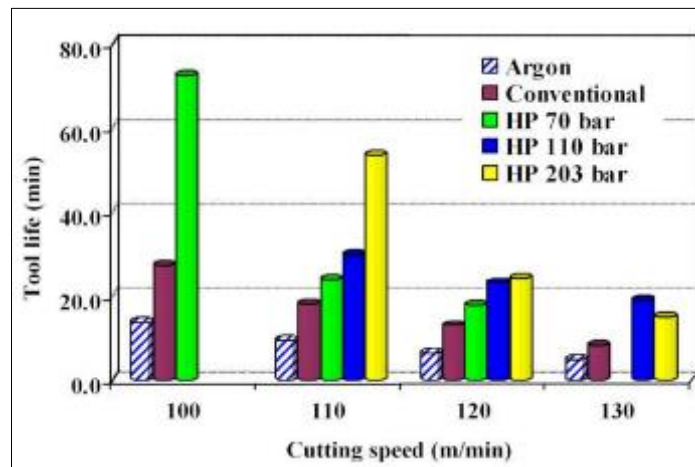
Figure 4: Tool life during Ti-6Al-4V machining with uncoated tungsten carbide [19]

At a cutting speed of 110 m/min (Figure 4) a pressure of 203 bar yields approximately double the tool life of 70 bar pressure. It also results in a three times increase in tool life compared to flood cooling. At 110 m/min, there is a noticeable difference in tool life when comparing 110 bar and 203 bar cooling is. However, at 120 m/min the difference between tool life for 110 bar and 203 bar pressures is less than 5%. Also, at 130m/min, 110 bar pressure delivers better tool life than 203 bar pressure [19]. These results therefore question the supposed direct relationship between pressure and cooling effectiveness.

2.2.3   Near Dry Machining with Oil Based Lubricants (MQL and DOS)

As industry moves toward greener manufacturing processes, the minimal quantity of lubricant technique (MQL) is being implemented in cases where the waste oil by-product of machining is undesirable [20] [21] [22]. The minimal quantity of lubricant technique implements a pressured air nozzle to deliver a small amount of oil mist to the cutting surface thereby substantially reducing the amount of cutting fluid required for machining operations.

In an attempt to improve the current minimal quantity of lubricant technique, Aoki, Aoyama, Kakinuma, and Yamashita [23] argue that it has two major disadvantages for consideration: Due to the absence of the hydraulic pressure of pressurised coolant, the chip removal ability of the minimal quantity of lubricant technique is practically non-existent. Furthermore, the minimal quantity of lubricant technique results in the work area being covered in oil. The oil mist causes machine problems, slippage on affected surfaces and inhalation of hazardous fumes [23].

Aoki et al. [23] proposes an improved system: "Direct Oil Drop Supply System (DOS)", to counteract the oil mist problem of the minimal quantity of lubricant technique. During the operation of this system, pressurised oil drops are supplied to the nozzle via a 0.4 MPa gear pump.
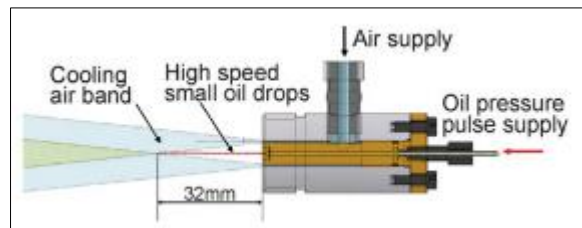
Figure 5: Structure of nozzle for DOS system [23]

Compressed air is also exhausted from the circular slit surrounding the oil discharge hole in order to direct the oil mist to the cutting surface. The pressurised air serves both as chip removal mechanism and also contains the oil drops inside a high speed air barrier. During experimentation it was found that the nozzle in Figure 5 did not deliver oil to the entire cutting surface effectively, consequently a second derivate nozzle was designed.
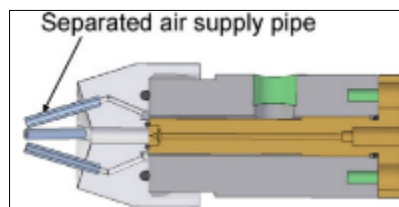
Figure 6: Revised DOS nozzle design [23]

The subsequent design (Figure 6) comprises four small air flow pipes to deliver air flow to the cutting point more directly while still separating the oil and air. The oil delivery nozzle is located in the centre of the four surrounding air supply nozzles.

Figure 7 illustrates the measured temperatures at the cutting surface for Ti-6Al-4V with a 10mm Carbide square end mill. Cutting speed set at 150m/min, ADOC 6mm and radial ADOC at 0.5mm. Results indicate little difference in temperature between the minimal quantity of lubricant technique and the direct oil drop supply system. Aoki et al. reported an 80% reduction in oil mist diffusion around the machine [23].
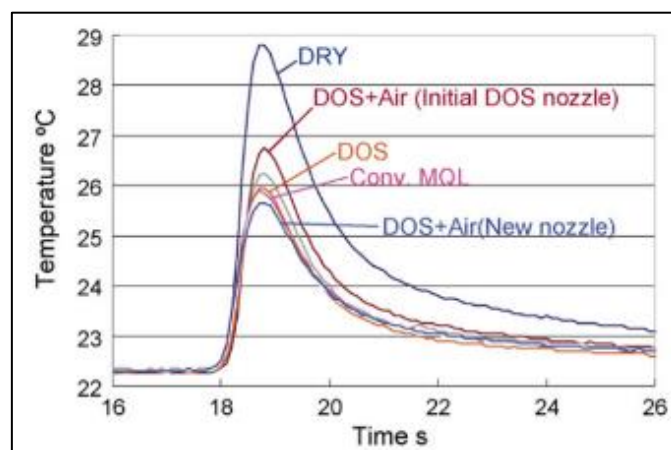
Figure 7: Behaviour of cutting temperature related to cooling method [23]

Liu WD, Liu Q, Yan, and Yuan [24] found that although the MQL technique significantly reduces cutting force, tool wear and surface roughness, it cannot produce an evident effect on cutting performance. As a result flaking wear on the flank surface of the insert was found under certain experimental conditions.

Another major disadvantage of this experimental technology is the degree of customization that is required to install a MQL technique system or DOS. Due to a high level of customization to existing equipment, machine setups can be complex and costly.

2.2.4 Liquid Nitrogen Cooling (LN$_2$)

LN$_2$ as a coolant has been used in a number of studies. In certain cases, it has been conclusively proven that when utilised correctly; it improves tool life, surface finish and dimensional accuracy [15] [25] [26].

Kaynak [26] experimented on a lathe with cryogenic cooling and found that machining performance is improved when the amount of coolant nozzles directed at the workpiece is increased. As a result of this approach, tool wear was reduced, lower machining temperature achieved and better surface quality was measured.

Furthermore, Rajurkar and Wang [27] compared conventional cooling and LN$_2$ cooling during turning of Ti-6Al-4V for a cutting speed of 132m/min^{-1}, feedrate of 0.2 mm/rev^{-1} and ADOC of 1 mm. Experiment results indicated that with conventional cooling, flank wear was increased five times as compared to LN$_2$ cooling.

In contrast to this, Gowrishankar, Nandy, and Paul (2008) [28] found that HPC outperformed LN$_2$ cooling by two fold when comparing tool wear. Further experiments by Bermingham, Dargusch, Kent, and Palanisamy (2011) [29] supports the findings of Gowrishankar et al.

Although Bermingham et al. and Gowrishankar et al. found that HPC resulted in improved performance over LN$_2$ cooling, improvements are marginal. Turning of Ti-6Al-4V is used as comparison for all three experimental sets. The discrepancies between the respective findings can be attributed to differences in coolant delivery mechanisms.

Bermingham et al. [29] experimented with four different coolant delivery systems (Note D1-4 postfix for tests in Figure 8):

- (D1) Coolant delivered to the tip of tool through nozzles on standard Jetstream tool holder;
- (D2) same as (D1) with added nozzle directing coolant to primary flank;
- (D3) standard nozzles in Jetstream are sealed and all coolant is delivered through three aftermarket nozzles directing coolant to the primary flank, the tool nose and the rake face;
- (D4) same as D2 with added nozzle underneath tool directing coolant onto the tool nose.

Results differ noticeably at 125m/min where the "LN" datasets show a clear departure from high pressure emulsion (HPE) and "dry" results in terms of tool life.
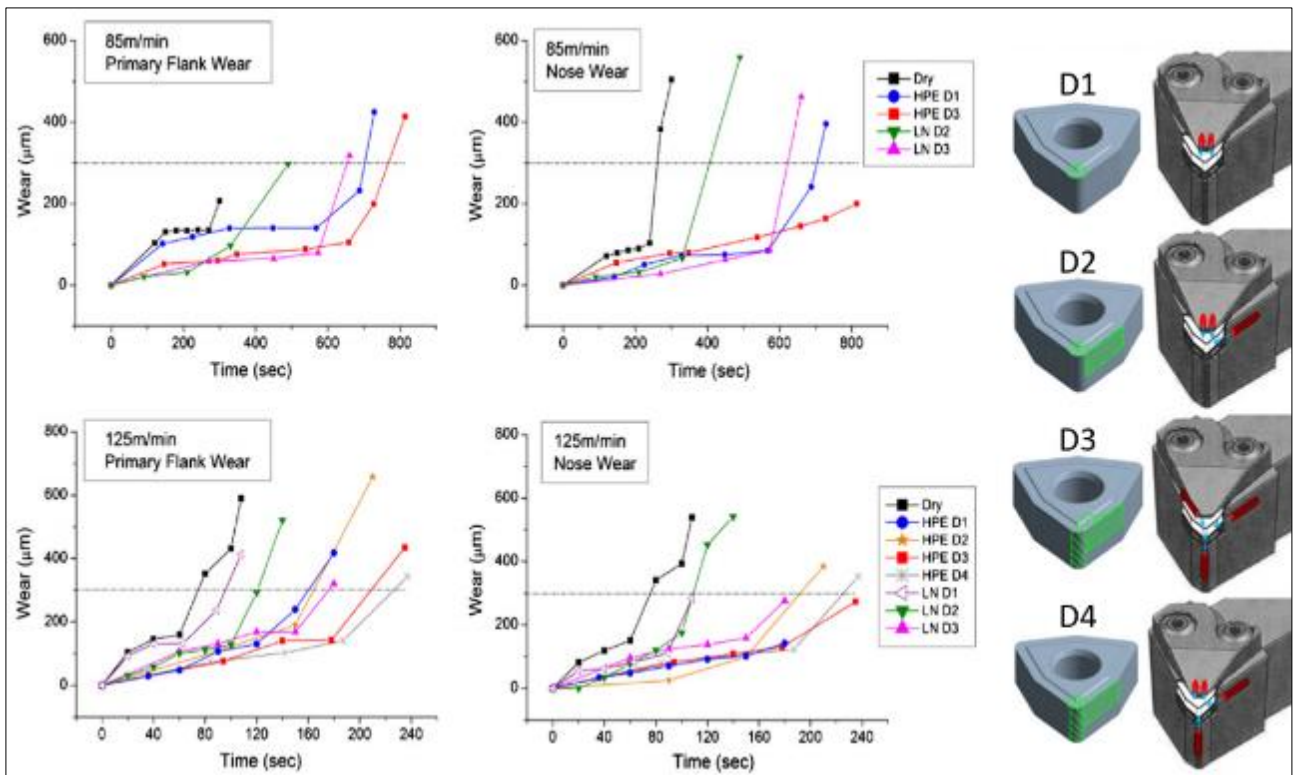
Figure 8: Flank and Nose wear during turning of Ti-6Al-4V [29]

LN_2 cooling reduces tool wear during higher speed turning operations (125m/min) while performing marginally inferior to HPC at lower machining speeds [27] [28] [29]. Evidence therefore suggests that there are high speed application possibilities for LN_2 cooling.

2.2.5   High Pressure, Through Spindle Cooling (HPTSC)

HPTSC has been used since 1994, when it was first patented by Chang, Chen, Du, Hsu, and Lin [30]. This 20 year old technology directly led to the removal of the external cooling pipe and nozzle in the design of modern high pressure cooling systems. HPTSC is available for milling, drilling and turning applications as shown in Figure 9.
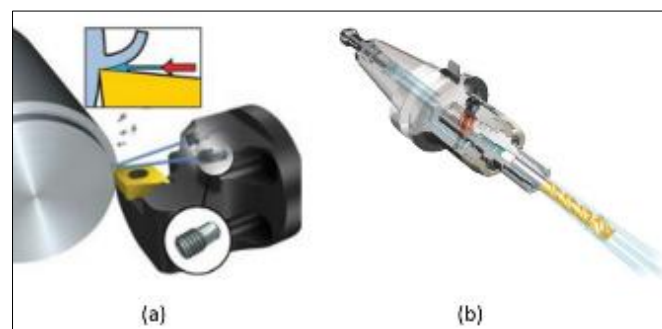
Figure 9: (a) CoroTurn HPTSC for turning. (b) HPSTC application for Hyundai's drilling tool body

During HPTSC, coolant is delivered to the work surface through a channel inside the tool clamp and/or cutter body. The coolant is directed at the workpiece through minute nozzles, mounted close to the insert [16].

At first glance, HPTSC seems complex and costly to implement. Tool manufacturers maintain that it provides unsurpassed advantages: Rapid tool changes, better chip control, increased tool life for difficult to machine materials, 50% increase in cutting capability at the same cutting parameters (v_c, a_p, f_z) and 20% cutting speed increase for aerospace materials such as titanium and nickel alloys [16].

Ezugwu [19] performed a number of milling experiments in order to compare HPC with HPTSC. During the experiments, single layer coated, multi-layer coated and uncoated inserts were compared for both cooling methods. It was found that when coated tungsten carbide cutting tools are used, improvements in flank wear under the concept of high pressure through spindle cooling are realised.

Experiments indicate that the multi layered coating performance is the lowest and shows no benefit from pressurised cooling or high pressure through spindle cooling. Uncoated inserts showed clear benefit from high pressure through spindle cooling, yielding considerably lower values of uniform wear during the earlier part of the insert's life.

2.2.6   Cutting Fluids

Cutting fluids, in general, serve two major roles in machining namely cooling and lubrication [31] [32]. The flow of cutting fluid also aids in the removal of chips, minimise thermal shock in milling operations and keeps chips from igniting. When high pressure cooling methods are used, chips are often small and discontinuous as shown in Figure 10.

Cutting fluids can be divided into three major categories: neat cutting oils, soluble oils and gaseous cooling. Each of these categories have their own characteristic application. Neat cutting oils are mineral oils that may contain additives and are primarily used when the pressures between the tool and chip are high and when lubrication is a primary concern. Water soluble coolants are suitable when cutting speeds are high and tool pressures are low. It has been found, that cutting fluids do not penetrate the tool-chip interface when cutting speeds are high [32]. Here gaseous coolants can be utilised to overcome coolant penetration difficulties, but the high cost of gases does limit their use.

When a workpiece is overcooled it becomes harder and tougher, resulting in reduced tool life [33]. Overcooling can also deteriorate the surface finish and dimensional accuracy of the workpiece in severe cases.

Cutting fluids may cause environmental, health and logistical problems. Typical environmental problems are chemical breakdown resulting in water and soil contamination. Operators may experience

dermatological ailments due to prolonged exposure. Government regulations are strict about disposal procedures, resulting in high transportation costs to disposal sites [15].
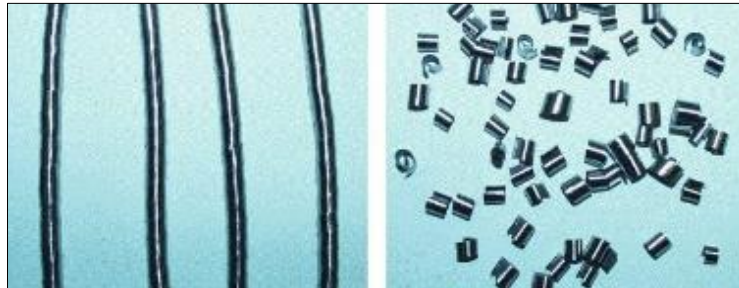
Figure 10: Long continuous and short, discontinuous chips

Nitrogen composes approximately 78% of our earth's atmosphere, and because LN_2 evaporates to nitrogen gas when used, it is considered environmentally friendly [19] [15] [25]. No operator ailments have been reported with regard to nitrogen. Nevertheless, displacement of normal oxygen rich air in semi-confined spaces such as machine shops are a risk for operator safety.

2.2.7   Specialised Cooling: Cryogenic Through Spindle, Through Tool Cooling (LN_2/MQL)

In 2010, MAG announced LN_2/MQL cooling system, that comprises an internally developed system that combines LN_2 cooling with HPTSC for machining of difficult-to-cut materials. Marketing media may indicate *what* is being accomplished by these new technologies, but not *how* these processes precisely work. Conversely, as is the case with MAG, these technologies are slowly making their way to the market [34].
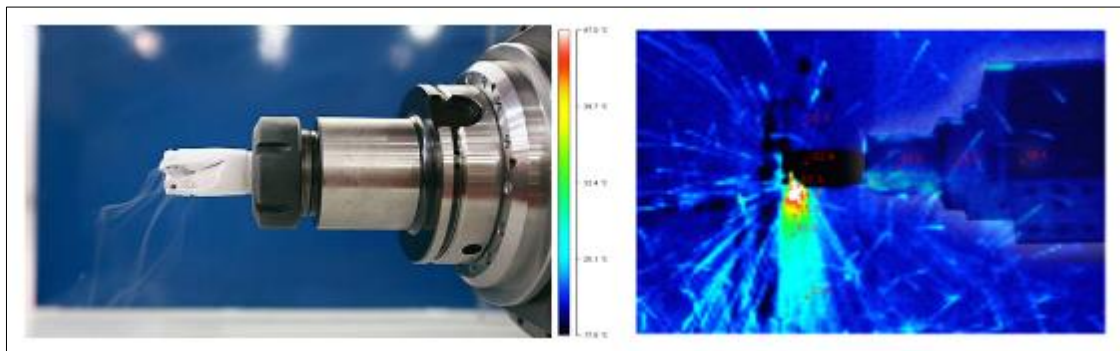
Figure 11: Cryogenic/MQL and through spindle cooling system with thermograph [34]

Figure 11 thermo-graphically depicts the hottest and coldest areas on the tool/workpiece interface. The measured temperature for the cutter is -32°C, while the hottest area is measured to be 82°C. MAG's LN_2/MQL system concentrates the cooling in the body of the cutter. Early in-house experimental tests found that through tool cooling provides the most efficient heat transfer model for LN_2 and consumes the least amount of the coolant gas. MAG claims a four times increase in processing speed for milling compacted graphite iron with Polycrystalline Diamond inserts. LN_2/MQL cooling is claimed to provide twice the tool life, compared to conventional MQL. The benefits for this cooling technology are listed as: no mist collection, no filtration required due to the absence of wet chips, workpieces aren't contaminated and

therefore disposal cost is reduced. LN_2 is a pressured gas, which is self-propelled and therefore eliminates the need for coolant pumps and fans [34].

In terms of academic publications, Jeong, Lee, DY, Lee, MG, Lee, SW, Park, and Yang (2014) [12] recently published experiment results based on LN_2/MQL cooling for a milling process. The machining performance during flood cooling, dry machining, conventional MQL, laser assisted machining (LAM), LN2 cooling and LN2/MQL were compared. A dynamometer was attached to the milling machine for the measurement of cutting forces. Experimental results indicate that the cutting forces for LN_2/MQL cooling was the lowest of all techniques tested at high machining speeds as shown in Figure 12.
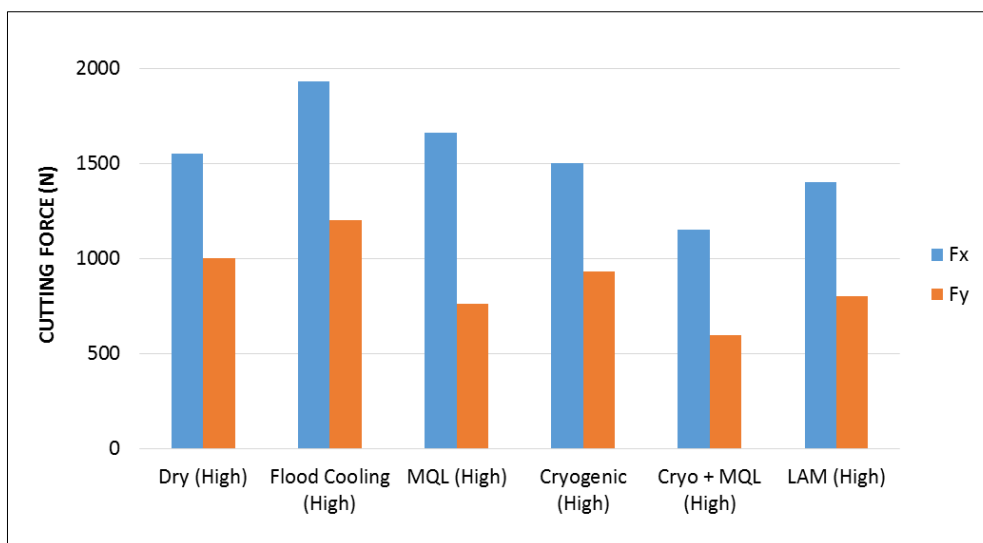
Figure 12: Cutting forces during high speed experiments with different cooling methods [12]

Conversely, LN_2/MQL cooling performance is reduced under low speed machining. Other techniques such as flood cooling and conventional MQL were more effective in terms of the resultant cutting forces. Furthermore, it was found that cryogenic/MQL cooling reduces tool wear most, compared to the other cooling techniques.

2.2.8   Specialised Cooling: HPTSC with Split Tool Inserts (HPTSC-ST)

HPTSC-ST was pioneered during an innovative development project in 2010 by Kennametal. Tools with HPTSC-ST technology are also referred to as "Beyond Blast" tools. This innovation followed Boeing's pre 2010 market research for their 787 manufacturing purposes that concluded that there would not be enough titanium alloy machining capacity in the world during peak requirement for the new 787's. This high demand is related to the requirement that 80% - 90% of the material of titanium alloy components is machined away for aerospace parts [11].

HPTSC-ST technology is different to LN_2/MQL, in two major ways; the type of coolant that is utilised and the delivery mechanism. HPTSC-ST can be implemented using existing water based HPC, while LN_2/MQL cooling

specifically requires LN$_2$. HPTSC-ST cooling is designed so that the coolant ejects through the insert rake face (Figure 13), while LN$_2$/MQL cooling uses a more traditional HPTSC delivery mechanism.
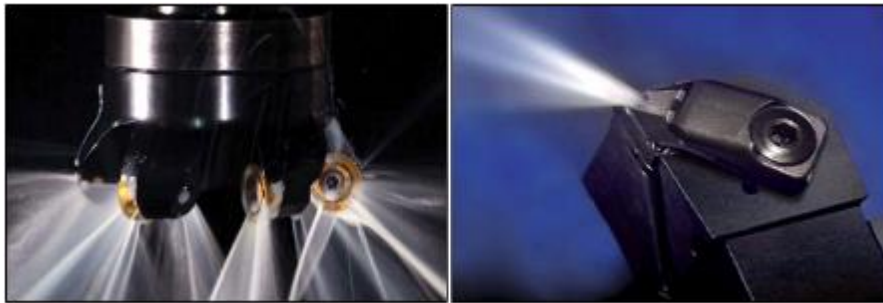
Figure 13: HPTSC-ST for both milling and turning applications [10]

It is claimed that HPTSC-ST cooling offers a cost reduction over conventional HPC methods, due to the insert that directs the coolant precisely where it is needed [10].

Cooling applications often miss the highest heat concentration location, generated at the shearing point (Figure 14). Impacting chips after they have formed proves typical cooling applications can even force chips back into the cut, accelerating tool wear. Part of the challenge is that the coolant-delivering nozzle is located relatively far from the workpiece.

With a split tool delivery system (Figure 14 (b)), coolant is delivered through the insert, at the cutting interface. Consequently, coolant is delivered much closer to the shear point, causing the pressure to remain stable. Delivery is therefore more reliable and controlled, significantly reducing temperatures at the point of the cut. The precision cooling technology assists in chip removal by hydraulically lifting chips out of the cut. This is known as chip lifting [10].
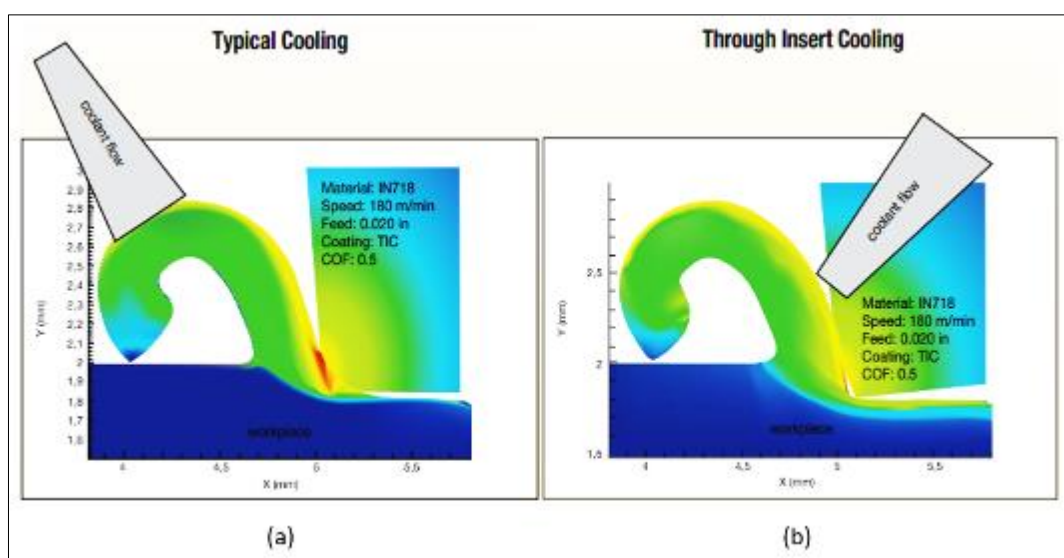
Figure 14: Thermograph for turning with typical cooling (a) vs. through insert cooling (b) [10]

HPTSC-ST tools for face milling applications are specifically aimed at large material removal rates. The Kennametal KSRM tools uses round insert split tool technology with HPTSC. The cutter bodies have up to eight positions for indexable inserts. The inserts are channelled to precisely direct the flow of coolant into the cutting interface, where it helps with chip lifting, chip removal, lubrication, and increased heat transfer as shown in Figure 15.
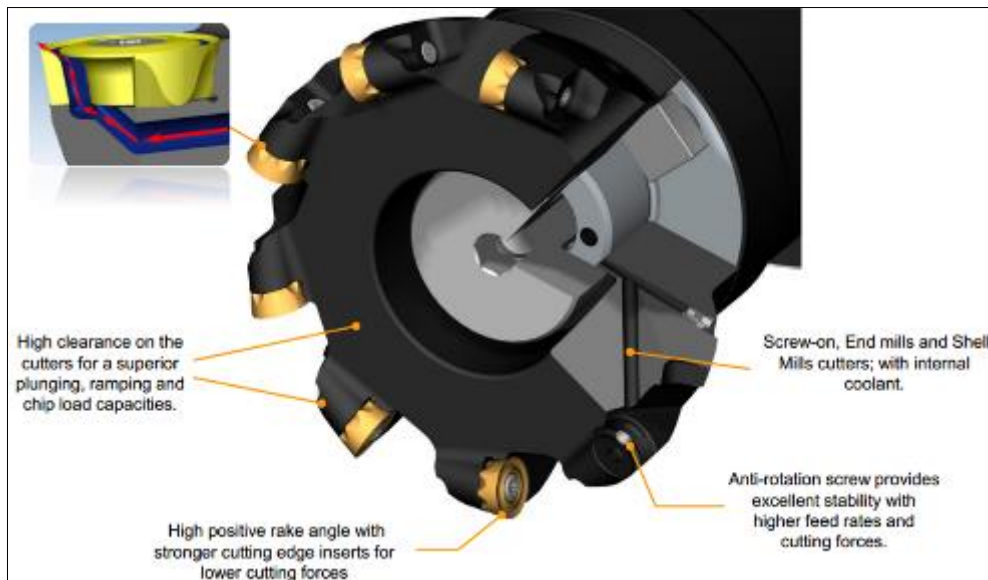
Figure 15: KSRM features and benefits [10]

The Beyond Blast cutter body (split tooling) is benchmarked with T114526 and T117470 inserts, specifically designed for heavy roughing of Ti-6Al-4V and other difficult-to-cut materials. Some cutting experiments from literature are considered:

Table 1: Experimental parameters [10]

Workpiece Material	Ti-6Al-4V
Number of inserts	5
Hardness	42-46 HRC
Length of Pass	245 mm
Cutting Fluid	Water based synthetic
Coolant Pressure	1000 Psi (~70 Bar)
Cutting Speed	46 m/min and 58 m/min respectively
Chip Load (f_z)	0.25 mm per tooth
Axial ADOC (a_p)	3.8 mm
Radial ADOC (a_e)	51 mm
Cutter Body Diameter (D)	100 mm

Table 2: Experimental Results [10]

EXPERIMENT 1: MATERIAL REMOVAL RATE AT 46 m/min			
v_f = 183.03 m/min	v_c = 46.00 m/min	MRR = 35.47 cm^3	n = 146.42 RPM
EXPERIMENT 2: MATERIAL REMOVAL RATE AT 58 m/min			
v_f = 230.77 m/min	v_c = 58.00 m/min	MRR = 44.72 cm^3	n = 184.62 RPM

The material removal rate (MRR) achieved during experiments one and two are comparable to steel milling for both roughing and semi finishing operations (35.37 cm^3/min and 44.72 cm^3/min). Moreover, experiment results indicate a 2.5x tool life increase (Figure 16) compared to conventional HPTSC systems. Desirable cutting parameters are at high feedrates (f_z) and large ADOC's (a_p) with low spindle speeds (n).
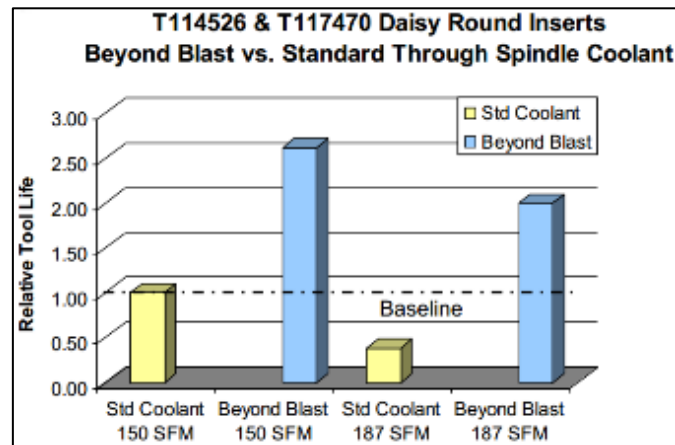
Figure 16: Beyond Blast Daisy round inserts vs. standard through spindle cooling [10]

Round insert cutters have a continuously variable entering angle, depending upon the cutting depth and causes a chip-thinning effect, suitable for machining difficult-to-cut materials [35]. Modern insert geometry developments have made the round insert milling cutters more widely suitable because of the smoother cutting action, requiring less power and stability from the machine tool. Today, it is not a specialised cutter anymore and should be regarded as an efficient roughing cutter, capable of high MRR's [35].
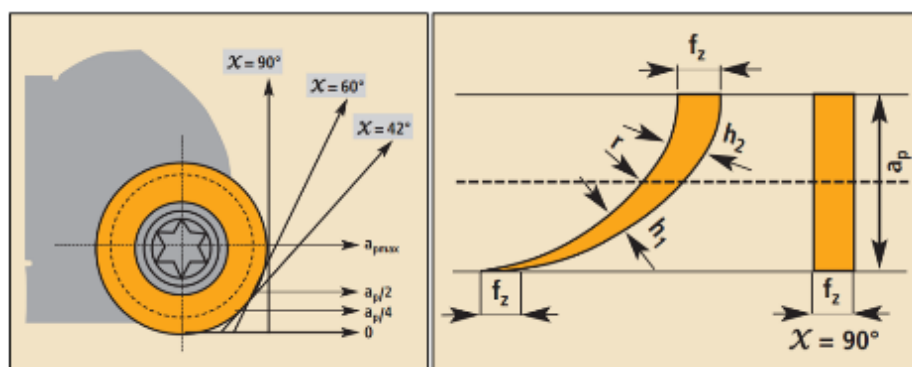
Figure 17: Round insert dynamic effective cutting diameter and superior chip lengths [36]

A unique trait of round inserts is that the effective cutting diameter increases dynamically with ADOC. Although chip thickness for a given feed per tooth is equal for round and straight edged inserts, the amount of material removed with round inserts per pass is superior. This is due to a larger contact area along the round cutting edge as shown in Figure 17. Nevertheless, with a larger contact area comes greater friction, which increases machining temperatures. This is the reason behind the development of a new coolant delivery method such as HPTSC-ST. Where high MRR's are required with round inserts, results have been achieved where the approach angle is close to 180 degrees and the ADOC is small [36].

2.3 CONCLUSION AND REMARKS

The use of coolant in the machining of Ti-6Al-4V serves multiple purposes. Coolant serves as a lubricant, which reduces cutting force, friction and heat, therefore increasing tool life. Coolant can also serve as an ejection mechanism for cut chips (higher pressure applications), prohibiting re-cutting and thus increasing tool life. The different cooling methods for consideration are summarised according to their strengths, weaknesses and cost of implementation in Table 3.

Table 3: Summary of Available Cooling Methods

Cooling Method	Operational Advantages	Operational Shortcomings	Cost of Implementation
Flood	Thermal shock minimised, relatively inexpensive and easy to setup.	Ineffective chip removal. Not suitable for high speed Ti-6Al-4V machining – Overheating.	Low cost.
HPC	More effective chip removal than flood. Penetration of Leidenfrost Barrier at high speeds.	Nozzle removed from cutting interface. Chips pushed back and re-cut. Increased thermal shock.	Widespread use, relatively low cost.
MQL DOS	Reduces oil mist deposit on work area by 80%. Similar performance to MQL. Low thermal shock.	Limited chip removal. Early stages of development. Setup can be challenging.	Not commercially available.
LN_2	Eliminates need for cutting fluids. Lower tool wear rate compared to HPC and MQL at high speeds.	Low speed results comparable to less expensive techniques such as MQL. Thermal shock.	Increased commercial availability. Expensive initial capital investment, especially for large scale installations.
HPTSC	Good chip removal. Strategically located nozzles. Successful integration with indexable tools and increased compatibility with machines.	Thermal shock. Chips sometimes blown back into cut by isolated coolant nozzles.	Widely available tools. Retro-fitting to older machines. Superior productivity over HP makes it feasible.
HPTSC-ST	High MRR, even for Ti-6Al-4V. Adhesion to inserts limited by coating and coolant's direction. Chips not re-cut.	Requires through spindle cooling capable machine.	Same as HPTSC, but inserts are more costly.

HPC provides better chip removal and penetration than flood cooling. It compresses the vapour barrier and successfully cools hot workpieces during high speed machining. Experiment results from previous work shows that tool life is not directly proportional to coolant pressure. Yet, the effect of HPC is diminished with high cutting speeds in excess of 125 m/min. In these high speed machining cases, cutting fluids often fail to penetrate the tool-chip interface. Gasses such as LN_2 provide better tool-chip interface penetration for high speed machining.

DOS is an improvement on conventional MQL due to its use of compressed air jets to reduce oil mist by 80%. As a result, the effectiveness of this cooling method is determined by the delivery mechanism. Operational improvements are incremental. The machining temperature of the direct oil drop supply system shows 4% improvement over dry machining and during experimentation flaking wear on the flank surface was observed. MQL systems are cumbersome and costly to install.

Liquid nitrogen holds distinct potential for high speed machining applications. Results from literature indicate that high pressure coolant and liquid nitrogen cooling provide similar performance benefits when compared at lower machining speeds (below 125 m/min). However, for high speed applications above 125 m/min, liquid nitrogen provides significant advantages. Findings from literature suggest that effectiveness of this cooling method is also dependent on the delivery system. As a result, more research and development from private companies has yielded products such as MAG's cryogenic through tool cooling. The technology offers a 60% speed increase with ten times increase in tool life due to the extraordinary low temperatures maintained at the tool and workpiece (-32°C and 86°C respectively). Unfortunately, this type of cryogenic machining is currently specialised, relatively costly and therefore more suitable for high volume production.

Kennametal's HPTSC-ST technology provides aggressive MRR's for rough and semi finishing face milling. Pocket milling tools are also available for intricate profile machining. During experiments conducted in the field, material removal rates of 35.37 cm^3/min and 44.72 cm^3/min at cutting speeds of 46 m/min and 58 m/min were observed. The use of round inserts causes a chip thinning effect that reduces cutting force and temperature. Round inserts in combination with the split tool cooling extends tool life by 2.5 times over other through spindle cooling applications.

The Beyond Blast coolant delivery method, through the insert rake face, achieves better penetration at the tool-chip interface compared to HPC and chips can be ejected more effectively. The improved delivery mechanism potentially reduces friction in the cut. Kennametal's choice to implement water based cooling with round insert split tools permits wider industry adoption. The cutter bodies are designed so that it is compatible with all milling machines that are capable of HPTSC.

CHAPTER 3

MACHINABILITY FACTORS FOR FACE MILLING

3.1 INTRODUCTION

The machinability of the workpiece has a significant influence on the machining thereof. Groover [37] lists these machinability factors as tool life or deterioration, forces and power, surface finish and ease of chip disposal. Similarly, Kalpakjian, Musa, and Schmid, [38] describe machinability factors as surface finish and integrity, tool life, force and power required, level of difficulty in chip control. Machinability indices for materials are available, but often lacking in specific detail on machining recommendations. Poor machinability would indicate short tool life, high cutting force and power requirements, long continuous and unmanageable chips that interfere with the cutting operation, as well as poor surface finish and integrity.

3.2 SURFACE FINISH AND INTEGRITY

3.2.1   Introduction

Surface finish refers to the geometric features of a machined surface area, while surface integrity describes material properties such as corrosion resistance, residual stress and fatigue life. Surface finish is influenced most predominantly by built up edge on tool tips. Dull tools or tools with large nose radi will cause more rubbing on the material surface during machining, because of the larger tool contact area. Rubbing generates heat, which can cause residual surface stresses that lead to component failures. It is common practice to adjust the ADOC to an amount that exceeds the nose radius of the tool [38].

On the other hand, surface integrity of Ti-6Al-4V can be affected by the raw material production process. A quenched Ti-6Al-4V component, for example, is likely to have high residual stresses. These residual stresses are not necessarily relieved during aging and components machined from such a raw material may show signs of distortion upon further analysis [39].

In the study of manufacturing and tool wear, surface roughness is most commonly denoted as R_a or Ra. This abbreviation refers to the arithmetic mean surface roughness measurement parameter. Surface roughness is generally expressed in microns (μm). The arithmetic mean value (Ra) is internationally used since 1955, because of its simplicity [38].

Cetin, Demirbas, Kuram, and Ozcelik [40] used a Mitutoyo Surf Test 301 for surface roughness (Ra) measurements for the comparison of different cutting fluids for a turning operation. Estrems, Faura, and Franco [41] used a SM RT-150 profilometer to determine arithmetic mean surface roughness (Ra) and profile for the prediction of the latter by examining factors such as feed, cutting tool geometry and tool errors. Similarly, Baek, Kim, and Ko [42] created a surface roughness model, based on feedrate, which

simulates a face milling operation to determine the arithmetic mean surface roughness. Lockheed Martin Space Systems also utilises the arithmetic mean surface roughness parameter for investigation of surface finish on the Juno spacecraft [43].

3.2.2   Measurement

During examination of surface finish, certain characteristics of the surface texture are considered. Figure 18 illustrates these characteristics: (1) Flaws and defects are random irregularities such as cracks, holes, seams, tears depressions, scratches or inclusions. (2) The lay is the direction of the surface pattern.
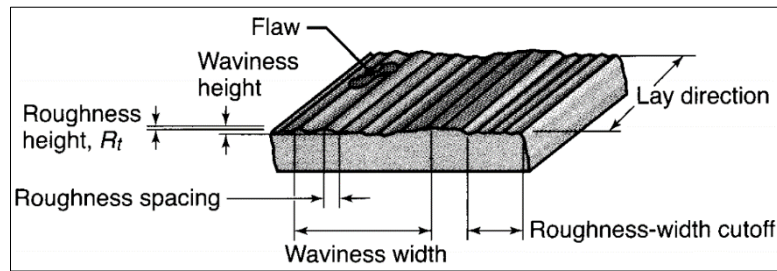
Figure 18: Surface texture characteristics [38]

(3) Roughness is defined as closely spaced, irregular deviations on a small scale and can be expressed in terms of its height, width, and distance along the surface. (4) Waviness is the recurrent deviation from a flat surface. It can be expressed in terms of distance between adjacent crests (waviness width) and distance between peaks and valleys (waviness height) [38] [37].

The calculation of the arithmetic mean surface roughness is based on the surface profile as shown in Figure 19 and is formulated as:

$$R_a = \int_0^{L_m} \frac{|y|}{L_m} dx$$

[Eq. 3.1]

Where L_m is the profile length and $|y|$ are absolute values for surface profile readings. For explanatory purposes, equation 3.1 can be rewritten as:

$$R_a = \frac{a + b + c + d + e + \cdots}{n}$$

[Eq. 3.2]

In equation 3.2, all coordinates are considered absolute values and *n* is the number of readings across the measured length of the profile, AB as shown in Figure 19.
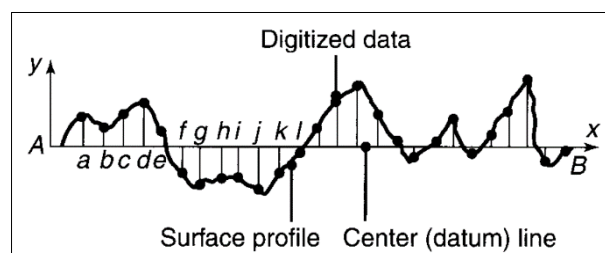
Figure 19: Arithmetic mean surface roughness profile [38]

Surface roughness is generally measured with a profilometer, which has a diamond tip, called a stylus. The stylus travels along the roughness profile, measuring magnitude of the peaks and valleys. The length of the path that the stylus travels along the profile is called the cut-off. The cut-off length is 0.8 mm in most engineering applications, though the cut-off for profilometers can be adjusted to 25 mm where there is a requirement [38]. Figure 20 shows the path of the stylus along the measured surface. The red line represents the actual path that the stylus travels. A diamond stylus tip is approximately 10 µm in diameter and can therefore not penetrate all the valleys in the profile. The stylus follows a path such as illustrated by the red line drawn across the peaks and valleys in Figure 20. A smaller stylus tip and smoother surface finish, will produce a more accurate roughness reading [44].
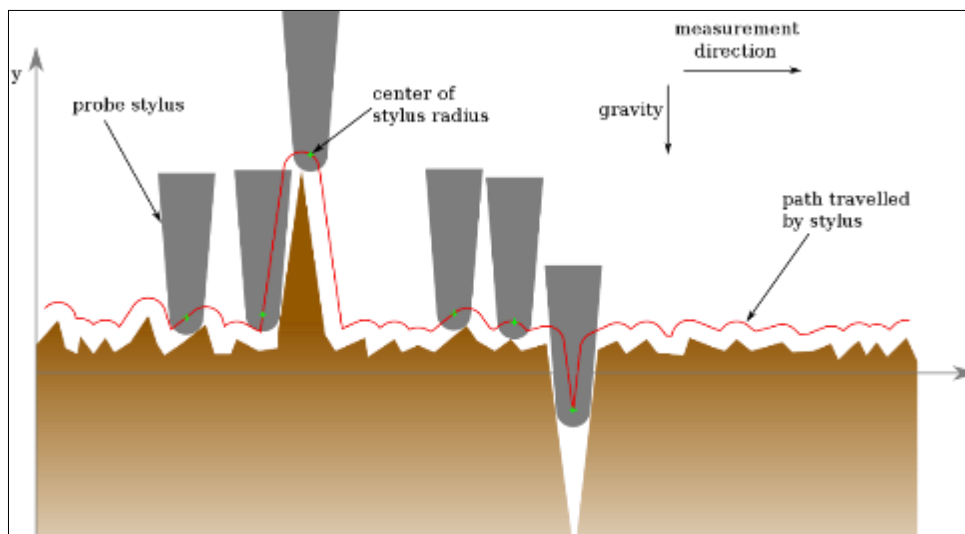
Figure 20: Profilometer stylus path along the cut-off length [37]

3.2.3   Considerations for Face Milling

The tool geometry and feed determine the surface geometry and it is the tool tip that is the important tool geometry factor. In the case where a larger tool nose radius is used at the same feedrate, the larger tool nose will produce a smoother finish, because the feed marks are less pronounced. On the other hand, where the same tool nose radius is used at two different feedrates, the larger feedrate will provide a rougher surface finish, because of the increase between feed mark intervals along the roughness profile [37].

Surface finish roughness for insert cutters typically ranges between 0.8 and 3.8 micron. Better surface finish is usually achieved with cutters that have non interchangeable cutting edges. Due to the indexing ability of cutters and accompanying inserts comes with certain drawbacks. Although the inserts are usually tightly seated in the cutter body by means of slots, grooves and a lock screw, tiny offsets in relation to each other still occur. The tool manufacturer advises that this offset be adjusted to an approximate maximum of 0.025 mm for a good surface finish [45].

There is a difference when comparing the surface roughness of the outside diameter of the cut with the roughness of the inside of the cut as shown in Figure 21.
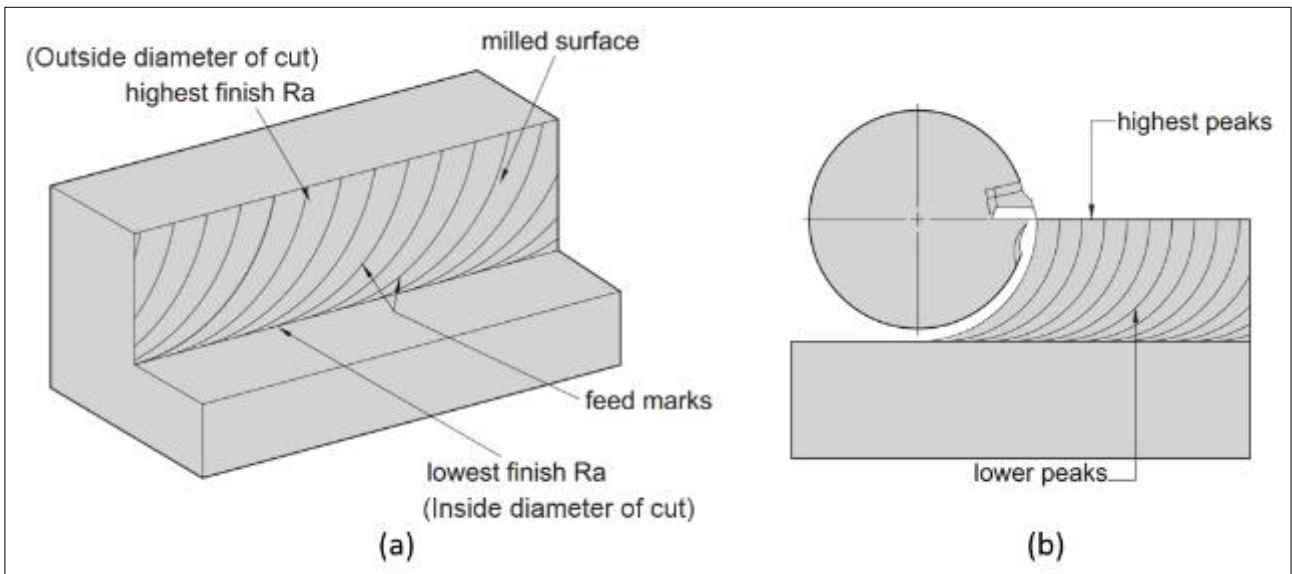
Figure 21: Surface finish face milling (a) Isometric view after milling (b) Top view during milling [45]

This phenomenon is more pronounced in cases where face milling is performed at a high radial engagement, because of the instantaneous radial position of each insert upon entry, compared to exiting the cut. The peaks are highest at the outer diameter of the cut, towards the centre line of the cutter, because the distance between passes is at the set maximum of the feedrate. At the inside diameter of the cut, the peaks are the lowest because the width between feed marks is reduced. When measuring the surface finish in such a case, the final surface roughness value is the maximum, e.g. the roughness at the outer diameter of the cut.

3.2.4   The Complexities of Surface Roughness Prediction

The theoretical depth of roughness for a turning operation can be calculated using the feedrate and nose radius value of the tool. Klocke and Kuchle [46] formulate the theoretical calculation as follows:

$$R_t = r_\varepsilon - \sqrt{r_\varepsilon^2 - \frac{f^2}{4}}$$

[Eq. 3.3]

Where R_t is the theoretical surface roughness, r_ε is the nose radius and f is the feedrate. Furthermore, Martellotti's classic study of surface roughness formulates the ideal surface roughness for a slab milling process as [47]:

$$R_i = \frac{0.125f^2}{(D/2) \mp (fn_t/\pi)}$$

[Eq. 3.4]

Where R_i is the ideal surface roughness, f is the feedrate, D is the effective cutter diameter and n_t is the number of teeth in the cutter. The positive sign (Eq. 3.4) in the denominator is for up milling and the

negative sign is for down milling. Mertellotti's equation assumes that the inserts are spaced perfectly around the cutter axis and in relation to each other within the cutter body. Additional assumptions relate to the straightness of the cutter, clamping rigidity, play on the spindle and that the inserts are always sharp. These conditions are rarely achieved in practice, due to a significant difference between theoretical versus measured values. Therefore the use of equations 3.3 and 3.4 are limited.

Benardos and Vosniakos [48] produced a review on roughness prediction for machining and validated previous findings by means of a neural network approach. Findings from reviewed literature point to the fact that theoretical prediction of surface roughness values is complex, due to a plethora of influencing factors that should be considered.

Figure 22: Influences on surface quality in metal cutting [46]

Benardos and Vosniakos constructed an intricate fish bone diagram to illustrate the associated complexities. Similarly, Kloche and Kuchle [46] efficiently summarises the currently known factors that influence surface quality in metal cutting as shown in Figure 22.

Surface roughness prediction models are known to be limited in their application and scope, because they are primarily valid for a specific set of conditions [41] [42] [49] [50] [51]. Conversely, Benardos and Vosniakos conclude that research in the field is increasing and that the resulting contributions are valuable for development of automated in-line inspection of machining operations.

3.3 CHIP CONTROL

3.3.1   Introduction

Ti-6Al-4V machining generates heat, concentrated at the tool tip, due to the material's low thermal conductivity. Chips formed during Ti-6Al-4V machining are characterised by a serrated or segmented formation, due to the low modulus of elasticity of Ti-6Al-4V. More specifically, the findings Ozel and Sima [52] suggest that for cutting speeds of 60 m/min and above, serrated chips with accompanying adiabatic shear bands are visible during electron microscope analysis. Similarly, Komanduri and von Turkovich [53]

report that Ti-6Al-4V is regarded as model material by investigators, because it forms serrated chips at low cutting speeds. Other materials typically start producing serrated chips at higher cutting speeds.

The physical characteristics of chips provides important evidence about the formation at the shear zone. The examination of the shape of the chip provides information about the condition of the tool tip, cutting speed, shear force and temperature at the tool-chip interface.

3.3.2 Chip Classification Criteria

Chips are generally classified into four categories. They are: Continuous chips, segmented or serrated chips, chips that result from a built-up edge (BUE) on the tool and shearing or discontinuous chips as shown in Figure 23 [38] [46] [37].
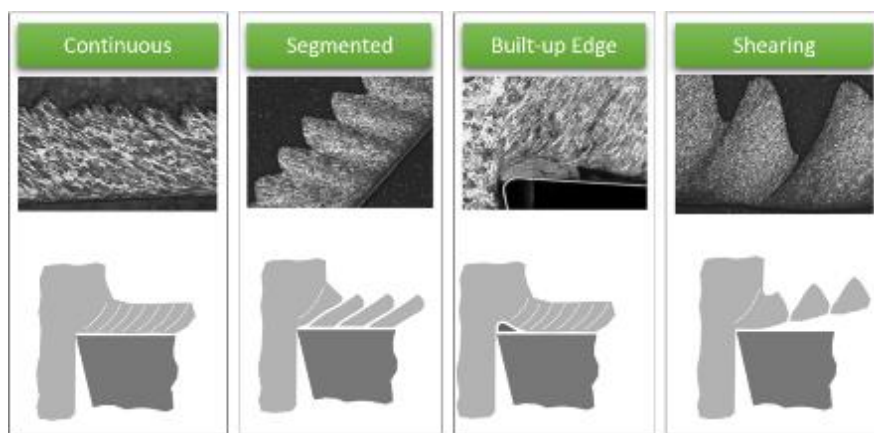
Figure 23: Chip type categories [46]

Continuous chips are formed when ductile materials are machined at high cutting speeds with small feedrates and ADOC. This type of chip usually produces a desirable surface finish, but tend to tangle around critical parts of machines such as the tool holder (turning) or cutter body (milling) as well as the fixturing and chip evacuation system. A continuous chip also provides evidence of low friction at the shear zone, hence lower cutting temperatures and therefore improved tool life. Chip breakers are frequently used to control the length of this chip type, that increases the overall manageability thereof. Additional remedies to control chip geometry include changing cutting speed, ADOC and using cutting fluid [54] [37] [38].

Segmented chips have a distinctive sawtooth appearance due to the cyclical alteration in strain at the shear zone. This type of chip is also refered to as serrated or non-homogenous. This sawtooth appearance is characteristic in the machining of difficult-to-cut superalloys, particularly titanium alloys. The sawtooth chip profile can also be observed with the machining of more common metals at high cutting speeds [54] [37] [38].

BUE chips are caused by the adherence of the work material to the tool tip due to tool-chip friction at the shear zone at lower cutting speeds. As the cutting speed increases, the BUE decreases. The magnitude of the BUE on the tool tip varies constantly as material accumulates on the tip and finally breaks off in a

cyclical manner, until corrective measures are taken. During machining, the BUE material is partially removed from the tool tip by the in-contact chip area and the rest is deposited on the workpiece surface. This undesireable effect causes changes in the tool tip geometry and contributes to premature dulling. An additional drawback is the negative effect of the BUE deposits on the finished workpiece surface. Managing a smaller BUE is advantegous, because it protects the rake face and extends tool life [54] [38] [37].

Shearing or discontinuous chips are formed when machining a brittle or impure material or during extreme cutting speeds beyond the machinability guidelines for feedrate and ADOC. Poor workpiece clamping, flexure in the tool holder and the milling machine are causes of chatter and vibration, that results in discontinuous chips. Depending on the degree of rigidity in the milling machine setup, the cutting tool may wear prematurely or even become damaged. The surface finish for ductile materials is negatively impacted when discontinuous chips are formed, while discontinuous chip formation has a positive impact on surface finish for less ductile materials such as Ti-6Al-4V. [54] [37] [38]

3.4 TOOL DETERIORATION PHENOMENA

Groover [37] lists three failure modes for cutting tools: (1) Fracture failure, (2) temperature failure and, (3) gradual wear. In agreement to this, the ISO standard for tool life testing in milling defines these three failure modes as (1) brittle fracture, (2) plastic deformation and, (3) tool wear [55]. These failures can be subdivided into more specific failure phenomena.

3.4.1   Flank Wear

The typical components of a milling insert for an indexable tool is illustrated in Figure 24. The insert flank face is represented by A. The flank is the part of the insert that comes into contact with the workpiece as the cutter rotates. Flank wear results from the friction between the tool flank face and the material being cut [37]. Friction is high on the flank face and this is where most of the tool wear should occur under normal Ti-6Al-4V machining conditions. The rake face is the area of the insert that is adjacent to the cutting edge and denoted by B. The rake face mostly directs the flow direction of the newly cut material. The insert clamp screw is denoted by D. The insert clamp screw pulls the indexable insert onto the insert seat, which is represented by C.
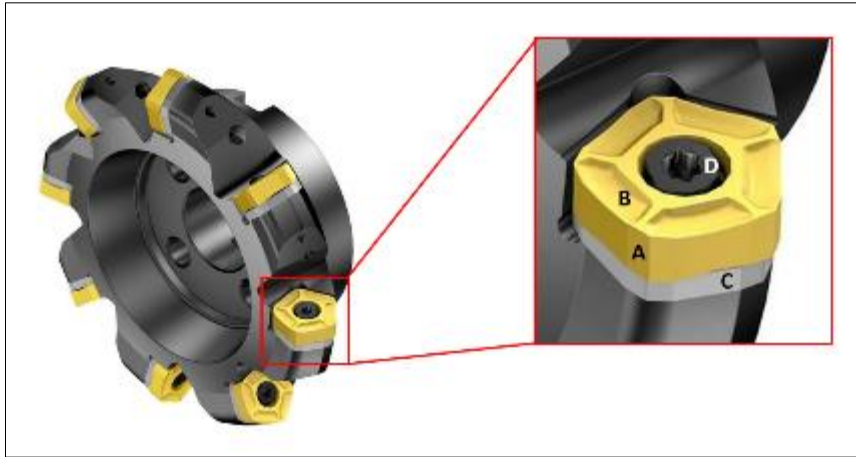
Figure 24: Milling insert components

Flank wear is a gradual process and characteristic of normal cutting conditions, however, flank wear can be accelerated in cases where inadequate lubrication is applied or cutting speeds are excessive [38] [56].

Flank wear is measured by determining the width of the wear bands, also known as the wear land, on the rake face as shown in Figure 25.
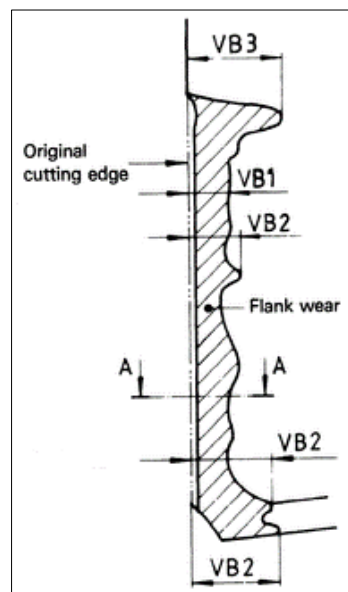
Figure 25: Flank wear measurement criteria for an endmill [57]

The wear land is measured from the position of the original cutting edge even in cases where the edge is worn away. In such a case, the position of original cutting edge is determined by extending the line from the neighbouring, unaffected cutting edge. VB 1 is the uniform wear land and usually has a constant width across the cutting edge. Uniform wear is considered the as the average wear on the cutting edge and denoted as V_b in literature. Non-uniform flank wear has an uneven width for all occurrences along the flank and is illustrated as VB 2 in Figure 25. Non-uniform flank wear is also described as maximum flank wear and denoted as V_{bmax} in literature. ISO 8688-1 : 1989 [55] further describes localized flank wear as exaggerated

flank wear at localized areas on the flanks. Localized flank wear is referred to as VB 3 and is further subdivided into notch wear and groove wear as shown in Figure 26.
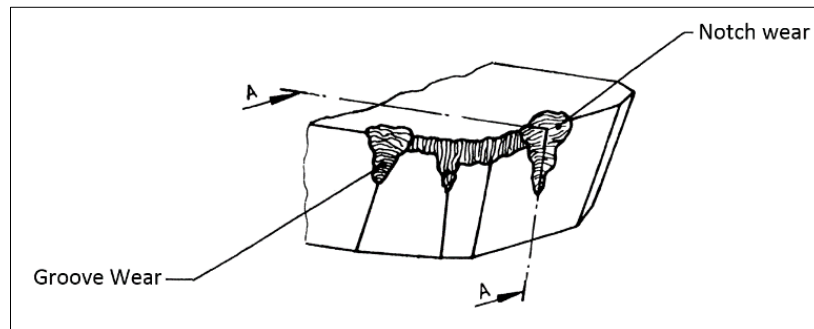
Figure 26: Localized flank wear in the form of notch wear and groove wear [55]

The flank wear rate can be decelerated by choosing a more suitable tool grade for the material being cut, reducing cutting speed or selection of a smaller entering angle. The Taylor tool life equation is based on flank wear:

$$VT^n = C$$
[Eq. 3.5]

Where V is the cutting speed, T is the time (min) to develop a certain wear land (V_b), n is a workpiece and tool material exponent and C is a constant. The value for factors n and C are determined experimentally, through performing numerous cutting tests at different cutting speeds, feedrates, depths of cut, tool materials and geometries. Cutting speed is the primary factor affecting tool life [37] [56] [58] [38].
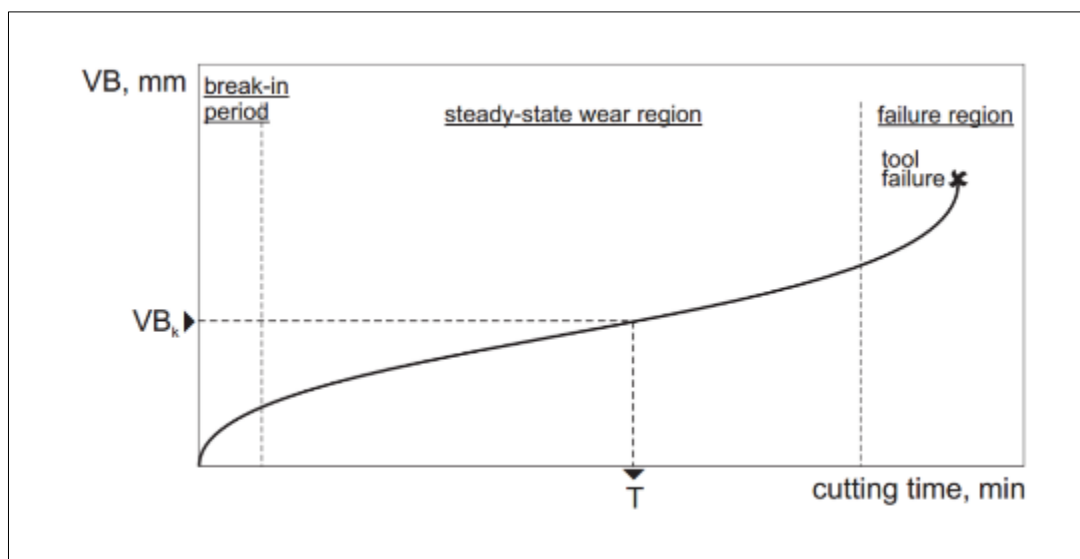
Figure 27: Flank wear as a function of time [58]

The break-in period (Figure 27) sees the tool's sharp cutting edge rapidly wear during the first few minutes of machining. During the steady-state wear period, wear is uniform although not a linear relationship over time in all cases. The failure region marks the useful tool lifetime where cutting temperatures are elevated and productivity is reduced due to approaching maximum flank wear for the tool [37].

During tool wear experiments, the cutting time is recorded and the wear land is measured. Tool wear experiments are rather costly, because large amounts of material is removed to record tool wear from break-in to failure as shown in Figure 27 and also explained earlier in Figure 4 and Figure 8.

Costs are increased for high cost alloys such as Ti-6Al-4V [4]. The cost of recording the tool failure time for face milling with a tool diameter of 63 mm (Kennametal Beyond Blast KSRM63A04RC20BB) would therefore not be feasible for academic purposes at university level.

3.4.2   Crater Wear

Crater wear (Figure 28) consists of a concave section on the rake face and occurs with high cutting temperatures that is caused by chip friction against the rake face. Craters are predominantly measured by depth or area [38]. Diffusion is usually associated with crater wear. During diffusion, atoms are exchanged in the tool-chip interface. Diffusion depletes the tool tip of the atoms responsible for its hardness. The tool then becomes more vulnerable to abrasion and adhesion.
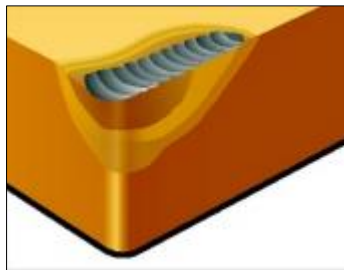
Figure 28: Crater wear [56]

ISO 8688-1 : 1989 [55] also explains how crater wear (KT 1) is typically formed parallel to the major cutting edge and the maximum crater depth is often located some distance away from the major cutting edge. Another closely related type of wear is stair-formed face wear (KT 2), in which the maximum depth of the wear scar occurs at the intersection of the wear scar with the tool major flank.
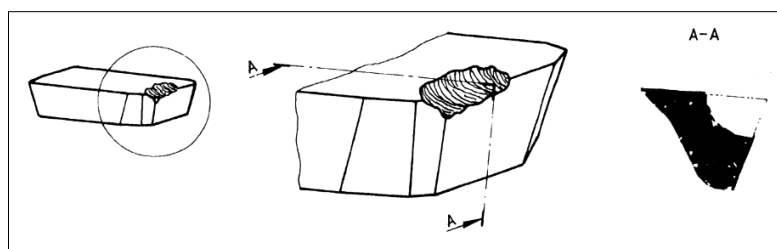
Figure 29: Stair-formed face wear [55]

Cratering or stair-formed face wear is remedied by reducing the cutting speed and increasing coolant to the tool-chip interface [37] [56]. ISO 8988-1 : 1989 provides a guideline for maximum crater size in terms of testing time, under a tool deterioration section [55]. Unfortunately, crater wear can be challenging to measure accurately.
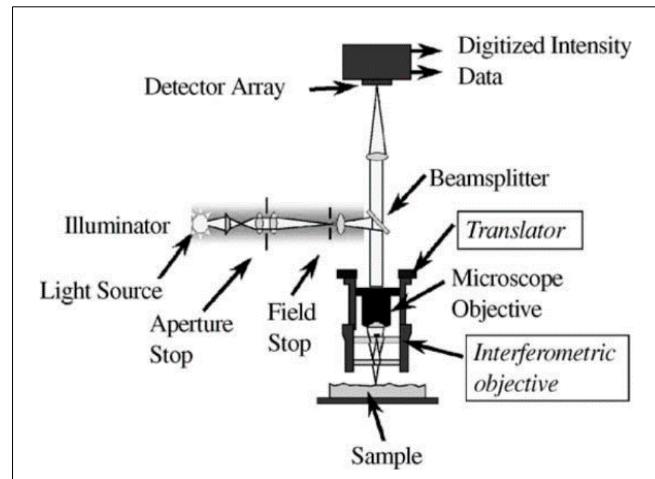
Figure 30: Vertical scanning interferometer [59]

Devillez, Lesko, and Mozer [59] proposed the use of white light interferometry for the measurement of the crater depth as shown in Figure 30. During white light interferometry, an optical profiler is used to scan the object (such as a cratered insert) along the vertical axis. Fringes developed along the crater as each area of the surface moves into focus. The images are communicated to a computer algorithm that fits the data with a coherence envelope, which reveals the crater depth.

Alternatively, Hong, Wang, and Wong, [60] measures crater wear by implementing a phase shifting method to achieve a 3D rendering of the tool surface. During the scanning process, an LCD projects linear sinusoidal fringe patterns over the insert as shown in Figure 31 (a).
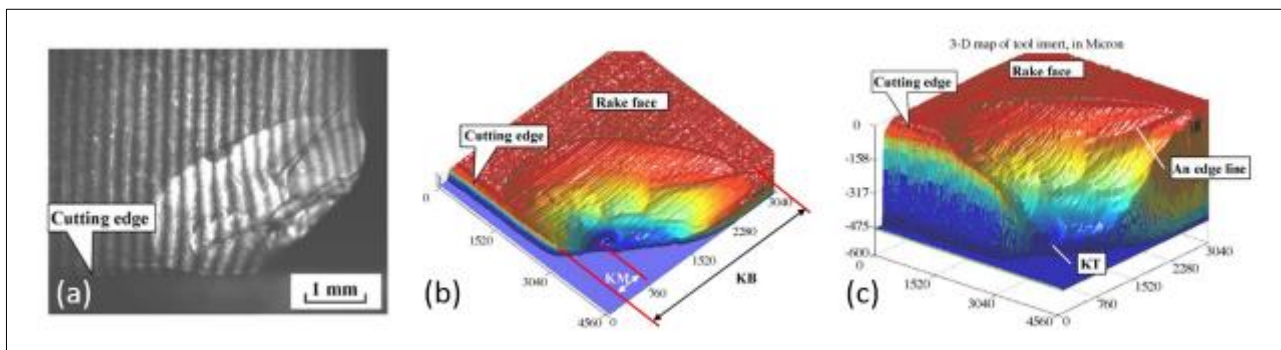
Figure 31: 3D map (b & c) of insert crater (a) [60]

These projections are altered from four different angles with respect to the insert, which is mounted on a stage in front of the projector and microscope camera. The images are captured by a long working distance microscope. The captures 256-graylevel images are then processed to map the 3D surface as shown in Figure 31 (b & c).

3.4.3   Notch and Groove Wear

Notch and groove wear is characterised by a noticeable indentation at a certain point along the worn major and minor flank face. ISO 8988-1 : 1989 [55] categorises notch and groove wear under localized flank wear, because the notches develop on the area of the major flank adjacent to the work surface during cutting as

shown in Figure 32 b. However, groove wear is formed on the area of the minor flank adjacent to the machined surface during cutting as shown in Figure 32 a.
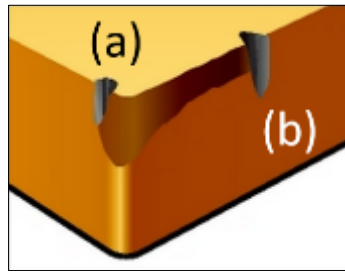
Figure 32: (a) Groove wear, (b) Notch wear [56]

Notches or grooves are initiated when machining a material that has an inconsistent hardness gradient. In practice a hardened outer layer is encountered. Residues from sand casting, hardening from cold drawing or previous machining are the main causes of notch wear. Sandvik Coromant [56] suggests that notch or groove wear can be caused by excessive cutting speed and Kennametal blames incorrect cutter geometry [45].

3.4.4   Plastic Deformation

Plastic deformation (PD) is the distortion of the cutting part of a tool from its original shape without initial loss of tool material as shown in Figure 33 [55]. During PD, the cutting tool edge geometry is transformed by high temperatures at the tool-chip interface. The cutting force pressure on the tool further contributes to the deformation of the geometry.
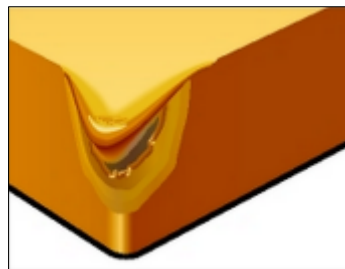
Figure 33: Plastic deformation [56]

A plastically deformed tool is more susceptible to flank wear, because of increased abrasion. PD is reduced by selecting a harder grade tool, reducing feedrate and cutting at a lower speed [56].

3.4.5   Chipping

Chipping patterns have a saw-toothed appearance and can easily be mistaken for normal flank wear as shown in Figure 34. An ineffectively clamped workpiece or re-cutting of chips is often the cause [45] [56].
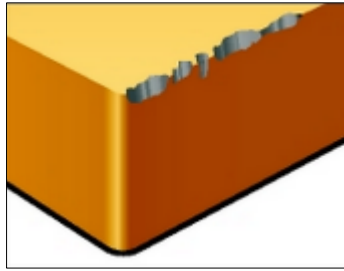
Figure 34: Non-uniform chipping (CH 2) [56]

There are four types of chipping according to ISO 8988-1 : 1989: (CH 1) Uniform chipping, where the loss of tool fragments along the cutting edge is around the identical size, (CH 2) Non-uniform chipping which is formed at a few positions along the active cutting edges but with no uniformity from one cutting edge to another, (CH 3) Localized chipping which happens consistently along specific locations along the active cutting edge, and (CH 4) Chipping of the non-active part of the major cutting edge, which is formed outside the active part of the cutting edge due to chip hammering [55].

Chipping can be reduced by changing from a tool with a neutral geometry to a lead angle geometry. Rigid clamping reduces chatter and an increase in coolant pressure or better delivery system helps to prevent the re-cutting of chips [56] [45].

3.4.6   Edge Fracture or Catastrophic Failure

This phenomenon (Figure 35) is observed when there is rapid deterioration to complete failure of the cutting part [55]. A number of factors contribute to edge fracture: Excessive load on the insert, BUE, excessive tool wear, tool grade and incorrect geometry [56]. Edge fracture can also occur in cases similar to chipping, due to lack of stability in the workpiece clamping.
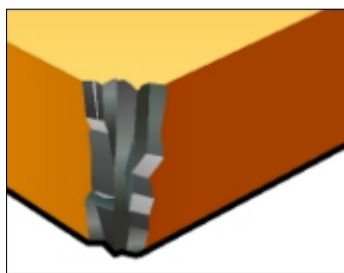
Figure 35: Edge fracture [56]

Edge fracture can be reduced by reducing the feedrate and ADOC, while ensuring that the workpiece is rigidly clamped. Selection of a more suitable insert type, with regards to geometry and grade reduces the chances of fractures.

3.4.7   Thermal Cracking

Thermal cracking is induced by extreme temperature variations within the cutting tool insert during cutting. There are three types of cracks: (CR 1) Comb cracks which form on the tool face and the tool flank and are oriented perpendicular to the major cutting edge, (CR 2) Parallel cracks that appear on the tool face or the

CHAPTER 3: MACHINABILITY

tool flank and are orientated parallel to the major cutting edge, (CR 3) Irregular cracks, which appear on the tool face and on the tool flank and are randomly orientated [55].

With every revolution of the milling cutter the insert enters the cutting interface and friction causes the temperature to rise abruptly. As the insert leaves the cutting interface, the coolant rapidly reduces the insert temperature. This cycle is repeated with every revolution of the cutter. The phenomenon is also known as thermal shock.
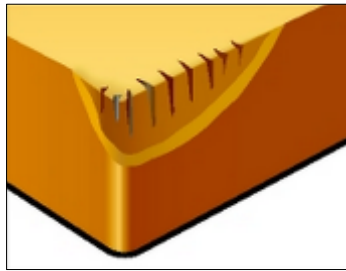
Figure 36: Thermal cracking [56]

Thermal cracking can be reduced be turning off the coolant, reducing cutting speed, or by using coated inserts designed specifically for wet milling [45] [56].

3.4.8 Built-up Edge (BUE)
The causes and effects of this phenomenon is discussed in section 3.2.2.
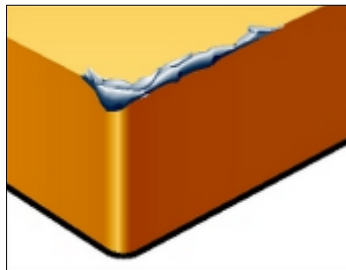
Figure 37: Built-up edge [56]

BUE can be reduced by increasing cutting speed, sharp PVD inserts and adjustment to coolant delivery for better chip removal [45].

3.4.9 Flaking
Flaking when the tool surface is steadily removed in the form of flakes. Flaking is most often observed when coated tool inserts are used but may also occur with other tool materials [55].
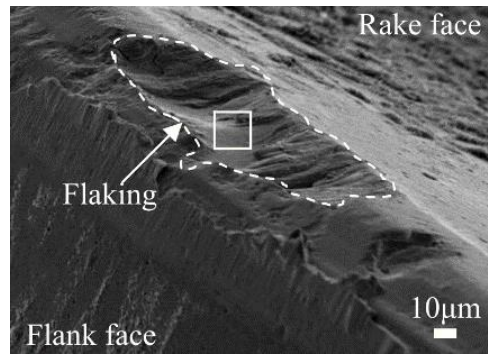
Figure 38: Flaking on the cutting edge of a turning insert [61]

Flaking can also be caused in cases where the cutting tool is used at feedrates or cutting speeds in excess of the tool manufacturer's specifications for that particular material [62].

3.5 FORCE AND POWER REQUIRED

3.5.1 Forces in Machining

Knowledge of the magnitude of the cutting forces during machining is important. Kalpakjian et al. [38] elaborates on the significance of cutting force data: The design of machine tools is based on the magnitude of cutting forces, amongst other factors. A knowledge of the cutting forces prevents distortion of machine components, maintains the desired dimensional accuracy of the machined part and aids in selecting correct tool and work holding devices. Attention to these factors reduces the distortion of the finished workpiece. The power requirements also need to be determined for selection of the appropriate machine tool.

A cutting force diagram can be constructed to determine the force components acting on the tool and workpiece as shown in Figure 39 [46]. This force diagram is known as a Merchant force diagram and is named after its creator, Eugene Merchant [63]. Merchant's force wheel is interpreted as follows: In Figure 39, the forces acting on the chip are divided into two perpendicular components, namely friction force (F_γ) and normal force to friction ($F_{\gamma n}$). $F_{\gamma n}$ is perpendicular to F_γ. These two forces are used to define the coefficient of friction between the tool and chip:

$$\mu = \frac{F_\gamma}{F_{\gamma n}}$$

[Eq. 3.6]

The vectors F_γ and $F_{\gamma n}$ are added to form the resultant force F_z which is orientated at angle ρ. This angle is known as the friction angle [37]. The relationship of the friction angle (ρ) and the coefficient of friction is written as:

$$\mu = \tan \rho$$

[Eq. 3.7]

There are also two additional tool forces components acting on the chip, namely shear force (F_ϕ) and normal force to shear ($F_{\phi n}$). Shear force (F_ϕ) causes shear deformation at the shear plane to which the

normal force to shear ($F_{\phi n}$) is perpendicular [37] [46]. The shear stress that acts along the shear plane between the work and the chip is formulated as:

$$\tau = \frac{F_\phi}{A_s}$$

[Eq. 3.8]

Where A_s is the area of the shear plane (mm²). The shear plane area is:

$$A_s = \frac{t_o w}{sin\phi}$$

[Eq. 3.9]

Shear stress from Eq. 3.8 is the magnitude of stress required to perform the machining operation. Shear stress is therefore equal to the shear strength ($\tau = S$) of the work material during cutting. When the two vectors F_γ and $F_{\gamma n}$ are added, the resultant force F_z is determined. The forces acting on the chip must be in balance and therefore F_z must be equal, collinear and opposite in direction as F_z' [37] [38] [46].
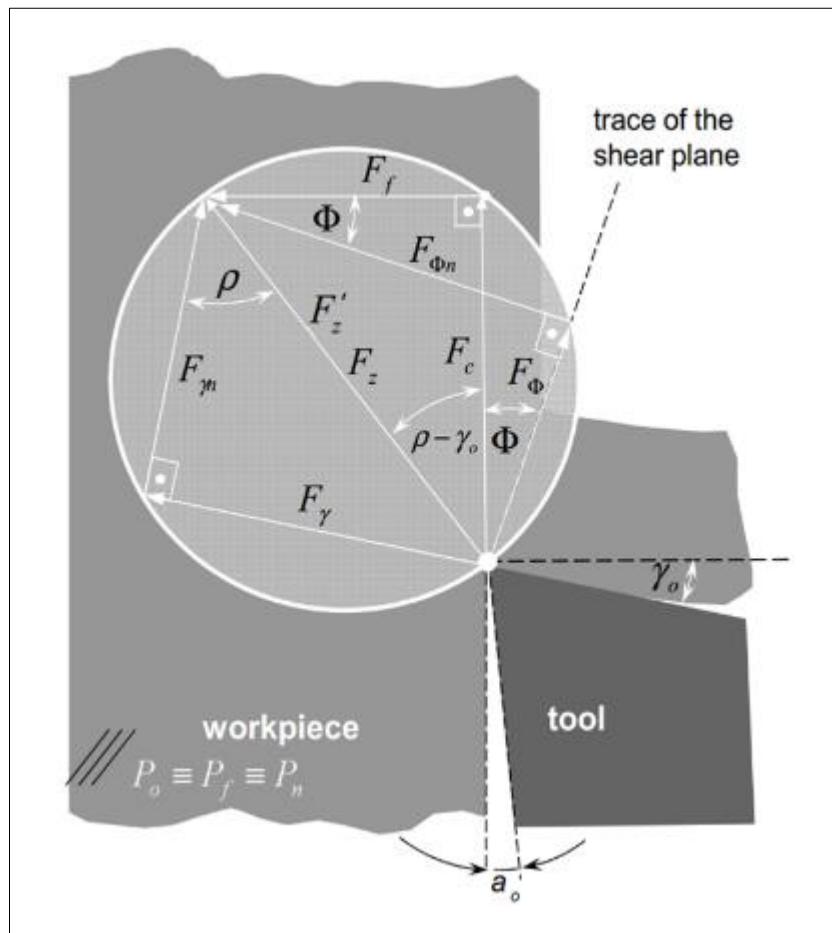
Figure 39: Merchant's force wheel [46]

None of the forces F_γ, $F_{\gamma n}$, F_ϕ or $F_{\phi n}$ can be directly measured during cutting, because their directions vary with tool geometries and cutting conditions. Dynamometers enable the direct measurement of the two additional force components acting against the tool. These forces are thrust force (F_f) and cutting force (F_c). Cutting force is in the direction of cutting and thrust force is perpendicular to cutting force.

Equations can be derived to relate the force components F_γ, $F_{\gamma n}$, F_ϕ or $F_{\phi n}$ to the two forces that can be measured with the dynamometer:

$$F_\gamma = F_c \sin \gamma_0 + F_f \cos \gamma_0 \qquad \text{[Eq. 3.10]}$$

$$F_{\gamma n} = F_c \cos \gamma_0 - F_f \sin \gamma_0 \qquad \text{[Eq. 3.11]}$$

$$F_\phi = F_c \cos \phi - F_f \sin \phi \qquad \text{[Eq. 3.12]}$$

$$F_{\phi n} = F_c \sin \phi + F_f \cos \phi \qquad \text{[Eq. 3.13]}$$

If F_f and F_c are known, equations 3.10-3.13 can be used to determine the shear force, friction force and normal force to friction [37]. Subsequently, based on these forces shear stress and the coefficient of friction can be calculated.

3.5.2   The Effect of Tool Geometry on Cutting Force

Tool geometry is a contributing factor to cutting forces during machining. When both the radial and axial rake angles are positive, it is referred to as a double-positive geometry. Figure 40 (a) shows such an example. Double positive geometry is used for softer, non-ferrous materials such as copper and aluminium. This geometry is implemented in cases where there is limited power available from the milling machine spindle. Chips are removed effectively and the surface finish is smooth, but care needs to be taken with the setup as the inserts tend to chip at the edges and the positive radial angle may lift the workpiece from the table [64] [65].
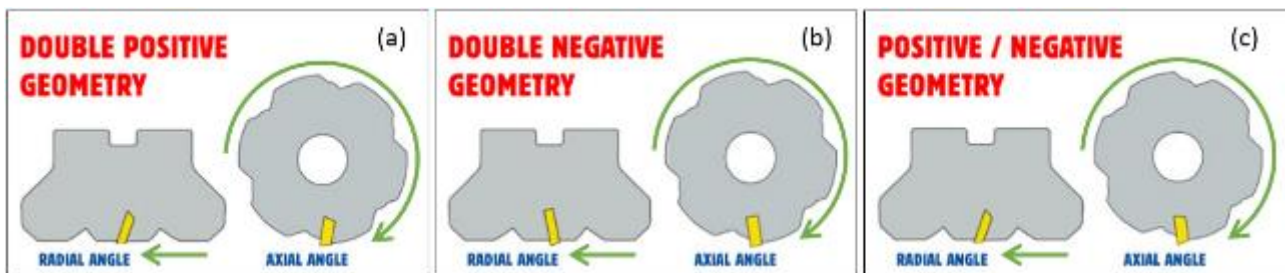
Figure 40: Tool geometries [65] [64]

A double-negative cutter has a negative radial and axial rake angle as shown in Figure 40 (b). This geometry is mainly used in the machining of cast iron. The negative rake angle pushes the workpiece towards the table. Large cutting forces are required for a cutter with this geometry.

Positive-negative cutters , as depicted in Figure 40 (c), are mainly used for titanium alloy milling as it requires less cutting force and hence consumes less energy [64] [65].

3.5.3 Power Required in Machining

Cutting power is the product of force and velocity. The cutting power is largely dissipated in the shear zone (due to energy required to shear the material) and at the rake face of the tool (due to tool-chip interface friction) [38].

The power equation can therefore by derived as [45] [37] [38]:

$$P_s = F_c v_c \qquad \text{[Eq. 3.14]}$$

Where P_s = power at spindle (kW), F_c is the cutting force component and v_c is the cutting speed. The instantaneous power required by a certain cut is limited by the maximum allowable power at any given revolutions per minute according to the milling machine spindle specification for power and torque delivery.

3.5.4 Modeling of Cutting Forces

A significant amount of publications cover the area of modeling cutting forces for a machining operation. Most popular among these are models for drilling, milling and turning operations. Publications also differ in their modeling approach: Some follow a mechanistic approach to predict cutting forces, while others rely on the finite element method (FEM). In addition, the statistical or nonparametric approach to force prediction is increasingly used. The statistical approach differs from mechanistic and FEM approaches in that the majority of experiments for such a model are performed before modeling is done. Thereafter it is commonplace to utilise tools such as analysis of variance (ANOVA) or regression to evaluate factorial relationships and also test the error between the model and experimental values. The inverse is true for mechanistic and FEM modeling.

During the classic study of Chandrasekharan, DeVor, and Kapoor, [66] a mechanistic model was developed from first principles to predict thrust force during drilling. The mechanistic model was compared to experiment results and a maximum error of 10% was reported in the predicted mean thrust values.

Similarly, Baro, Joshi, and Kapoor [67] developed a mechanistic model for face milling. The purpose of the model is to predict cutting forces for face milling with self-propelled round inserts. Baro et al. follows the same methodology as Chandrasekharan et al. in that a mechanistic model is validated with experiments. Additional factors considered by Baro et al. are the various frictions acting on the cutting interface, geometry of the insert and geometry of the cutter. Experiments are validated using a dynamometer. The maximum error between measured and predicted forces is 17% for this study.

Another mechanistic prediction model is that of Huang and Liang [68]. They derived a mechanistic force prediction model for turning, considering the tool wear effect. Subsequently, a genetic algorithm was applied to identify the coefficients, due to the absence of explicit normal equations. Finally, cutting force

prediction was validated through obtaining experiment results by means of a dynamometer mounted to the tool post.

Hsieh, Shih, and Strenkowski [69] modeled drilling thrust force with a FEM technique. The model was validated with laboratory experiments at several drill diameters, spindle speeds and feedrates.

Furthermore, Altan and Özel [70] developed a FEM model for flat end milling, which was then validated with experiments, using a dynamometer. Experimental results showed "reasonable agreement" with predicted force values. The interpretation of the results follow a subjective approach due to the prediction of an entire cut cycle waveform instead of a mean force value for a given axis. The predicted values appear to closely follow the maximum measured cutting force along the force curve.

The FEM approach taken by Hossan and Qian [71] for predicting cutting force during a turning operation differs slightly from other modeling approaches as it uses results from literature to validate predicted values. Predicted force error is a maximum of 15% when compared to results from literature. It is worth mentioning that models are often validated against results from literature if researchers do not have access to high cost testing equipment such as dynamometers or heavy milling machines.

Hocheng and Tsao [72] follows the Taguchi method: Multi-variable linear regression through ANOVA to statistically predict thrust forces during core drilling of carbon fibre reinforced polymer. The correlation between thrust force and cutting parameters is also described. Verification of the predictive model reveals a maximum error of 15.3%.

Amin, Faris, and Patwari (2009) [73] incorporates experimental design and (response surface methodology) RSM to predict tangential cutting force in end milling. The cutting parameters of the model are ADOC, feedrate and cutting speed. The measured response is tangential cutting force. Through ANOVA it was determined that the cutting force is most affected by feedrate, then ADOC, and finally cutting speed. Central composite design was applied to develop the force model in relation to the cutting parameters. The significance of the model was verified with ANOVA at a 95% confidence level.

During turning experiments Bouacha, Mabrouki, Rigal, and Yallese [74] explores the relationship between machining input parameters and output variables with RSM. The effect of ADOC, feedrate and cutting speed on cutting force is determined through ANOVA. Bouacha et al. finds that the ADOC has the largest influence on the cutting forces measured during experimentation.

3.5.5 Response Surface Methodology (RSM)

Montgomery [75] [76] defines RSM as, "A collection of mathematical and statistical techniques useful for the modeling and analysis of problems in which a response of interest is influenced by several variables and the objective is to optimize this response." RSM is a sequential technique for following a path to the

optimum response surface. The path that the experimenter follows is called the method of steepest ascent, and in cases where minimization is required, it is called the method of steepest descent.
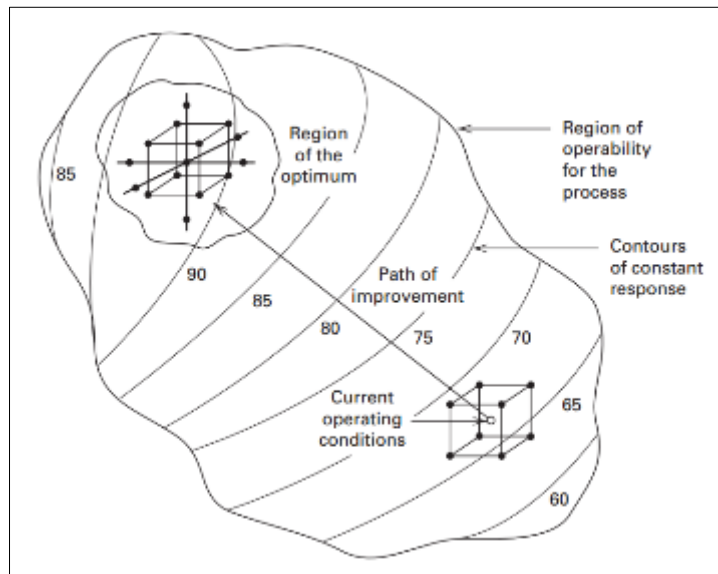
Figure 41: The sequential nature of RSM [75]

The response surface can be represented by the entire curved surface in Figure 41. The relationship between the dependent and the independent variables is often unknown at first. The experimenter usually starts some distance away from the optimum as shown by the 'current operating conditions' in Figure 41. First, the experimenter needs to approximate the true functional relationship between the response and the independent variables employed. This is usually achieved through a first-order model that is derived from a fractional factorial or full factorial design as shown in Figure 42 (a) and (b) respectively. If the response is well modeled by a linear function of the independent variables, then the approximating function is the first-order model. If this is not the case, then the steepest ascent method is followed until a decrease in response is observed as shown by the contours in Figure 41 [75] [77].
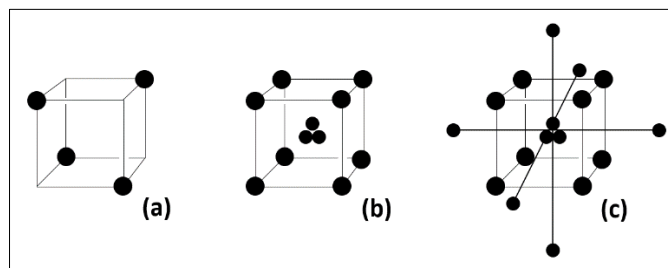
Figure 42: (a) Fractional factorial (b) Full factorial with centre points (c) Central composite design

A factorial design with centre points, as shown in Figure 42 (b), is then fitted around this region. If the ANOVA for this model reveals no significant curvature, then a first-order model may very well adequately represent the optimum surface. Conversely, if significant curvature is detected by the full factorial design, then additional experiments need to be performed to establish a second-order model [75] [78]. A second-order model usually significantly describes the response surface, but in certain cases a third or fourth-order

model might be of better significance. Additional experimentation usually follows a central composite design methodology as illustrated in Figure 42 (c).

The second-order model fitted by means of the central composite design method allows the experimenter to construct a response surface with the aid of computer software.
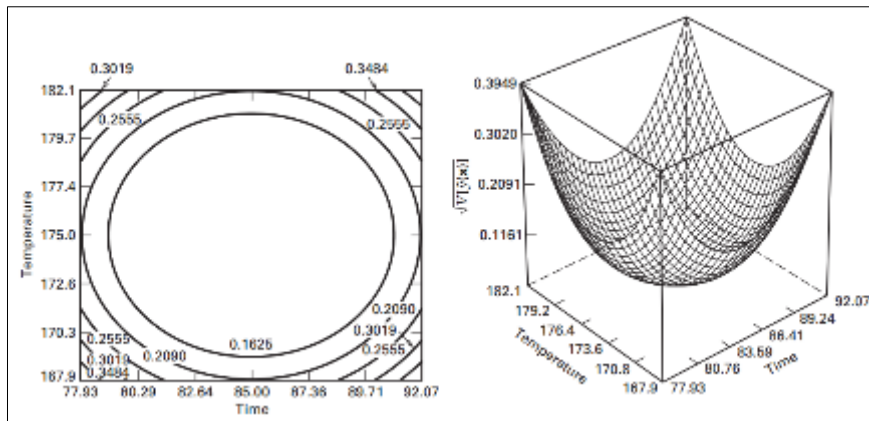
Figure 43: Contours and response surface [76]

RSM is a valuable tool in determining the optimum operating characteristics of the modeled function, especially when a rotatable design was chosen. Figure 43 shows the concentric circle contours, which means that the response is the same on all points along the same contour that are the same distance from the centre of the design. The valley represented by the 3-dimensional response surface in Figure 43 further shows that the optimum response values are for a minimization problem and that a method of steepest descent was followed. The response values around the centre contours are therefore minimum optima.

3.6 CONCLUSION AND REMARKS

Surface finish is generally measured with a profilometer in micron and the arithmetic mean surface roughness method is followed. Surface roughness is affected by numerous factors that are difficult to control in practice. Despite the widespread use of the arithmetic mean surface roughness method, there are limitations to its accuracy.

Conditions at the tool-chip interface affect chip formation. There are four main categories for the types of chips. Furthermore, the characteristics of machined chips provide evidence about machinability factors such as the material being cut, the magnitude of the cutting force, geometric features of the cutting tool and the quality of surface finish and integrity. Chip analysis is an important tool in the improvement of machining operations.

Tool wear is a factor of productivity and is typically affected by cutting speed. There are roughly nine different categories of tool wear. The type of tool wear observed during a machining operation suggests the specific corrective measures that needs to be taken for increased productivity. Flank wear is the principal measure of tool wear and tools normally wear according to three distinct phases over time. Tool

wear is measured by recording the width of the wear land on the insert flank. Tool wear measurement requires microscopy. Examination of tool wear across all three phases of wear can be a time consuming and therefore costly exercise, depending on the amount and the cost of the material that will be removed during the experiment.

Milling machines and tools are designed according to the type of forces present at the tool-chip interface. The cutting force component is measured in the direction of the cutting speed and is used to determine the required force for the cutting operation. Although the magnitude and direction of all force components during cutting cannot be theoretically determined, dynamometers enable the measurement of thrust force and cutting force. Equations 3.10 to 3.13 allow the determination of friction force, normal force to friction, shear force and normal force to shear in cases where the cutting force and thrust force is known.

Modeling of cutting forces for drilling, milling and turning is a popular subject for researchers. Past papers provide ample groundwork to build on in terms of methodology when modeling. There are three types of approaches mainly used for cutting force modeling: Mechanistic, FEM and statistical. When taking into consideration an industrial engineering approach to answer the research questions of this thesis, it becomes apparent that the statistical methods discussed in this chapter offer a more suitable way forward in terms of modeling.

The literature review reveals that a reasonable amount of papers follow the response surface methodology. RSM provides an iterative sequence of arriving at an optimum solution for modeling a particular response surface and subsequently fitting a first, second, third or even fourth-order model of significance. The RSM technique in its entirety can become a lengthy process in terms of the number of experiments that are required to accurately model a specific response surface. The reason therefore is within the sequential experimental approach that needs to be followed before and after the application of the steepest ascent method. A well prepared full factorial design with centre points can provide information about the location of the optimum surface area by examining the curvature represented in the location of the central points.

CHAPTER 4

METHODOLOGY

4.1 INTRODUCTION

The experimental design is tailored to provide conclusive results for Ti-6Al-4V cutting experiments. The overall goal of the experiments is to: (1) Measure and inspect tool wear, chip formation, surface finish and tangential cutting forces, (2) Fit a statistical model to the experimental data for the purpose of cutting force prediction.

4.2 PREPARATION OF MATERIAL, TOOLS AND EQUIPMENT

The experimental design follows procedures set forth by ISO 8688-1 [55] and 8688-2 [57]. These guidelines are aimed at experimentation with end milling and face milling respectively. Important experimental design factors for consideration include: (1) Workpiece material properties, (2) Tool geometry and cutting edges, (3) Cutting fluid and lubricant, (4) Cutting strategy, (5) Tools and tool holders, and (6) Machine tool.

4.2.1   Workpiece Material

The workpiece material used for experiments is Ti-6Al-4V, grade 5. The required properties and specifications of the Ti-6Al-4V bar used for experiments are listed in Table 4.

Table 4: Workpiece material properties

Material	Ti-6Al-4V
Supplier	Sierra Alloys
Product Code	MIL T-90451
Grade	5
Condition	Annealed
Vickers Hardness (HV)	342.3
Rockwell Hardness (HRC)	34.7
Tensile Strength (N/mm$_2$)	1100.25
Chemical Composition	Al (6%) – Fe (0.25%) – O (0.2%) – Ti (90%) – V (4%)
Final Dimensions (W x L x H)	101.68 mm x 73.20 mm x 92.3 mm

The surface scale on the Ti-6Al-4V bar was removed prior to milling experiments. The hardness of the material was verified to confirm the information provided by the product data sheet. The testing zone Hardness testing was performed at five points along the centre line of the test zone or width of cut area as shown in Figure 44.

Hardness readings were taken on the testing zone before and after experiments, to check the hardness gradient throughout the workpiece. The average Vickers hardness of the uncut testing section was 342 HV and the average hardness of the cut section was 342.6 HV. The width of the cut is 43 mm. The marking out of the hardness testing points along the experimental area on the Ti-6al-4V sample is shown in Figure 44.
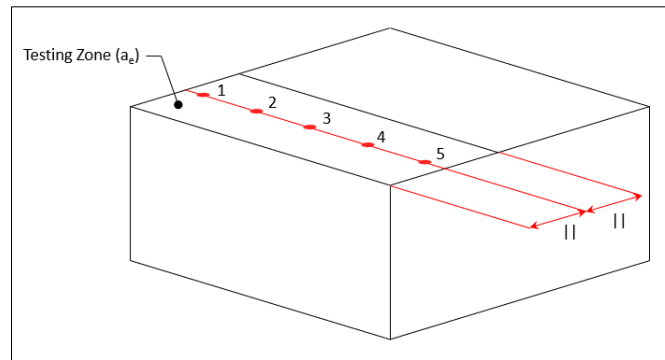
Figure 44: Material hardness testing procedure [55]

4.2.2   Tool Geometry and Cutting Edges

The Kennametal KSRM63A04RC20BB cutter body and RCGX2006M0SGF inserts as shown in Figure 45 is used for cutting experiments. The cutter is designed for machining with Ti-6Al-4V. Due to the large tool diameter and 20mm inserts, this tool is capable of high material removal rates at higher radial engagement.

Figure 45: Kennametal KSRM63A04RC20BB cutter geometry

The cutter has a neutral axial rake angle and neutral radial rake angle as shown in Figure 45. A neutral geometry is uncommon for a Ti-6Al-4V face milling cutters. In cases where a cutter has a positive axial rake angle, it usually ranges between 5° to 20° (positive) for Ti-6Al-4V purposes. Similarly, the radial rake angle ranges from 1° to 14° [79]. Kennametal developed the KSRM63A04RC20BB cutter body for through spindle cooling with split tools. This is achieved by channelling the coolant through the cutter body and out through the insert rake face as shown in Figure 46.
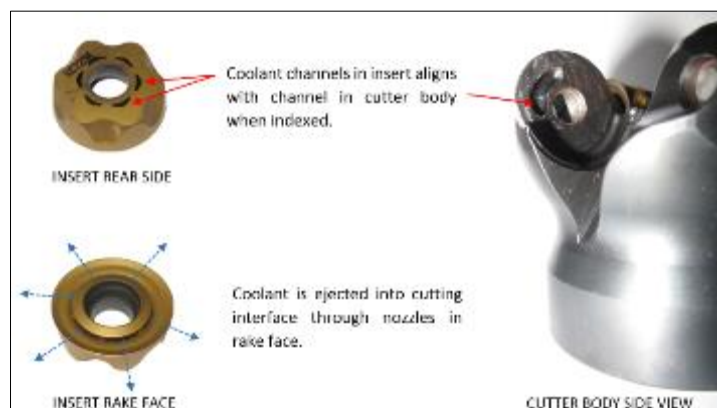
Figure 46: Insert coolant channel alignment with cutter body

The RCGX insert range is manufactured from carbide and the RCGX2006M0SGF inserts have a TiAlN coating which is applied by means of the Physical Vapour Deposition (PVD) process [80]. TiAlN is the next derivative coating of titanium nitride (TiN).

Horling, Hultman, Karlsson, Larsson, Mayrhofer, Mitterer, and Sjolen, found that TiAlN outperforms TiN coatings in high speed machining applications, because TiAlN coatings undergo "spinodal decomposition", that hardens the insert at elevated temperatures. Furthermore it was determined that TiAlN has higher resistance against oxidation due to the formation of an aluminium-oxide layer [81].

Figure 47: RCGX2006M0SGF insert [82]

The RCGX2006M0SGF insert is designed for heavy Ti-6Al-4V milling, hence its larger nose radius. These inserts each have six indexable positions with an anti-rotation notch in the cutter body. RCGX2006M0SGF inserts have a 0° rake angle and 7° relief angle [80] [82].

4.2.3   Milling Machine

Face milling experiments were conducted on a Hermle C40 milling machine in the Rapid Product Development Laboratory. The milling machine configuration for the experiments is summarized in Table 5.

Table 5: Milling machine configuration

Machine Tool	Hermle C40
Spindle	HSK A 63 (18 000 rpm/130 Nm/15 kW)
Coolant	Blaser Vasco 5000 (Diluted to 12% concentration)
Coolant Delivery	Through spindle, through insert (split tooling)
Coolant Pressure	65 Bar
Cutter	Kennametal KSRM63A04RC20BB
Inserts	Kennametal RCGX2006M0SGF
Radial Engagement	43 mm
Cutting Force Measurement	Kistler 9255C Dynamometer

The tangential cutting force was measured with a Kistler dynamometer attached between the Hermle C40 bed and the workpiece. A force signal cable connects the dynamometer and charge amplifier, which is connected to the data acquisition system (DAQ). The magnitude and direction of the cutting force

components are then communicated from the DAQ to the Dynoware software by USB interface. The force measurement system is summarised in Figure 48.
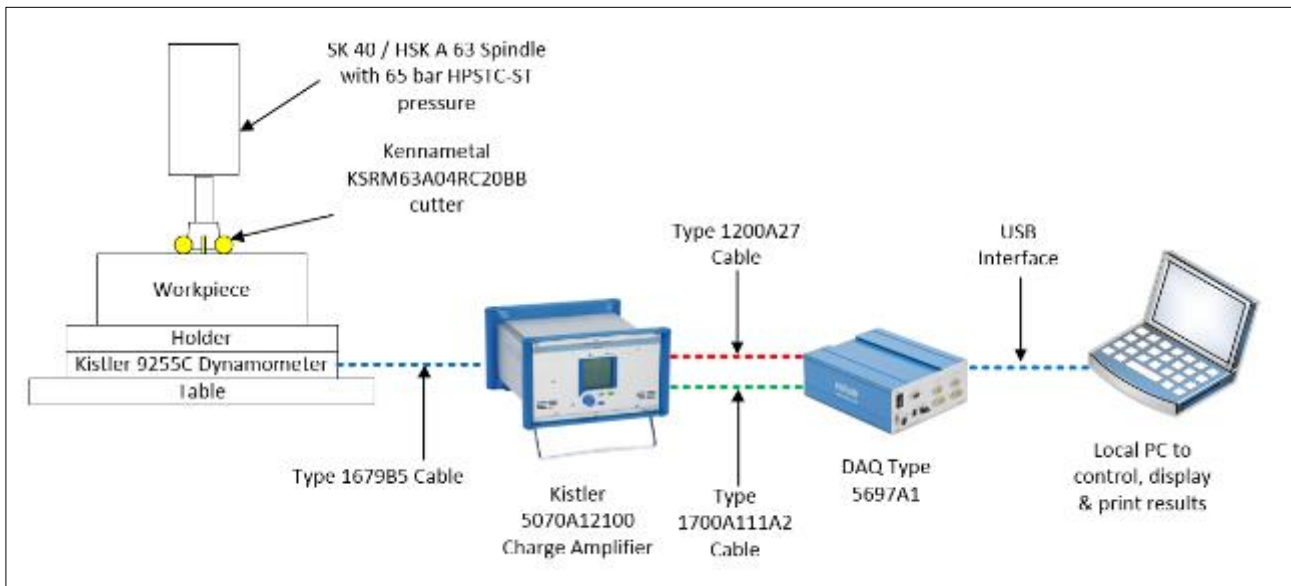
Figure 48: Force measurement experiment setup

The arithmetic mean surface roughness of the outside and inside diameter of each cut was measured with a Mitutoyo SJ-201P profilometer. The surface finish was measured after each run, because every successive cut creates its own surface finish, removing the previous surface. The average of three readings was taken on each side of the cut. The surface roughness of the inside diameter of the cut was labelled as Ra1 and the roughness of the outside diameter of the cut was labelled as Ra2.

The indexing of inserts after each experiment run enabled measurement of tool flank wear. Each insert has six indexable positions and each position was marked with a scriber. The marking of inserts followed an alpha numeric convention: Insert number, followed by the index position according to the alphabet. Insert three at index B would be labelled as 3B for example. Uniform tool wear measurements were made at six intervals along each insert's indexed flank and the average was measured with an Olympus GX51 microscope.

Machining chips were collected for analysis after each experiment run. The milling machine's table was cleaned with a high pressure nozzle after every experiment run, to prevent mixing of chips. The chips were stored in labelled plastic containers for microscope analysis. Chip formation and characteristics were examined with an Olympus SZX7 Zoom Stereo microscope.

4.2.4   Cutting Strategy

Straight cuts were performed for experiments. Each successive straight line cut was made on top of the previous cut. The radial engagement of 43 mm remained constant for all experiments as the cutting speed, ADOC and feedrate were varied according to the experimental design matrix. The cutter was not rolled into

cuts, hence thicker initial chips can be expected. The down milling technique, popular with Ti-6Al-4V milling, was used as described by Tschätsch and Reichelt [83].

4.3 EXPERIMENTAL DESIGN

4.3.1 Introduction

The pre-experimental planning was done by means of constructing a fish bone diagram of controllable, uncontrollable and constant factors. These factors are illustrated in Figure 49.
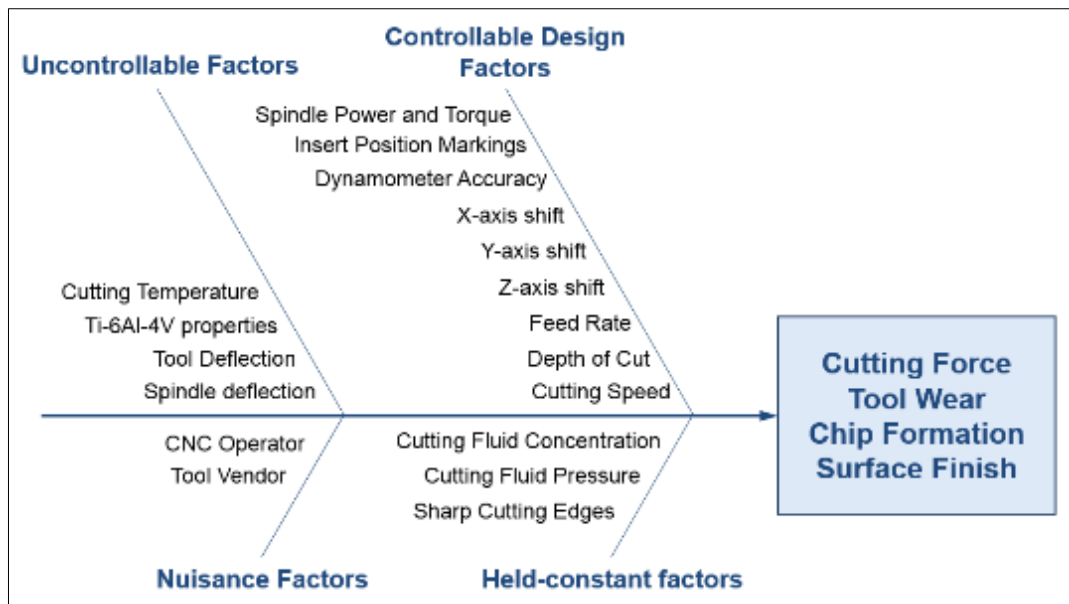
Figure 49: Experiment design factors

The choice of experimental design is determined by the desired sample size [75]. In this case, the high price and limited availability of Ti-6Al-4V in South Africa requires a small sample size. A full factorial design with three variables at two levels and three centre points (2^{3+3}) was chosen. This particular design was chosen, because it is the most efficient design for the study of two or more factors [75] [84]. The addition of centre points to the full factorial design enables curvature testing. This provides an indication of how far the selected response surface is from a change in the sign of the gradient, indicating a possible optimum [75] [76] [85] [77] [78].

4.3.2 Research Hypothesis

If both the curvature and lack of fit is not significant, while the model is found to be significant, then a first-order model accurately represents the optimal response surface of tangential cutting forces. On the other hand, if there is significant curvature, the first-order model, despite being fitted significantly to the current response surface, does not represent the optimum response surface [75] [85]. Therefore the following hypothesis can be derived:

H_0: *A first-order model significantly represents the optimal response surface of tangential cutting forces.*

H₁ : A first-order model represents a response surface different from the optimum of tangential cutting forces.

4.3.3 Research Methodology for Statistical Modeling

The chosen methodology follows the steps shown in Figure 50. Response surface methodology (RSM) cannot be followed in its entirety due to the amount of experiments required to determine the optimum response surface by means of the steepest ascent method. The methodology provides a best model fit solution for the given design space by means of systematic increase of the model order if a better fit is required.
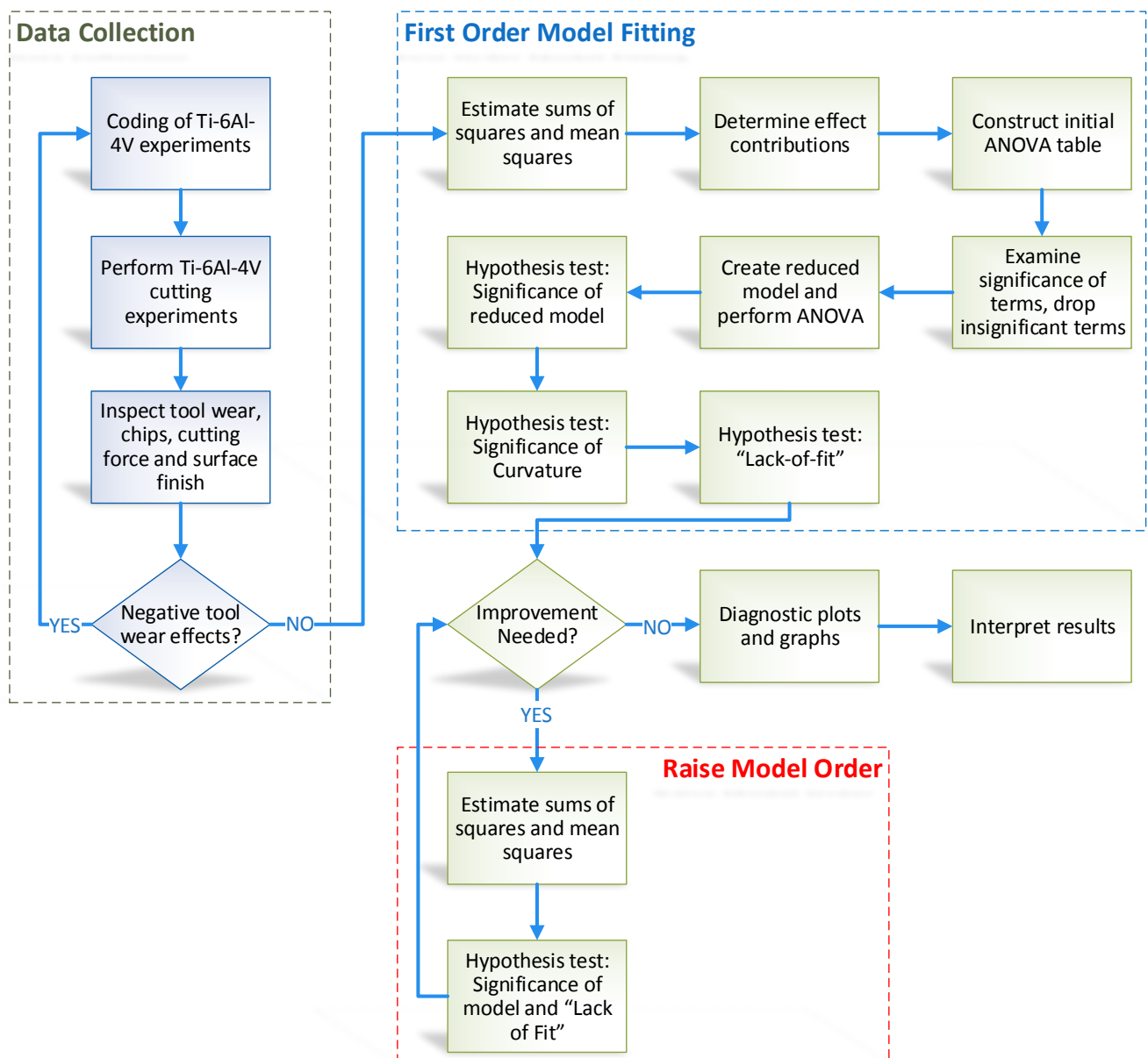
Figure 50: Research methodology

4.3.4 Coding of Experimental Matrix

The variables chosen for experimentation are feed per tooth (f_z), ADOC (a_p) and cutting speed (v_c). The measured response is tangential cutting force (F_x). Using orthogonal coding, the low and high levels of the factors are listed for eight runs as shown in Table 6. The addition of centre points to the factorial design, allows an independent estimate of error to be calculated [75].

Table 6: Coding of the design matrix.

	CODED FACTORS			Effect Labels	FACTOR LEVELS			
Run	A (a_p)	B (f_z)	C (v_c)		Factor	Low (-)	High (+)	Centre (0)
1	—	—	—	(1)	A (a_p mm)	0.50	2.50	1.50
2	+	—	—	a	B (f_z mm)	0.05	0.15	0.10
3	—	+	—	b	C (v_c m/min)	55.00	99.29	77.15
4	+	+	—	ab				
5	—	—	+	c				
6	+	—	+	ac				
7	—	+	+	bc				
8	+	+	+	abc				
9	0	0	0	Centre				
10	0	0	0	Centre				
11	0	0	0	centre				

4.3.5 Cutting Experiment Worksheet

The experimental design run chart, as shown in Table 7, was developed using the Design Expert 7 software package from Stat-Ease. Values under the heading "Exp." is the order from 1 to 11 in which experiments were performed. The "Run" order follows the standard full factorial (2^{3+3}) design matrix according to Table 6.

Table 7: Experimental design run chart

		Factors			Effect
Exp.	Run	A (a_p)	B (f_z)	C (v_c)	Labels
10	1	0.50	0.05	55.00	(1)
3	2	2.50	0.05	55.00	a
1	3	0.50	0.15	55.00	b
2	4	2.50	0.15	55.00	ab
6	5	0.50	0.05	99.29	c
9	6	2.50	0.05	99.29	ac
4	7	0.50	0.15	99.29	bc
5	8	2.50	0.15	99.29	abc
7	9	1.50	0.10	77.15	Centre
11	10	1.50	0.10	77.15	Centre
8	11	1.50	0.10	77.15	Centre

CHAPTER 4: METHODOLOGY

The tangential cutting forces are recorded for each experiment. Analysis of the machinability factors determines if the measured forces are acceptable for modeling purposes. If the machinability analysis provides evidence of catastrophic tool failures, high temperatures or abnormal chip formation, then the recorded cutting forces are rejected and adjustments need to be made to the face milling experimental design run chart. If no problems are observed during the machining of the Ti-6Al-4V, then the tangential cutting force data is useful for the purpose of statistical modeling.

CHAPTER 5

EXPERIMENTAL RESULTS AND STATISTICAL MODELING

5.1 SURFACE FINISH

Ra1 is lowest at high ADOC, high cutting speed and low feedrate as shown in Figure 51. Alternatively Ra1 is highest at medium ADOC, medium cutting speed and medium-to-high feedrate. Figure 51 shows agreement with findings from the literature review: surface roughness is primarily affected by feedrate.
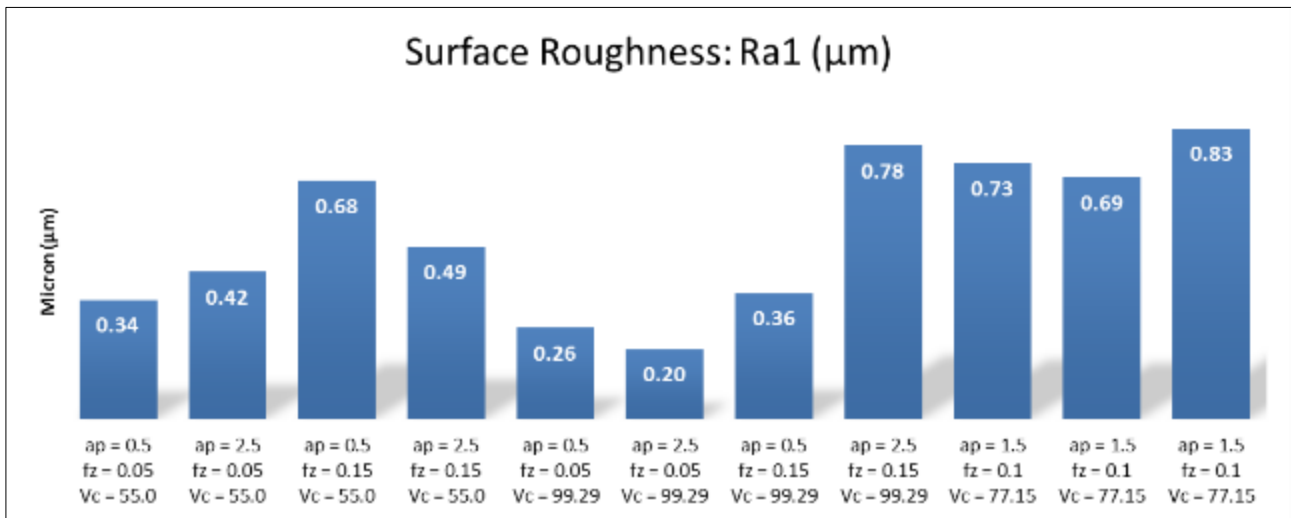
Figure 51: Surface roughness measured on inside diameter of cut (Ra1)

The measured surface roughness on the outside diameter (Ra2) also suggests feedrate as a primary affecting factor as shown in Figure 52. The surface roughness is greatest with high-to-medium feedrates and surface roughness is lower with smaller feedrates. It is also observed that high ADOC increases surface roughness along with higher feedrates. The maximum recorded surface roughness is 1.26 µm as shown in Figure 52, while the minimum recorded surface roughness was 0.2 µm as shown in Figure 51.
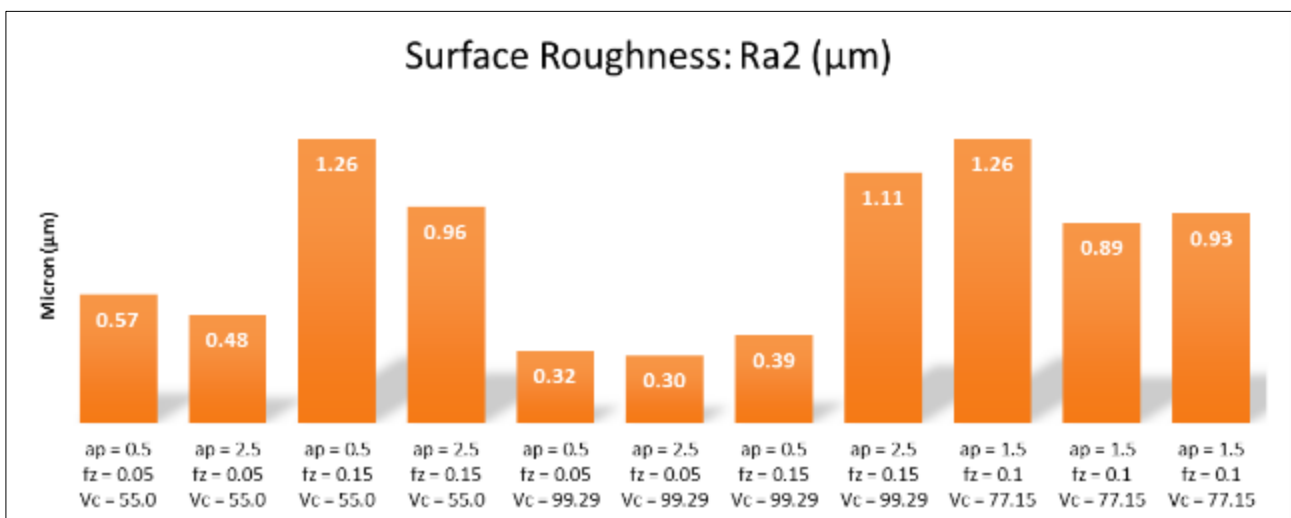
Figure 52: Surface roughness measured on outside diameter of cut (Ra2)

The recorded data for surface roughness confirms that the Kennametal KSRM63A04RC20BB cutter with RCGX2006M0SGF inserts is able to perform semi finishing and finishing of machined surfaces. Typical surface finish for components manufactured by the Daliff Engineering industry partner ranges from 1.6 µm to 3 µm.

5.2 TOOL WEAR

Uniform tool wear measurements were made at six intervals along each insert's indexed flank and the average was recorded as shown in Figure 54.
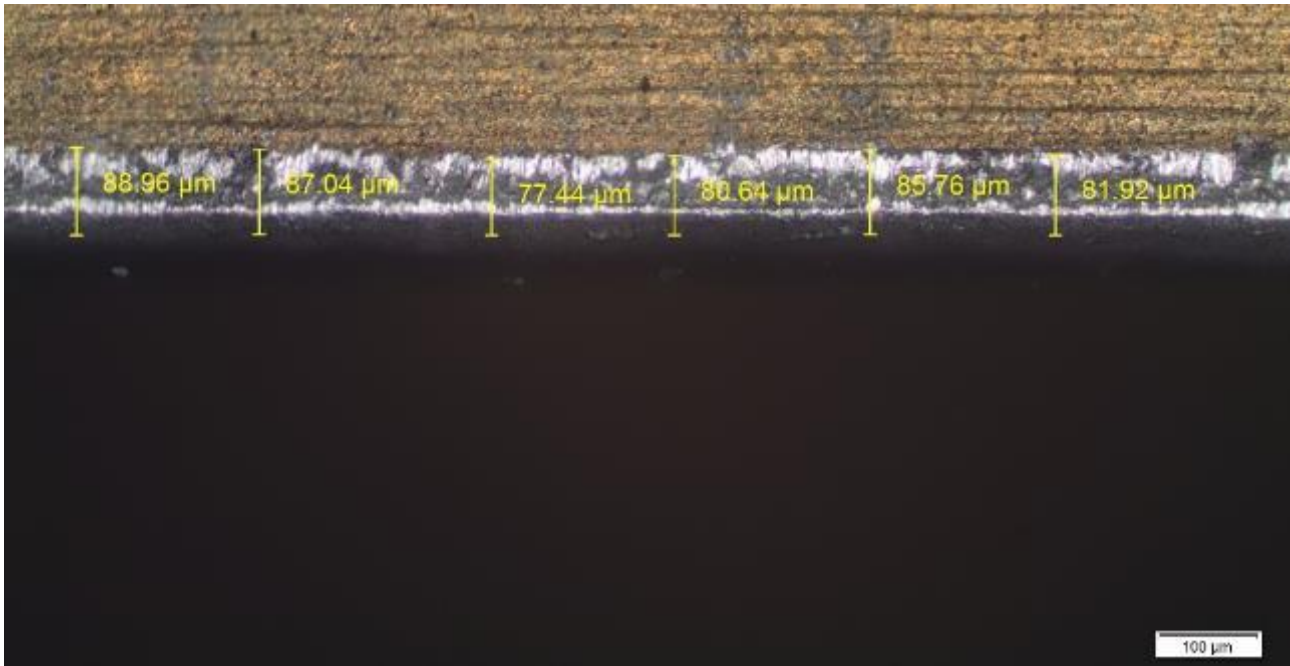
Figure 53: Experiment run 2, Insert 3, index B: Six uniform wear measurements along flank (at 100 µm)

Cutting experiment duration ranged from 18 seconds to 97 seconds, which represents the tool break-in period as discussed in section 3.4.1 and illustrated in Figure 27. Therefore, the data recorded for the purpose of tool wear examination cannot be used to model tool wear rate prediction. However the microscope analysis of the insert flanks is required to assess if tangential cutting force measurements were conducted under ideal or normal conditions. If there were to be chatter or heat induced tool failures, the accuracy of the tangential cutting force measurement data becomes questionable.

Examination of the flank wear types gives an indication of conditions at the cutting interface. Uniform flank wear was observed during all 11 runs. Non uniform flank wear was also observed in four separate runs, but in negligible magnitudes of 5 µm to 10 µm in the worst cases. These observations were therefore omitted from results. Figure 54 shows that tool wear rate is affected by the cutting variables ADOC, feedrate and cutting speed.
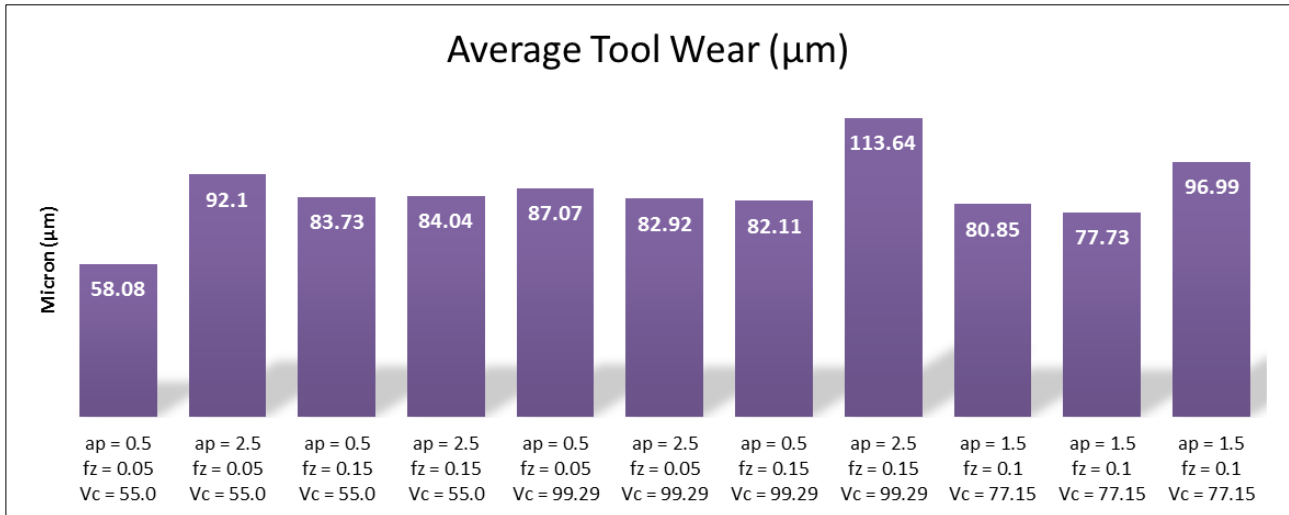
Figure 54: Average tool wear for experimental runs

The average uniform tool wear graph (Figure 54) shows that maximum tool wear rate was observed at high levels for feedrate, ADOC and cutting speed. Conversely, the lowest tool wear rate was observed at low feedrate, low ADOC and low cutting speed. The microscope analysis therefore concludes that cutting conditions were normal and tangential force measurements are accurate enough to perform modeling of the data.
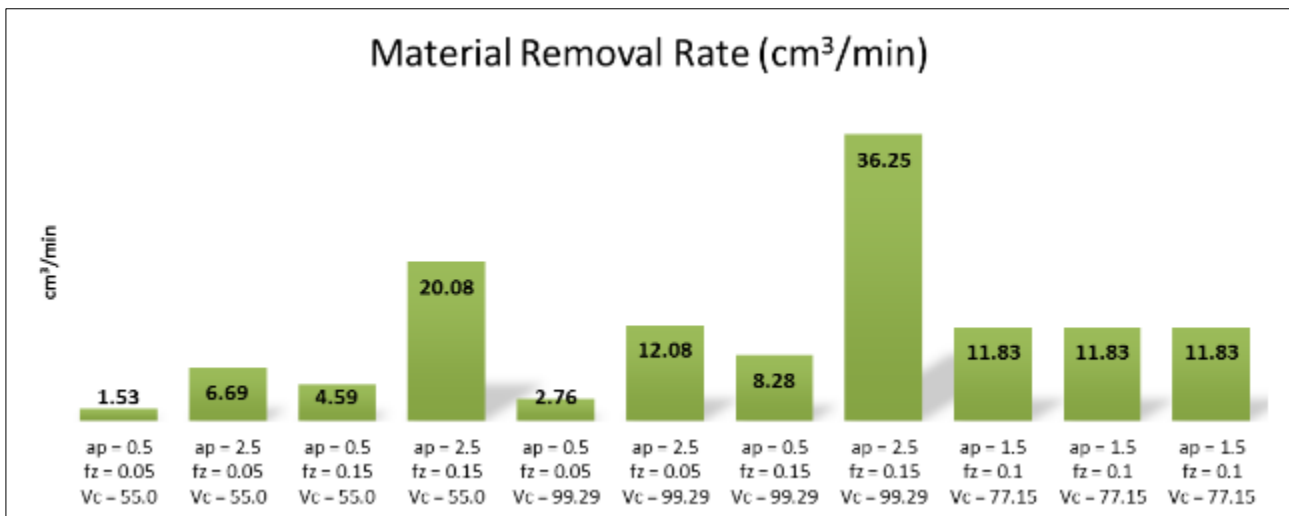
Figure 55: Material removal rate per experimental run

The MRR's for experiments are shown in Figure 55. The highest MRR of 36.25 cm^3/min is in agreement with Kennametal's marketed MRR for Beyond Blast cutters.

5.3 CHIP CONTROL AND CHARACTERISTICS

Serrated chips were observed during all experiment runs with some shearing at higher ADOC and cutting speeds. No BUE or continuous chips were observed.
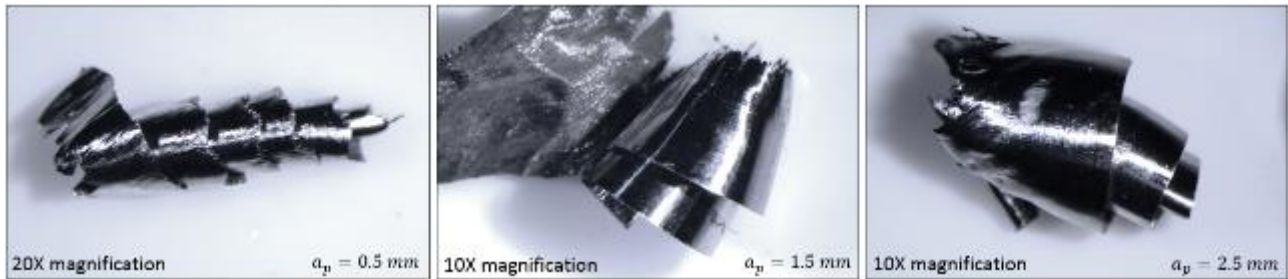
Figure 56: Chip width at varying ADOC

It was found that the chip width increased with higher ADOC and decreased with lower ADOC as shown in Figure 56. The chip length increased with cutting speed and deformation of chips were observed at the highest level of cutting speed as shown in Figure 57. This deformation of the edge can be attributed to the observed shearing of the chips at high cutting speeds.

Figure 57: Chip length at varying cutting speeds

Segmentation was only observed at cutting speeds beyond 55 m/min. This is in agreement with findings from literature. The feedrate also has an impact on the pitch of the segments. Higher feedrates cause higher segment pitches or a more prominent saw tooth effect, while lower feedrates have the opposite effect as shown in Figure 58.
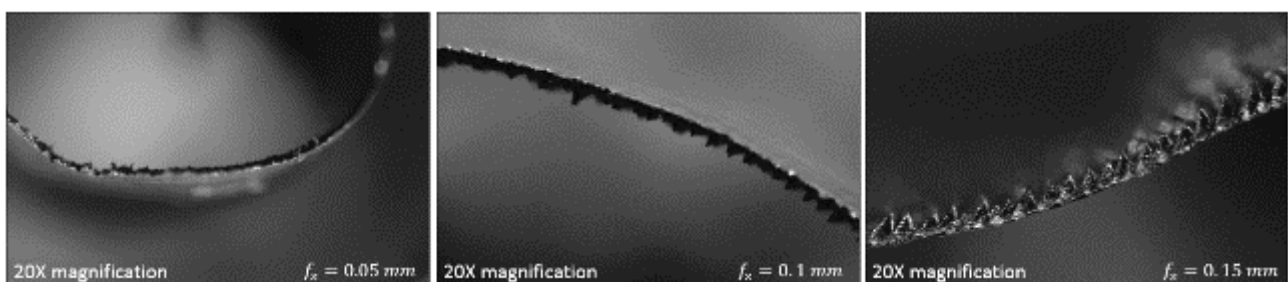
Figure 58: Chip segmentation at varying feedrates

No discoloration of any chips were observed. This is evidence of low cutting temperatures at the cutting interface. High cutting temperatures usually cause a yellow to brown discoloration of Ti-6Al-4V chips. The chips that were collected were discontinuous, but not short, indicating that the cutter and inserts performed adequate chip control. Few chips collected on the milling machine table and the workpiece itself during experiments. The beyond blast coolant delivery method and coolant pressure of 65 bar thus removed chips from the cut very effectively. It is therefore expected that very few chips were re-cut contributing to better tool life.

CHAPTER : EXPERIMENTAL RESULTS AND STATISTICAL MODELING

5.4 CUTTING FORCE MEASUREMENTS

The cutting force data was recorded and plotted with Kistler Dynoware as shown in Figure 59. The average tangential cutting force (F_x), which is the force in the direction of the cut, was measured using the software's mean force measurement add-in.
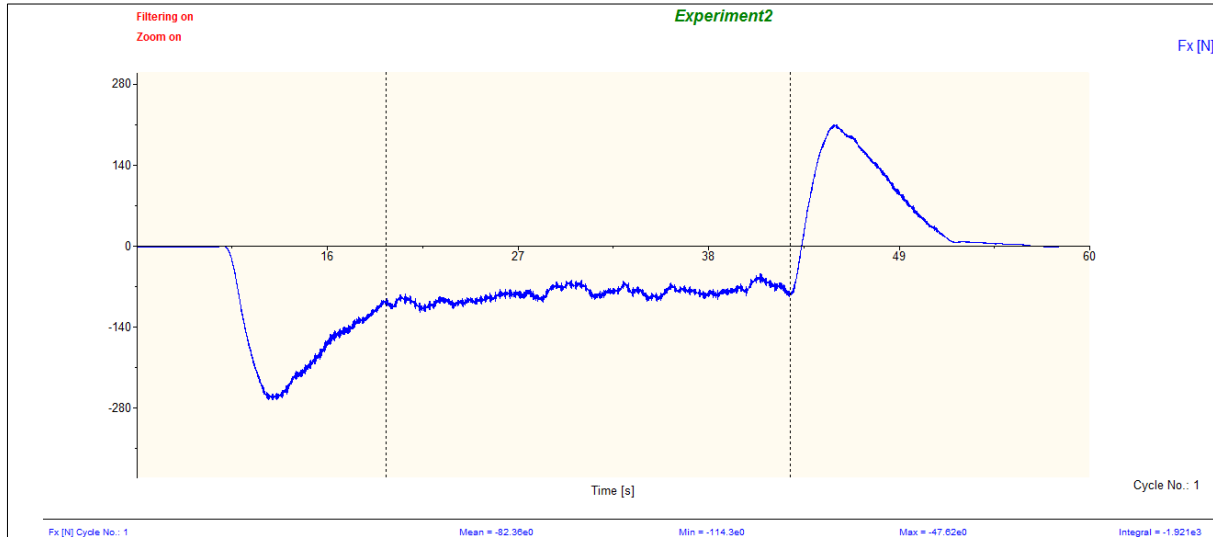
Figure 59: Dynoware cutting force signal measurement

A low pass signal filter was applied to remove signal noise and the graph was corrected for signal drift. The mean force was measured for the duration of full tool engagement with the workpiece. The impact forces during tool entrance and exit with respect to the cut were omitted from the analysis and the average tangential cutting force during full engagement was recorded as indicated by the two vertical lines in Figure 59. The recorded tangential cutting forces for each experiment run are summarised in Table 8.

Table 8: Tangential force measurement results

Experiment	Factors			Response
Run	A (a_p)	B (f_z)	C (v_c)	F_x
1	0.50	0.05	55.00	27.00
2	2.50	0.05	55.00	88.34
3	0.50	0.15	55.00	17.73
4	2.50	0.15	55.00	82.36
5	0.50	0.05	99.29	21.69
6	2.50	0.05	99.29	68.28
7	0.50	0.15	99.29	40.13
8	2.50	0.15	99.29	92.60
9	1.50	0.10	77.15	3.64
10	1.50	0.10	77.15	7.67
11	1.50	0.10	77.15	0.51

The results show that the highest force was measured at the high level of the coded variables (experiment run 8, with 92.6N). Lowest cutting forces were measured at the centre points.

5.5 STATISTICAL MODELING

Examination of the experimental results for the surface finish, chip formation, tool wear and cutting force reveal no undesired tool wear effects or distortions. Good surface finish was also achieved and chip colouration provides evidence of low temperatures at the cutting interface. The tangential cutting force data from the laboratory experiments is therefore used in creating a model for the purpose of cutting force prediction. The methodology illustrated in Figure 50 is followed for modeling purposes.

5.5.1   Estimation of the Sums of Squares

A power transformation was initially applied to the data, because the responses followed a left-skewed normal distribution [75] [76]. The cutting force data is illustrated in the design matrix as shown in Figure 60.
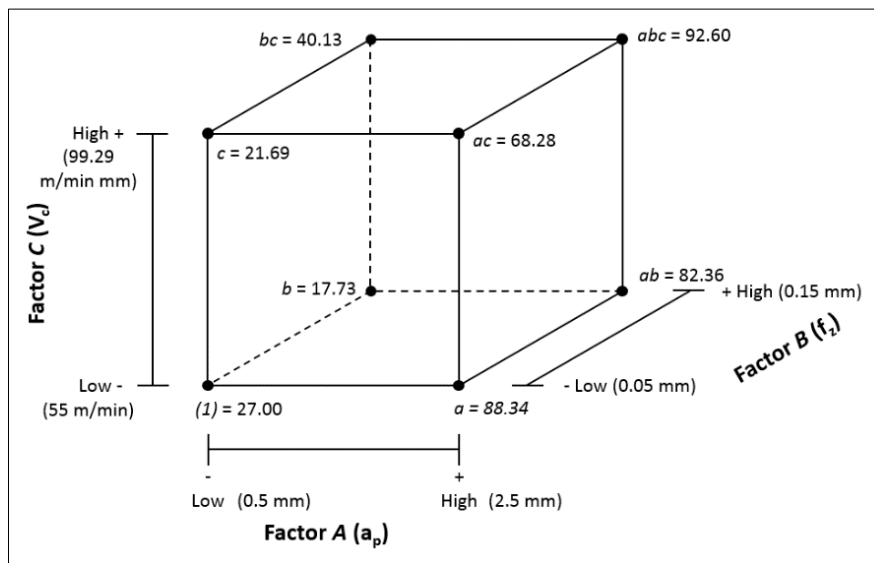
Figure 60: Geometric view of the design matrix

ANOVA is performed to determine the mean sum of squares, mean squares (MS's), F-values and p-values. The centre points are used to determine the curvature and pure error of the model. The average estimated effect of A is:

$$A = \frac{1}{4n}[a - (1) + ab - b + ac - c + abc - bc]$$

[Eq. 5.1]

Where A is an estimated effect factor, n is the number of experimental replications and a, b, c and (1) are the labels given to interaction levels as shown in Figure 60. The estimated effect of A is:

$$A = \frac{1}{4(1)}[88.34 - 27.00 + 82.36 - 17.73 + 68.28 - 21.69 + 92.60 - 40.13]$$

$$= \frac{1}{4}[225.03] = 56.26$$

Similarly, the remaining estimated effects are calculated:

$$B = \frac{1}{4n}[b + ab + bc + abc - (1) - a - c - ac]$$

[Eq. 5.2]

$$B = \frac{1}{4(1)}[17.73 + 82.36 + 40.13 + 92.60 - 27.00 - 88.34 - 21.69 - 68.28] = 6.88$$

$$= \frac{1}{4}[27.51] = 6.88$$

$$C = \frac{1}{4n}[c + ac + bc + abc - (1) - a - b - ab]$$ [Eq. 5.3]

$$C = \frac{1}{4(1)}[21.69 + 68.28 + 40.13 + 92.60 - 27.00 - 88.34 - 17.73 - 82.36]$$

$$= \frac{1}{4}[7.27] = 1.82$$

$$AB = \frac{1}{4n}[ab - a - b + (1) + abc - bc - ac + c]$$ [Eq. 5.4]

$$AB = \frac{1}{4(1)}[82.36 - 88.34 - 17.73 + 27.00 + 92.60 - 40.13 - 68.28 + 21.69]$$

$$= \frac{1}{4}[9.17] = 2.29$$

$$AC = \frac{1}{4n}[(1) - a + b - ab - c + ac - bc + abc]$$ [Eq. 5.5]

$$AC = \frac{1}{4(1)}[27.00 - 88.34 + 17.73 - 82.36 - 21.69 + 68.28 - 40.13 + 92.60]$$

$$= \frac{1}{4}[-26.91] = -6.73$$

$$BC = \frac{1}{4n}[(1) + a - b - ab - c - ac + bc + abc]$$ [Eq. 5.6]

$$BC = \frac{1}{4(1)}[27.00 + 88.34 - 17.73 - 82.36 - 21.69 - 68.28 + 40.13 + 92.60]$$

$$= \frac{1}{4}[58.01] = 14.50$$

$$ABC = \frac{1}{4n}[abc - bc - ac + c - ab + b + a - (1)]$$ [Eq. 5.7]

$$ABC = \frac{1}{4(1)}[92.60 - 40.13 - 68.28 + 21.69 - 82.36 + 17.73 + 88.34 - 27.00]$$

$$= \frac{1}{4}[2.59] = 0.65$$

The sums of squares are calculated, using the average estimate effects. The formula for calculating the sum of squares is:

$$SS = \frac{(Contrast)^2}{8n}$$ [Eq. 5.8]

$$SS_A = \frac{(225.03)^2}{8(1)} = 6329.81$$

$$SS_B = \frac{(27.51)^2}{8(1)} = 94.60$$

$$SS_C = \frac{(7.27)^2}{8(1)} = 6.61$$

$$SS_{AB} = \frac{(9.17)^2}{8(1)} = 10.51$$

$$SS_{AC} = \frac{(-26.91)^2}{8(1)} = 90.52$$

$$SS_{BC} = \frac{(58.01)^2}{8(1)} = 420.65$$

$$SS_{ABC} = \frac{(2.59)^2}{8(1)} = 0.84$$

$$SS_{Model} = SS_A + SS_B + SS_C + SS_{AB} + SS_{AC} + SS_{BC} + SS_{ABC}$$

$$= 6329.81 + 94.60 + 6.61 + 10.51 + 90.52 + 420.65 + 0.84$$

$$= 6953.53$$

The three centre points are taken into account for the calculation of the sum of squares for the curvature:

$$\bar{y}_C = \frac{3.64 + 7.67 + 0.51}{3}$$

$$= 3.94$$

The average of the eight factorial runs is:

$$\bar{y}_F = \frac{27.00 + 88.34 + 17.73 + 82.36 + 21.69 + 68.28 + 40.13 + 92.60}{8}$$

$$= 54.77$$

There is a large difference between $\bar{y}_C$ and $\bar{y}_F$. It suggests significant curvature. To verify this, the pure quadratic sum of squares or sum of squares of the curvature is calculated:

$$SS_{Curve} = \frac{n_F n_C (\bar{y}_F - \bar{y}_C)^2}{n_F + n_C}$$ [Eq. 5.9]

$$= \frac{(8)(3)(54.77 - 3.94)^2}{8 + 3}$$

$$= 5636.49$$

Where n_F is the number of factorial runs, n_C is the number of centre points, $\bar{y}_F$ is the average of the factorial runs, and $\bar{y}_C$ is the average of the centre points.

The total sum of squares is calculated by taking the centre points into account. The total sum of squares or SS_T for three variables is:

$$SS_T = \sum_{i=1}^{a}\sum_{j=1}^{b}\sum_{k=1}^{c}\sum_{l=1}^{n} y_{ijkl}^2 - \frac{y^2\cdots}{abcn}$$
[Eq. 5.10]

$$= (27.00 - 40.90)^2 + (88.34 - 40.90)^2 + \cdots + (7.67 - 40.90)^2 + (0.51 - 40.90)^2$$

$$= 12615.85$$

SS_E is determined by means of subtraction:

$$SS_{Total} = SS_{Model} + SS_{Curve} + SS_{Error}$$
[Eq. 5.11]

$$12615.85 = 6953.53 + 5636.49 + SS_{Error}$$

$$SS_{Error} = 25.83$$

5.5.2 Estimation of the Mean Squares

Each of the models terms A,B,C, AB, AC, BC and ABC has 1 degree of freedom, including the curvature. The total degrees of freedom is equal to the amount of observations, less 1. Therefore the degrees of freedom for the error is $10 - 8 = 2$. The degrees of freedom are:

$$df_{Total} = n - 1$$
[Eq. 5.12]

$$df_A = a - 1$$
[Eq. 5.13]

$$df_B = b - 1$$
[Eq. 5.14]

$$df_C = c - 1$$
[Eq. 5.15]

$$df_{AB} = (a - 1)(b - 1)$$
[Eq. 5.16]

$$df_{AC} = (a - 1)(c - 1)$$
[Eq. 5.17]

$$df_{BC} = (b - 1)(c - 1)$$
[Eq. 5.18]

$$df_{ABC} = (a - 1)(b - 1)(c - 1)$$
[Eq. 5.19]

$$df_{Curve} = a - 1$$
[Eq. 5.20]

$$df_{Error} = abc(n - 1)$$
[Eq. 5.21]

CHAPTER : EXPERIMENTAL RESULTS AND STATISTICAL MODELING

MS for each term is calculated by dividing each sum of squares by its degrees of freedom. The formula for the MS is:

$$MS = \frac{sum\ of\ squares}{degrees\ of\ freedom} = \frac{SS}{df}$$

[Eq. 5.22]

The MSE of all the factors is calculated by using the df's from equations 5.12-5.22:

$$MS_A = \frac{6329.81}{1} = 6329.81$$

$$MS_B = \frac{94.60}{1} = 94.60$$

$$MS_C = \frac{6.61}{1} = 6.61$$

$$MS_{AB} = \frac{10.51}{1} = 10.51$$

$$MS_{AC} = \frac{90.52}{1} = 90.52$$

$$MS_{BC} = \frac{420.65}{1} = 420.65$$

$$MS_{ABC} = \frac{0.84}{1} = 0.84$$

$$MS_{Curve} = \frac{5636.49}{1} = 5636.49$$

$$MS_{Error} = \frac{25.83}{2} = 12.91$$

$$MS_{Model} = \frac{6953.53}{7} = 993.36$$

5.5.3   Effect Contributions and Initial ANOVA

The effect estimates and the sums of squares are summarized in Table 9.

Table 9: First-order model, effect estimate summary

Factor	Effect Estimate	Sum of Squares	Percent Contribution
A	56.26	6329.81	50.17
B	6.88	94.60	0.75
C	1.82	6.61	0.052
AB	2.29	10.51	0.083
AC	-6.73	90.52	0.72
BC	14.50	420.65	3.33
ABC	0.65	0.84	0.006

The effect estimate summary table is a rough but effective tool to determine the relative importance of each model term. Effects A, B, AC, BC and curvature seem to be significant terms according to Table 9. The complete ANOVA table provides proof, by means of F-values and p-values.

Table 10: ANOVA for preliminary first-order factorial model

Source	Sum of Squares	df	Mean Square	F-Value
Model	6953.53	7	993.36	76.92
A-a_p	6329.81	1	6329.81	490.13
B-f_z	94.60	1	94.60	7.33
C-v_c	6.61	1	6.61	0.51
AB	10.51	1	10.51	0.81
AC	90.52	1	90.52	7.01
BC	420.65	1	420.65	32.57
ABC	0.84	1	0.84	0.06
Curvature	5636.49	1	5636.49	436.45
Pure Error	25.83	2	12.91	
Total	12615.85	10		

5.5.4   Significance of Terms

The significance of each term with respect to the model should be checked. Non-significant terms do not affect the model at the 95% confidence level. The p-value of each term is calculated to determine if they should form part of the revised model or not.

Table 10 shows the F-Value for the model factor. This is the summary for the overall model. It is already known that $SS_{Model} = SS_A + SS_B + SS_C + SS_{AB} + SS_{BC} + SS_{ABC} = 6953.53$. Two hypotheses test the model and the curvature of the preliminary first-order factorial model.

The F-statistic is used during ANOVA. MS_{Error} is used as denominator in all hypotheses about the significance of the model terms. This is the statistical error, and represents the difference between the model and the unobservable population mean. Alternatively, when calculating the F-value for individual terms such as the curvature or lack-of-fit, then MS_{Res} is used as denominator. This is the residual that is the difference between the term in question and the sample mean.

The critical values for the subsequent F-tests are determined by reading the corresponding values from the supporting table in Appendix A [76].

The hypothesis to determine the significance of the model is:

- The parameter of interest is the model terms.
- Thus the test statistic,

$$F_0 = \frac{MS_{Model}}{MS_{Error}}$$

- Tests the hypotheses,

$$H_0 : \beta_1 = \beta_2 = \beta_3 = \beta_{12} = \beta_{13} = \beta_{23} = \beta_{123} = 0$$

$$H_1 : at\ least\ one\ \beta \ \neq 0$$

- The selected confidence level is 95% ($\alpha = 0.05$).

- Reject H_0 if $F > F_{critical}$ where $F_{0.05,7,2} = 19.35$
- $MS_{Model} = 993.36, MS_{Error} = 12.91$

$$F_0 = \frac{MS_{Model}}{MS_{Error}} = \frac{993.36}{12.91} = 76.92$$

- The p-value is 0.0129.
- Since $F = 76.92$ and $76.92 > 19.35$, reject null hypothesis and conclude that the model is significant. The p-value of 0.0129 indicates that there is only a 1.29% chance that a Model F-Value this large could occur due to noise.

The hypothesis for the test of curvature is:

- The parameter of interest is the curvature term of the model equation.
- Thus the test statistic,

$$F_0 = \frac{MS_{Curve}}{MS_{Error}}$$

- Tests the hypotheses,

$$H_0: \sum_{j=1}^{k} \beta_{jj} = 0$$

$$H_1: \sum_{j=1}^{k} \beta_{jj} \neq 0$$

- The selected confidence level is 95% ($\alpha = 0.05$).
- Reject H_0 if $F > F_{critical}$ where $F_{0.05,1,2} = 18.51$
- $MS_{Curve} = 5636.49, MS_{Error} = 12.91$

$$F_0 = \frac{MS_{Model}}{MS_{Error}} = \frac{5636.49}{12.91} = 436.45$$

- The p-value is 0.0023.
- Since $F = 436.45$ and $436.45 > 18.51$, reject null hypothesis and conclude: There is significant curvature as measured by the difference between the average of the centre points and the average of the factorial points in the design space. There is only a 0.23% chance that a curvature F-value this large could occur due to noise.

Similarly, the p-values for the remaining terms (A, B, C, AB, AC, BC and ABC) are all calculated to determine their respective significance for consideration in the revised model. The p-values are summarized in Table 11 for length considerations. The ANOVA shown in Table 10 shows all of the p-values and indicate individual term significance.

Table 11: First-order ANOVA including p-values, indicating significant terms

Source	Sum of Squares	df	Mean Square	F-Value	p-value Prob > F	Comment
Model	6953.53	7	993.36	76.92	0.0129	Significant
A-a_p	6329.81	1	6329.81	490.13	0.0020	Significant
B-f_z	94.60	1	94.60	7.33	0.1137	Not significant
C-v_c	6.61	1	6.61	0.51	0.5487	Not significant
AB	10.51	1	10.51	0.81	0.4622	Not significant
AC	90.52	1	90.52	7.01	0.1180	Not significant
BC	420.65	1	420.65	32.57	0.0294	Significant
ABC	0.84	1	0.84	0.06	0.8227	Not significant
Curvature	5636.49	1	5636.49	436.45	0.0023	Significant
Pure Error	25.83	2	12.91			
Total	12615.85	10				

5.5.5 Non-significant Terms

According to the rough estimate of Table 9, the significant terms are A, BC and curvature. However calculations of the p-values have verified that the significant terms possess p-values smaller or equal to 0.05 (95% confidence level). Therefore, the terms B, C, AB, AC and ABC are not significant terms and are omitted from the first-order model equation. Nevertheless, due to the hierarchical limit of the terms, B and C cannot be omitted from the reduced model despite their low significance. The initial ANOVA is revised to exclude these terms.

5.5.6 ANOVA for Reduced Model

The non-significant terms are omitted. The sum of squares for the remaining terms are unchanged and the sum of squares for the lack of fit is calculated by subtraction.

$$SS_{LoF} = SS_{Total} - SS_{Model} - SS_{Curve} - SS_{Error} \qquad \text{[Eq. 5.23]}$$

Where, $SS_{Total} = 12615.85$, $SS_{Model} = 6851.66\,(A + B + C + BC)$, $SS_{Curve} = 5636.49$, $SS_{Error} = 25.83$ from Table 11. Thus:

$$SS_{LoF} = 12615.85 - 6851.66 - 5636.49 - 25.83 = 101.87$$

The MSE of all the remaining factors is re-calculated by using equations 5.12-5.22. Three degrees freedom are assigned to lack of fit for the three omitted terms.

$$MS_A = \frac{6329.81}{1} = 6329.81$$

$$MS_B = \frac{94.60}{1} = 94.60$$

$$MS_C = \frac{6.61}{1} = 6.61$$

$$MS_{BC} = \frac{420.65}{1} = 420.65$$

$$MS_{Curve} = \frac{5636.49}{1} = 5636.49$$

$$MS_{LoF} = \frac{101.87}{3} = 33.96$$

$$MS_{Error} = \frac{25.83}{2} = 12.91$$

$$MS_{Res} = \frac{127.70}{5} = 25.54$$

$$MS_{Model} = \frac{6851.66}{4} = 1712.92$$

The F-Values and p-values for the reduced ANOVA are required. The hypothesis to determine the significance of the model is:

- The parameter of interest is the model terms.
- Thus the test statistic,

$$F_0 = \frac{MS_{Model}}{MS_{Error}}$$

- Tests the hypotheses,

$$H_0 : \beta_1 = \beta_2 = \beta_3 = \beta_{12} = \beta_{13} = \beta_{23} = \beta_{123} = 0$$
$$H_1 : at\ least\ one\ \beta \neq 0$$

- The selected confidence level is 95% ($\alpha = 0.05$).
- Reject H_0 if $F > F_{critical}$ where $F_{0.05,4,2} = 19.25$
- $MS_{Model} = 1712.92, MS_{Error} = 12.91$

$$F_0 = \frac{MS_{Model}}{MS_{Error}} = \frac{1712.92}{12.91} = 67.07$$

- The p-value is 0.01474.
- Since $F = 67.07$ and $67.07 > 19.25$, reject null hypothesis and conclude that the model is significant. The p-value of 0.01474 indicates that there is only a 1.47% chance that a Model F-Value this large could occur due to noise.

The hypothesis for the test of curvature is:

- The parameter of interest is the curvature term of the model equation.
- Thus the test statistic,

$$F_0 = \frac{MS_{Curve}}{MS_{Res}}$$

- Tests the hypotheses,

CHAPTER : EXPERIMENTAL RESULTS AND STATISTICAL MODELING

$$H_0: \sum_{j=1}^{k} \beta_{jj} = 0$$

$$H_1: \sum_{j=1}^{k} \beta_{jj} \neq 0$$

- The selected confidence level is 95% ($\alpha = 0.05$).

- Reject H_0 if $F > F_{critical}$ where $F_{0.05,1,5} = 6.61$

- $MS_{Curve} = 5636.49, MS_{Res} = 25.54$

$$F_0 = \frac{MS_{Curve}}{MS_{Res}} = \frac{5636.49}{25.54} = 220.69$$

- The p-value is 0.000025.

- Since $F = 220.69$ and $220.69 > 6.61$, reject null hypothesis and conclude: There is significant curvature as measured by the difference between the average of the centre points and the average of the factorial points in the design space. There is only a 0.01% chance that a curvature F-value this large could occur due to noise.

The hypothesis for the test of lack of fit is:

- The parameter of interest is the lack of fit of the equation.

- Thus the test statistic,

$$F_0 = \frac{MS_{Lof}}{MS_{Res}}$$

- Tests the hypotheses,

$$H_0: There \ is \ no \ lack \ of \ linear \ fit$$
$$H_1: There \ is \ a \ lack \ of \ linear \ fit$$

- The selected confidence level is 95% ($\alpha = 0.05$).

- Reject H_0 if $F > F_{critical}$ where $F_{0.05,3,5} = 5.41$

- $MS_{Lof} = 33.96, MS_{Res} = 25.54$

$$F_0 = \frac{MS_{Lof}}{MS_{Res}} = \frac{33.96}{25.54} = 2.63$$

- The p-value is 0.1621.

- Since $F = 2.63$ and $2.63 < 5.41$, we cannot reject the null hypothesis and conclude: The "Lack of Fit F-value" of 2.63 implies the Lack of Fit is not significant relative to the pure error. There is a 16.21% chance that a "Lack of Fit F-value" this large could occur due to noise. Non-significant lack of fit is good. We want the model to fit.

Table 12: ANOVA for reduced first-order model

Source	Sum of Squares	df	Mean Square	F-Value	p-value Prob > F	Comment
Model	6851.66	4	1712.92	67.07	0.0147	significant
A-a_p	6329.81	1	6329.81	247.84	< 0.0001	
B-f_z	94.60	1	94.60	3.70	0.1123	
C-v_c	6.61	1	6.61	0.26	0.6327	
BC	420.65	1	420.65	16.47	0.0097	
Curvature	5636.49	1	5636.49	220.70	< 0.0001	significant
Residual	127.70	5	25.54			
Lack of Fit	101.87	3	33.96	2.63	0.1621	not significant
Pure Error	25.83	2	12.91			
Total	12615.85	10				

The R-Squared value for the ANOVA can be calculated as:

$$R^2 = \frac{SS_{Model} + SS_{Curve}}{SS_{Total}}$$ [Eq. 5.24]

$$= \frac{6851.66 + 5636.49}{12615.85}$$

$$= 0.9817$$

The adjusted R-Squared value for the ANOVA is:

$$Adj\ R^2 = 1 - \frac{(1 - R^2)(N - 1)}{N - p - 1}$$ [Eq. 5.25]

$$= 1 - \frac{(1 - 0.9817)(11 - 1)}{11 - 3 - 1}$$

$$= 0.9671$$

Where R^2 is from equation 5.25, N is the sample size and p is the number of estimators or variables. The remainder of the results from the ANOVA are tabulated in Table 13.

Table 13: First-order model ANOVA supplementary table 1

Std. Dev.	5.05	R-Squared	0.9817
Mean	40.90	Adj R-Squared	0.9671
C.V. %	12.35	Pred R-Squared	0.9380
PRESS	782.51	Adeq Precision	24.2619

Standard deviation is a measure of the dispersion around the average or mean value of 40.90 as shown in Table 13. High standard deviation is therefore undesirable. The standard deviation for the first-order model is 5.05.

The coefficient of variation (CV) is a ratio of the standard deviation to the mean. Lower CV ratios are desirable for modeling purposes. In this case CV is expressed as a percentage. The CV of the first-order model 12.35%.

Prediction error sum of squares (PRESS) is often used to evaluate and compare competing models [76]. PRESS is a measure of how well the model predicts new data or data that was not used to fit the model. Models with small PRESS values are preferred [76]. The PRESS value of 782.51 for the first-order model is reasonably low for modeling purposes.

The R-squared, Adjusted R-squared, Predicted R-squared are shown in Table 13. The problem with using R^2 alone as an indicator or test statistic is that it increases with the number of factors that are added to the model, even if they are insignificant. Adjusted R-squared decreases when non-significant terms are added to a model [75] [76]. Therefore it is good practice to evaluate the agreement between the R-squared and adjusted R-squared values. In this case, the adjusted R-squared of 0.9671 is in fair agreement with the R-squared of 0.9817.

 "Adeq precision" measures the model signal to noise ratio. A ratio greater than four is desirable. The current ratio of 24.262 indicates an adequate signal. This model can be used to navigate the design space.

Table 14: First-order model ANOVA supplementary table 2

Factor	Coefficient Estimate	df	Standard Error	95% CI Low	95% CI High	VIF
Intercept	54.77	1	1.79	50.17	59.36	
A-a_p	28.13	1	1.79	23.54	32.72	1
B-f_z	3.44	1	1.79	-1.15	8.03	1
C-v_c	0.91	1	1.79	-3.68	5.50	1
BC	7.25	1	1.79	2.66	11.84	1
Centre Point	-50.83	1	3.42	-59.62	-42.03	1

The coefficient estimates for the reduced model is assigned to the terms in Table 14. Each term has 1 degree of freedom. The standard error and confidence intervals are also given at a 95% confidence level. The upper and lower coefficients have ranges containing 0 for the terms B and C. This confirms these terms are not statistically significant in the model due to their near-zero effect. As previously mentioned: These terms are included to satisfy the hierarchical requirement of the model equation containing the term BC. The final equation (at 95% confidence level) for the linear model in terms of the coded factors can therefore be written as:

$$F_x = 54.77 + 28.13a_p + 3.44f_z - 0.91v_c + 7.25f_zv_c$$ [Eq. 5.26]

Coded equations are determined first, and the actual equations are derived from there. The equations appear different, even to the point of having different signs on the coefficients. To obtain the actual equation, each term in the coded equation is replaced with its coding formula:

$$X_{Coded} = \frac{X_{Actual} - \bar{X}}{(X_{High} - X_{Low})/2}$$

[Eq. 5.27]

Substitution of the formula into each linear term provides a new linear coefficient and a correction to the intercept. In addition, substitution of the formula into each interaction term results in a new interaction coefficient, a correction to each main effect in the interaction and a correction to the intercept. These corrections from the interactions can be large and opposite in sign from the linear terms and can change the sign on the linear terms. The linear model in terms of actual factors can therefore be written as:

$$F_x = 53.05 + 28.13a_p - 436.44f_z - 0.62v_c + 6.55f_zv_c$$

[Eq. 5.28]

Since the ANOVA for the reduced first order model proves that the model is significant, there is significant curvature and the lack of fit is good, the null hypothesis from section 4.3.2 is rejected. Hence it can be concluded that a first-order model represents a response surface different than the optimum of tangential cutting forces at a 95% confidence level.

Integration of the first-order equation with experimental values for a_p, f_z and V_c reveals a departure from experimental results for lower tangential cutting forces as shown in Figure 61.
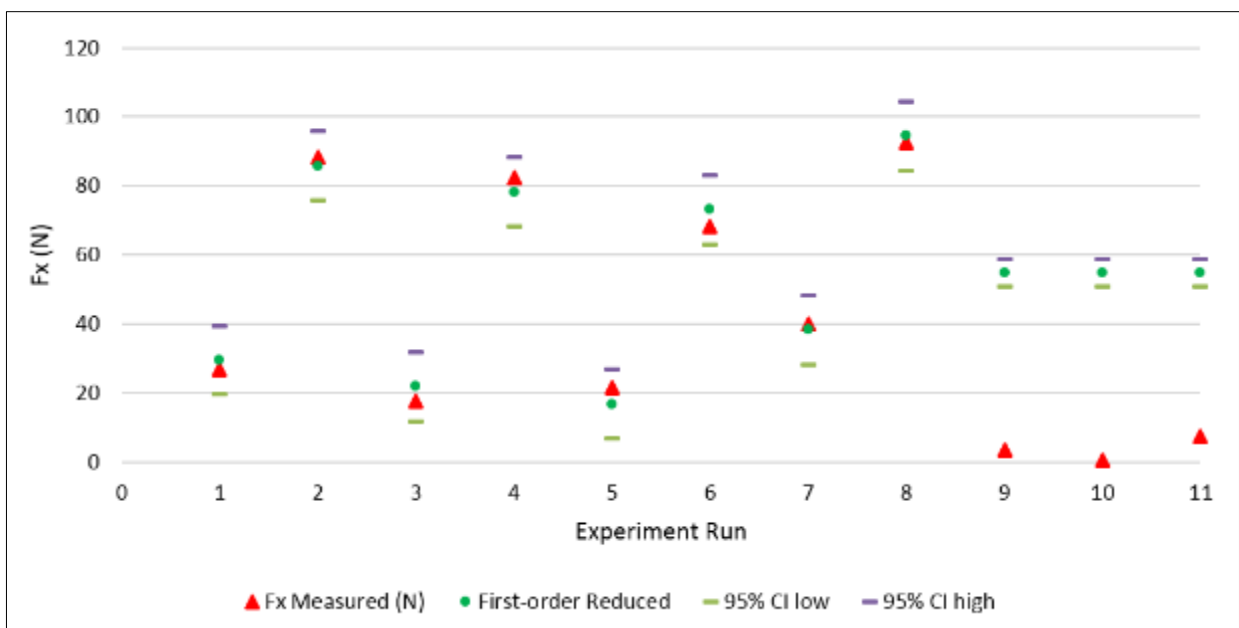
Figure 61: First-order model vs. experimental data

The first order model from equation 5.28 is able to predict the tangential cutting forces well along the higher tangential cutting force values, but prediction is unsatisfactorily along the lower cutting force data points. Cutting forces for experiment run 9, 10 and 11 are not predicted accurately despite the model's non-significant lack of fit and large R-squared value. This variation at lower cutting forces is due to the curvature that was found during the ANOVA. The first-order model does not represent the curvature adequately. Therefore it is worth testing if a second-order or quadratic model may provide an improvement upon the first-order model.

5.5.7 Fitting of a Quadratic Model

A quadratic model represents curvature more adequately due to the addition of second order terms to the equation. A second order equation typically assumes the following form [75] [76]:

$$y = \beta_0 + \beta_1 x_1 + \beta_2 x_2 + \beta_{12} x_1 x_2 + \beta_{11} x_{11}^2 + \beta_{22} x_2^2 + \varepsilon$$

The construction of the initial ANOVA for the second order model follows the same method as the first order model, with the exception of the squared term A^2, which represents the curvature. Terms B^2 and C^2 are omitted here, because they are non-significant terms. The model sum of squares therefore now includes the curvature sum of squares, which becomes A^2 and lack of fit is re-calculated:

$$SS_A = \frac{(225.03)^2}{8(1)} = 6329.81$$

$$SS_B = \frac{(27.51)^2}{8(1)} = 94.60$$

$$SS_C = \frac{(7.27)^2}{8(1)} = 6.61$$

$$SS_{AB} = \frac{(9.17)^2}{8(1)} = 10.51$$

$$SS_{AC} = \frac{(-26.91)^2}{8(1)} = 90.52$$

$$SS_{BC} = \frac{(58.01)^2}{8(1)} = 420.65$$

$$SS_{Curve} => SS_{A^2} = 5636.49$$

$$SS_{Model} = SS_A + SS_B + SS_C + SS_{AB} + SS_{BC} + SS_{AC} + SS_{A^2}$$

$$= 6329.81 + 94.60 + 6.61 + 10.51 + 90.52 + 420.65 + 5636.49$$

$$= 12589.18$$

From equation 5.10, the total sum of squares is 12615.85 and therefore from equation 5.11:

$$SS_{Total} = SS_{Model} + SS_{Error} + SS_{LoF}$$

$$12615.85 = 12589.18 + 25.83 + SS_{LoF}$$

$$SS_{LoF} = 0.84$$

And the residual sum of squares is the sum of SS_{LoF} and SS_{Error}:

$$SS_{Res} = SS_{LoF} + SS_{Error}$$
$$= 0.84 + 25.83$$
$$= 26.67$$

The MSE's are:

$$MS_A = \frac{6329.81}{1} = 6329.81$$

$$MS_B = \frac{94.60}{1} = 94.60$$

$$MS_C = \frac{6.61}{1} = 6.61$$

$$MS_{AB} = \frac{10.51}{1} = 10.51$$

$$MS_{AC} = \frac{90.52}{1} = 90.52$$

$$MS_{BC} = \frac{420.65}{1} = 420.65$$

$$MS_{A^2} = \frac{5636.49}{1} = 5636.49$$

$$MS_{LoF} = \frac{0.84}{1} = 0.84$$

$$MS_{Error} = \frac{25.83}{2} = 12.91$$

$$MS_{Res} = \frac{26.67}{3} = 8.89$$

$$MS_{Model} = \frac{12589.18}{7} = 1798.45$$

The F-Values and p-values for the second-order ANOVA are now calculated. The hypothesis to determine the significance of the model is:

- The parameter of interest is the model terms.
- Thus the test statistic,

CHAPTER : EXPERIMENTAL RESULTS AND STATISTICAL MODELING

$$F_0 = \frac{MS_{Model}}{MS_{Error}}$$

- Tests the hypotheses,

$$H_0: \beta_1 = \beta_2 = \beta_3 = \beta_{12} = \beta_{13} = \beta_{23} = \beta_{123} = 0$$
$$H_1: at\ least\ one\ \beta \neq 0$$

- The selected confidence level is 95% ($\alpha = 0.05$).

- Reject H_0 if $F > F_{critical}$ where $F_{0.05,7,2} = 19.35$

- $MS_{Model} = 1798.45, MS_{Error} = 19.35$

$$F_0 = \frac{MS_{Model}}{MS_{Error}} = \frac{1798.45}{19.35} = 92.94$$

- The p-value is 0.0106.

- Since $F = 92.94$ and $92.94 > 8.89$, reject null hypothesis and conclude that the model is significant. The p-value of 0.01059 indicates that there is only a 1.06% chance that a Model F-Value this large could occur due to noise.

The hypothesis for the test of lack of fit is:

- The parameter of interest is the lack of fit of the equation.

- Thus the test statistic,

$$F_0 = \frac{MS_{Lof}}{MS_{Error}}$$

- Tests the hypotheses,

$$H_0: There\ is\ no\ lack\ of\ fit$$
$$H_1: There\ is\ a\ lack\ of\ fit$$

- The selected confidence level is 95% ($\alpha = 0.05$).

- Reject H_0 if $F > F_{critical}$ where $F_{0.05,1,2} = 18.51$

- $MS_{Lof} = 0.84, MS_{Error} = 12.91$

$$F_0 = \frac{MS_{Lof}}{MS_{Error}} = \frac{0.84}{12.91} = 0.065$$

- The p-value is 0.8227.

- Since $F = 12.91$ and $12.91 < 18.51$, we cannot reject the null hypothesis and conclude: The "Lack of Fit F-value" of 0.065 implies the Lack of Fit is not significant relative to the pure error. There is a 82.27% chance that a "Lack of Fit F-value" this large could occur due to noise. Non-significant lack of fit is good. We want the model to fit.

Table 15: ANOVA for second-order model

Source	Sum of Squares	df	Mean Square	F-Value	p-value Prob > F	Comment

Model	12589.18	7	1798.45	92.94	0.0106	significant
A-a_p	6329.81	1	6329.81	712.08	0.0001	
B-f_z	94.60	1	94.60	10.64	0.0471	
C-v_c	6.61	1	6.61	0.74	0.4520	
AB	10.51	1	10.51	1.18	0.3564	
AC	90.52	1	90.52	10.18	0.0497	
BC	420.65	1	420.65	47.32	0.0063	
A^2	5636.49	1	5636.49	634.08	0.0001	
Residual	26.67	3	8.89			
Lack of Fit	0.84	1	0.84	0.06	0.8227	not significant
Pure Error	25.83	2	12.91			
Total	12615.85	10				

The second-order model standard deviation of 2.98 is less than the first-order model standard deviation of 5.05 as shown in Table 16.

Table 16: Second-order model ANOVA supplementary table 1

Std. Dev.	2.98	R-Squared	0.9979
Mean	40.90	Adj R-Squared	0.9930
C.V. %	7.29	Pred R-Squared	0.9911
PRESS	111.78	Adeq Precision	34.7427

The CV of the second-order model (7.29%) is lower than the CV of the first-order model (12.35%). The PRESS value of 111.78 for the second-order model is considerably less than the PRESS value of 782.51 for the first-order model. The adjusted R-squared of 0.9930 is in better, reasonable agreement with the R-squared of 0.9979 when compared to the first-order model. The signal to noise ratio of 34.74 shows improvement over the first order model signal to noise ratio of 24.2619.

Table 17: Second-order model ANOVA supplementary table 2

Factor	Coefficient Estimate	df	Standard Error	95% CI Low	95% CI High	VIF
Intercept	3.94	1	1.72	-1.54	9.42	
A-a_p	28.13	1	1.05	24.77	31.48	1
B-f_z	3.44	1	1.05	0.08	6.79	1
C-v_c	0.91	1	1.05	-2.45	4.26	1
AB	1.15	1	1.05	-2.21	4.50	1
AC	-3.36	1	1.05	-6.72	-0.01	1
BC	7.25	1	1.05	3.90	10.61	1
A^2	50.83	1	2.02	44.40	57.25	1

Coefficients are assigned to the second-order model terms in Table 17. The final equation in terms of the coded factors for the model is:

$$F_x = 3.94 + 28.13a_p + 3.44f_z - 0.91v_c + 1.15a_pf_z - 3.36a_pV_c + 7.25f_zV_c + 50.83a_p^2 \qquad \text{[Eq. 5.29]}$$

Substituting the formula from equation 5.27 into each quadratic term will result in a new quadratic coefficient and a correction to the intercept:

$$F_x = 102.45 - 114.93a_p - 470.83f_z - 0.39V_c + 22.93a_pf_z - 0.15a_pV_c + 6.55f_zV_c + 50.83a_p^2 \quad \text{[Eq. 5.30]}$$

Integration of the second-order equation with experimental values for a_p, f_z and v_c shows improved prediction ability for high and low values of measured tangential cutting force as shown in Figure 62.
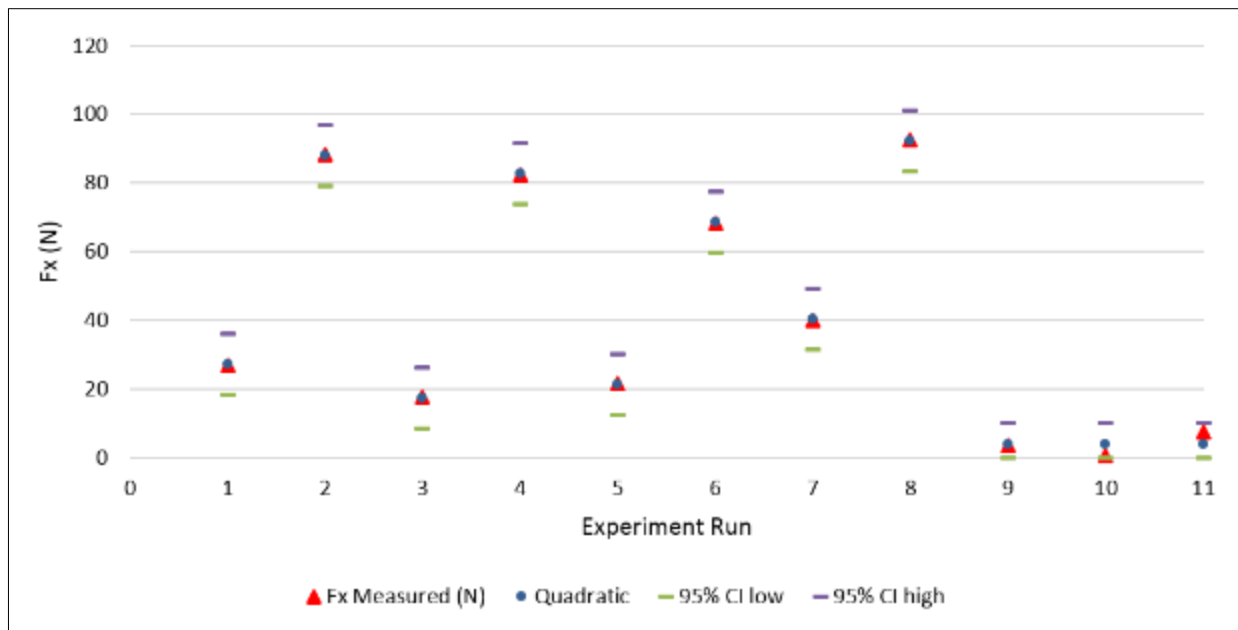
Figure 62: Second-order model vs. experimental data

Cutting forces for experiment run 9, 10 and 11 are predicted more accurately due to the inclusion of the curvature in the second-order model. The second-order predicted force values also show better agreement with experimental values, when compared to the predicted values of the first-order model. This confirms the improvements discussed with Table 16. The second-order model provides satisfactory results at a 95% confidence level. Diagnostic plots can be constructed for further evaluation.

5.5.8   Diagnostic Plots

Diagnostic plots provide a valuable tool for visual assessment of the ANOVA findings. A modest deviation from normality can be observed in the normal plot of residuals as shown in Figure 63, but not enough to be of concern. The residuals vs. predicted plot also reveals nothing unusual, nor does the plot for externalized student residuals. Predicted vs. actual plot shows good performance, including the centre points.
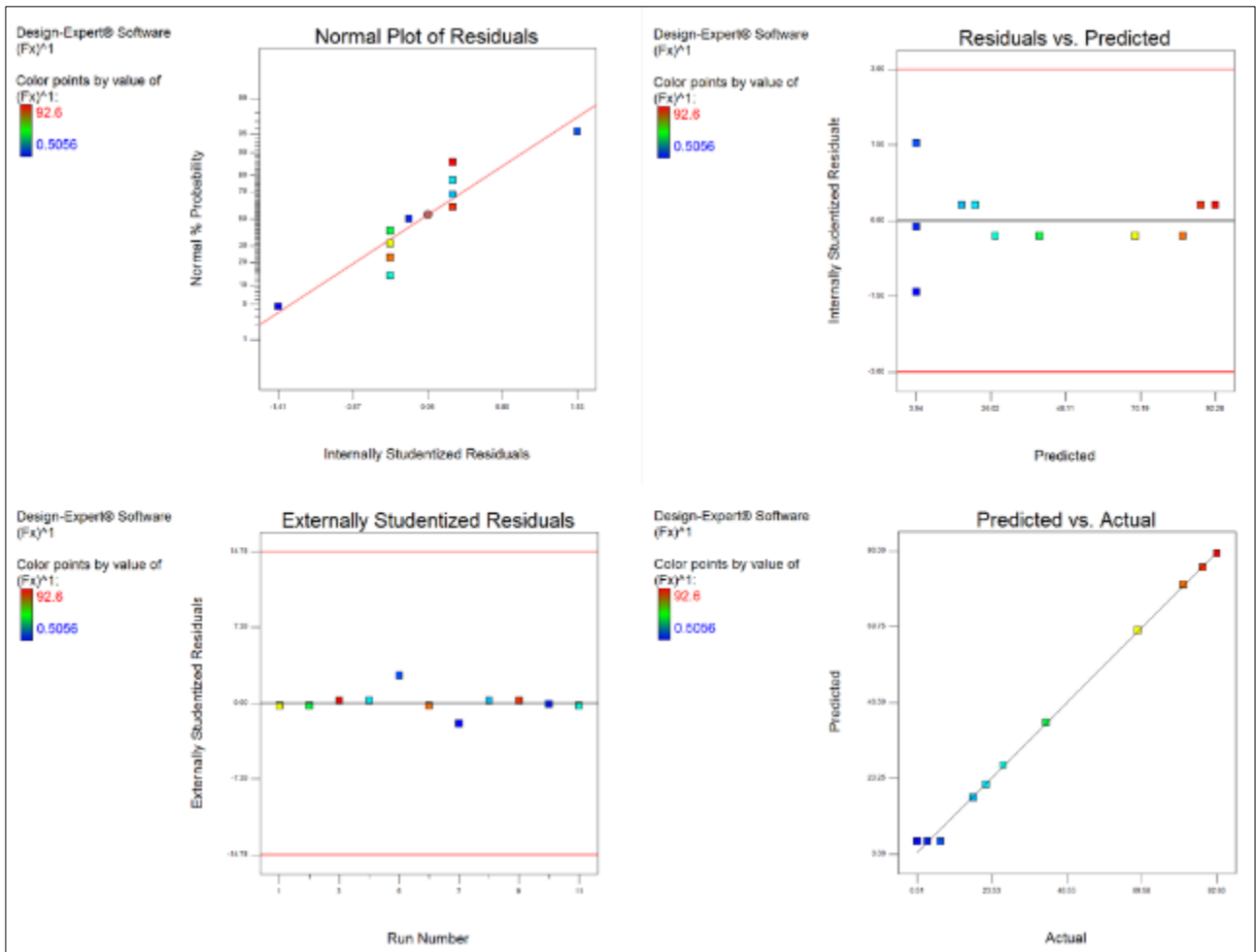
Figure 63: Residual and predictive plots

The Box-Cox plot for the power transforms that were performed on the primary data before the ANOVA was performed, reveals no further requirements as shown in Figure 64. The ANOVA and diagnostic plots provide satisfactory results of a significant second-order model that fits the design space.

Despite the suboptimal nature of the model, results still provide the opportunity to assess the model within the selected response surface. The model is not fitted to the optimal response surface, therefore significant predictions about any values outside of the experimental area cannot be made at the 95% confidence level.
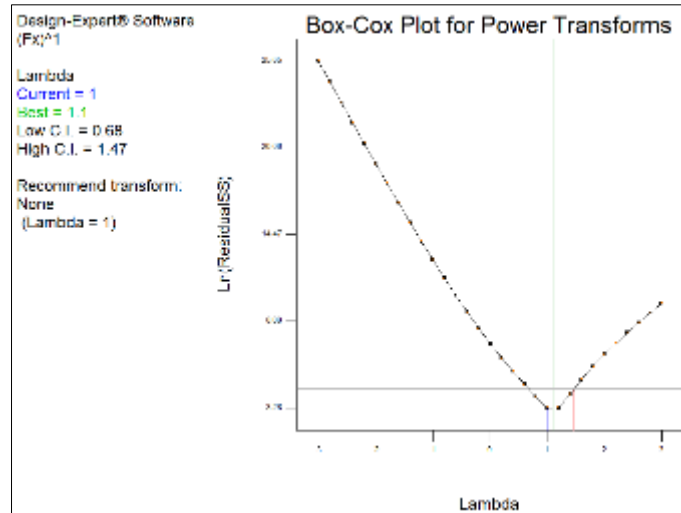
Figure 64: Box-Cox plot for power transforms

5.5.9   Model Graphing

Factors running in parallel lines mean no interaction, while crossing lines provide evidence for interaction. It should be added that interaction plots are often used for supplementary illustration purposes and should not be used as the only analysis technique, because the interpretation is subjective and the appearance can be misleading [75].
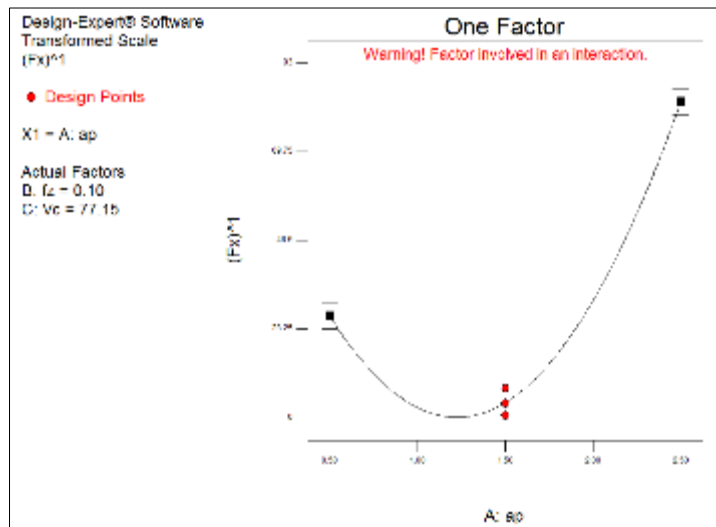
Figure 65: Effect of ADOC on tangential cutting force

The tangential cutting force reduces as ADOC is increased from 0.5 mm to approximately 1.2 mm as shown in Figure 65. From this point onward, tangential cutting force increases along with an increase in ADOC. This is the case for all feedrates and cutting speeds along the design space. Figure 66 shows that the tangential cutting force decreases as feedrate is increased, while cutting speed is at the low level. Conversely, if cutting speed is at medium and high levels, the tangential cutting force increases as feedrate is increased.

As cutting speed increases, the tangential cutting force decreases, as shown in Figure 67. This is only the case at the low level of feedrate. The tangential cutting force increases as cutting speed increases at the medium and high levels of feed per tooth.
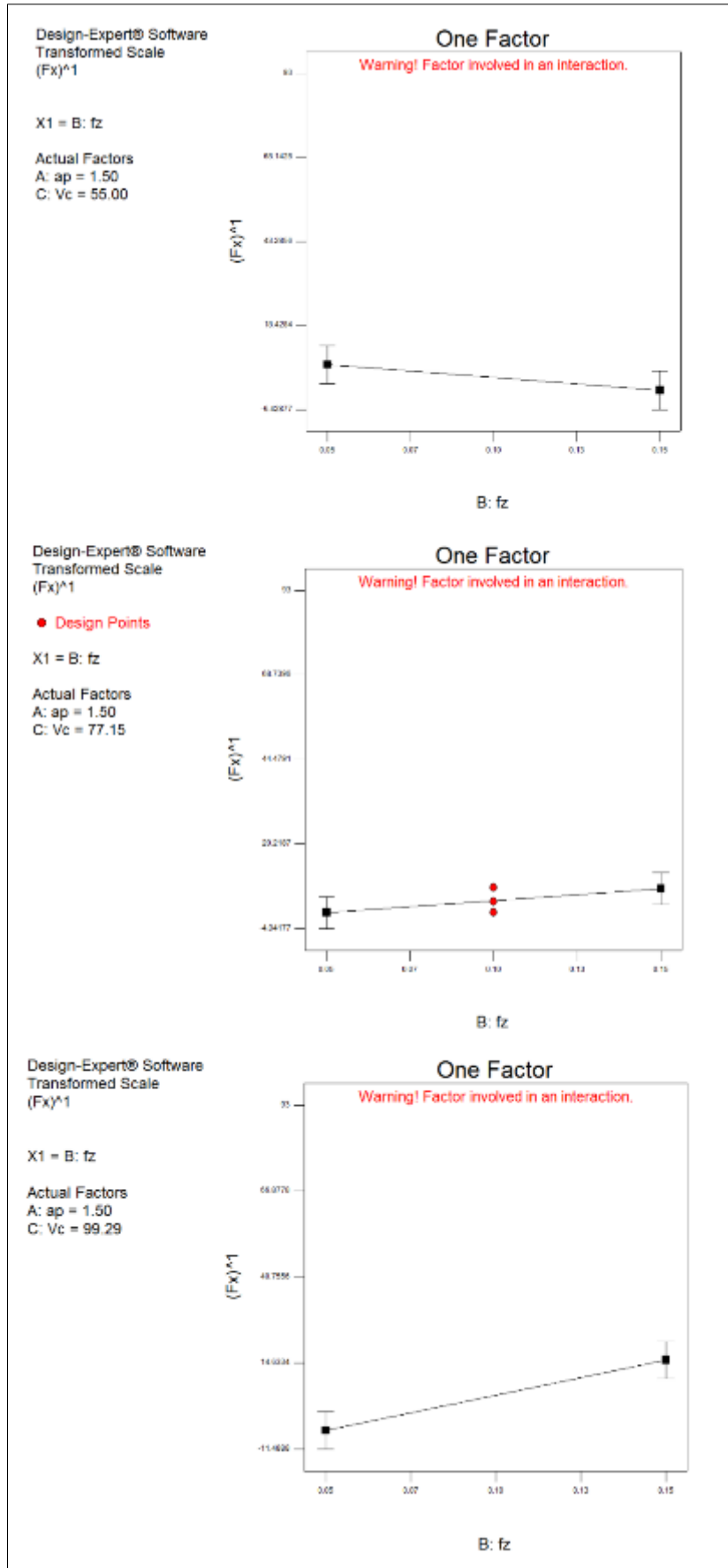
Figure 66: Effect of feed per tooth on tangential cutting force at different cutting speeds
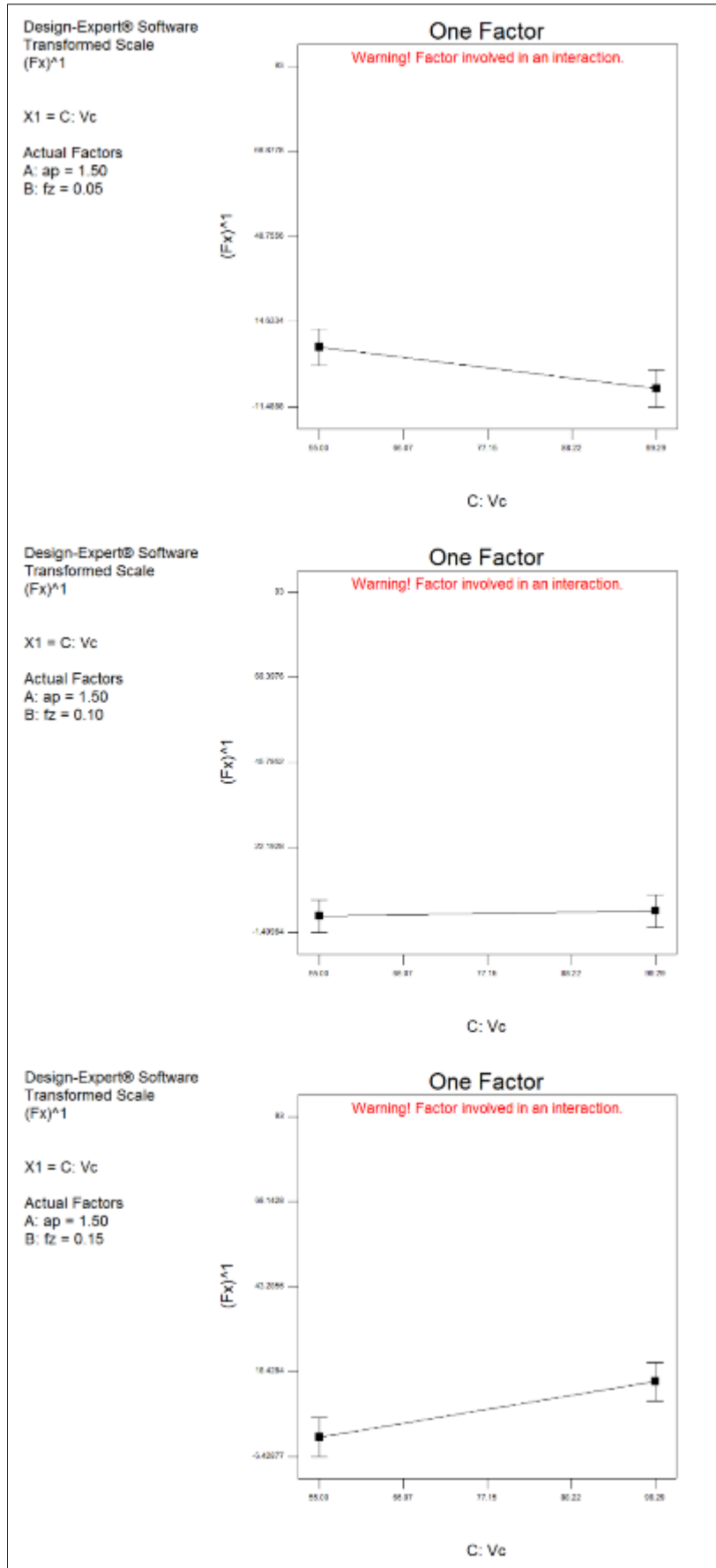
Figure 67: Effect of cutting speed on tangential cutting force at different feedrates

CHAPTER : EXPERIMENTAL RESULTS AND STATISTICAL MODELING

The interaction of feedrate and ADOC is shown in Figure 68. It is observed that with the initial decrease (at the low level) in ADOC, the tangential cutting force also decreases. This changes at approximately 1.20 mm ADOC (mid-level ADOC), where the relationship becomes: cutting force increases with an increase in ADOC. This relationship or tendency is observed at high and low feedrates.
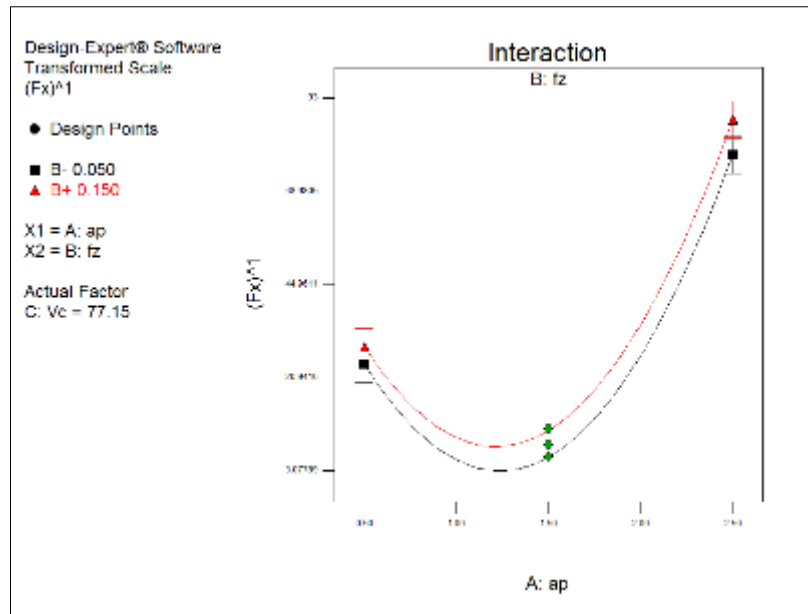
Figure 68: Effect of ADOC on tangential cutting force at different feedrates

The interaction between ADOC and cutting speed is shown in Figure 69. It is observed that with the initial decrease (at the low level) in ADOC, the tangential cutting force also decreases. This changes at approximately 1.20 mm ADOC (mid-level ADOC), where the relationship becomes: cutting force increases with an increase in ADOC. This relationship or tendency is observed at high and low cutting speeds.
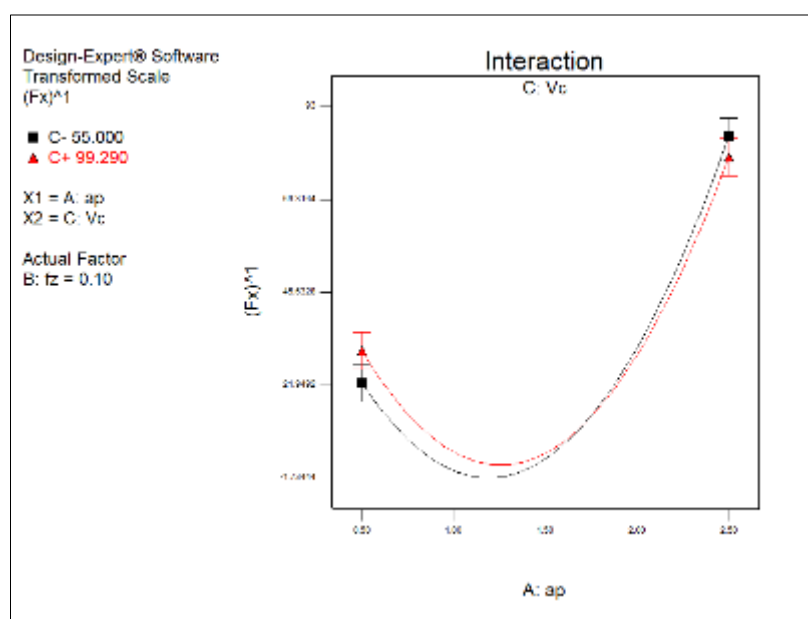
Figure 69: Effect of ADOC on tangential cutting force at different cutting speeds

The interaction of feedrate and cutting speed is shown in Figure 70. It is observed that tangential cutting force decreases with an increase of feedrate at low cutting speeds. Tangential cutting force increases as feedrate is increased at high cutting speeds.
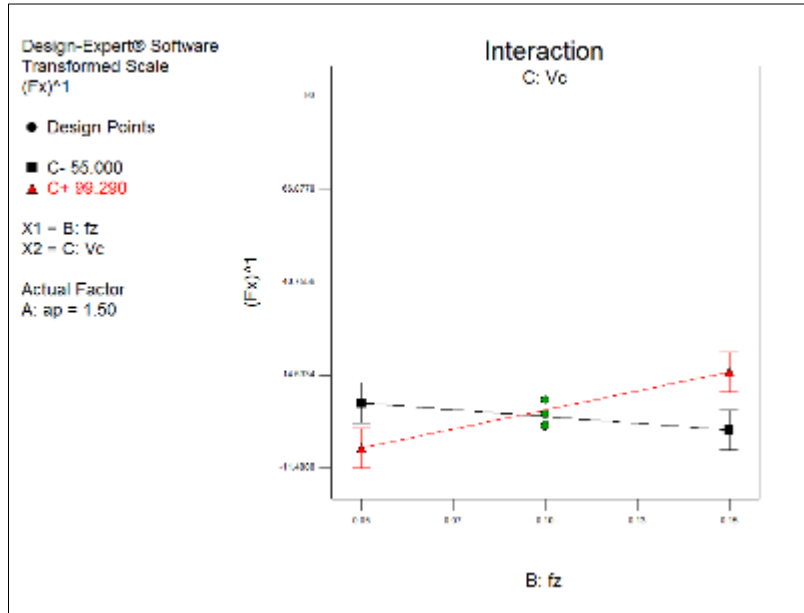
Figure 70: Effect of feedrate on tangential cutting force at different cutting speeds

The significance of the factors can also be summarized by a cube graph. ADOC is the most significant factor, followed by cutting speed and feedrate. Cutting speed and feedrate have a negative effect on tangential cutting force, while ADOC has a positive effect as shown in Figure 71.
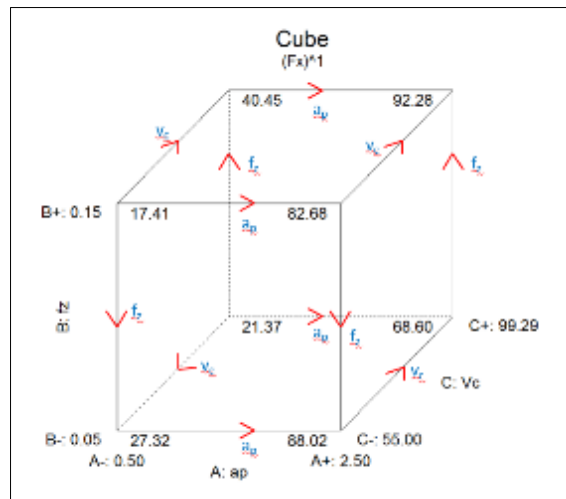
Figure 71: Cube graph

The 3-D response surface of the second-order model is shown in Figure 72, Figure 73 and Figure 74. The contour plot in Figure 72 is based on the significant interaction effect of feedrate and ADOC on the tangential cutting force. The twisting of the 3-D plane and the curved contour verifies strong interaction between these factors. The 3-D plot in Figure 72 verifies the conclusions from Figure 68 that tangential cutting force is highest in areas on the curve where the ADOC is at low and high levels, regardless of high

feedrate. Similarly, the contour plots and 3-D response surfaces in Figure 73 and Figure 74 provide additional evidence on the findings based on the interactions from Figure 69 and Figure 70 respectively.
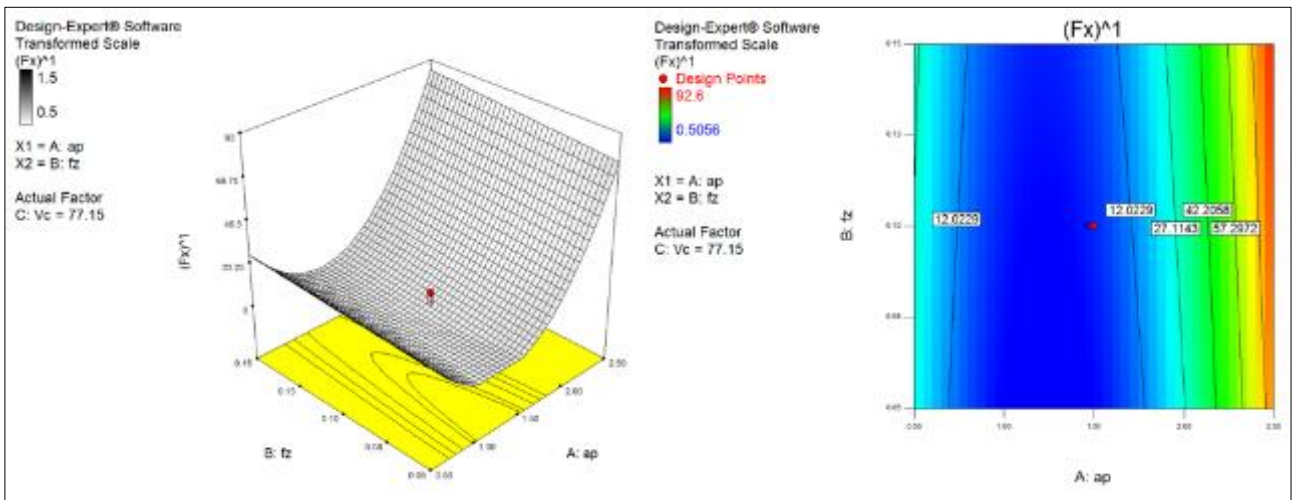
Figure 72: Response surface and contour plot for ADOC and feedrate interaction
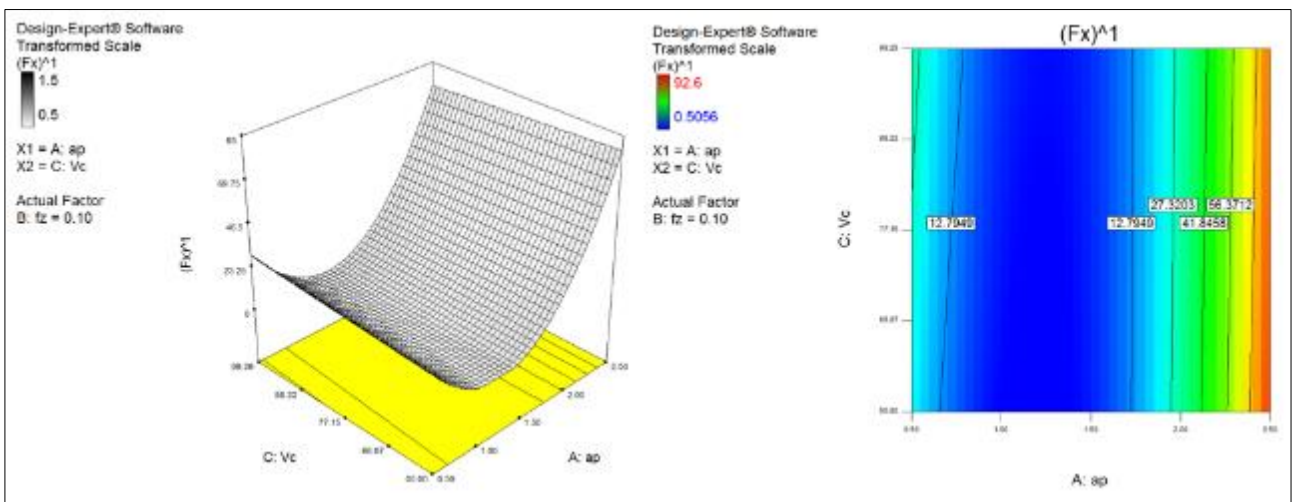
Figure 73: Response surface and contour plot for ADOC and cutting speed interaction
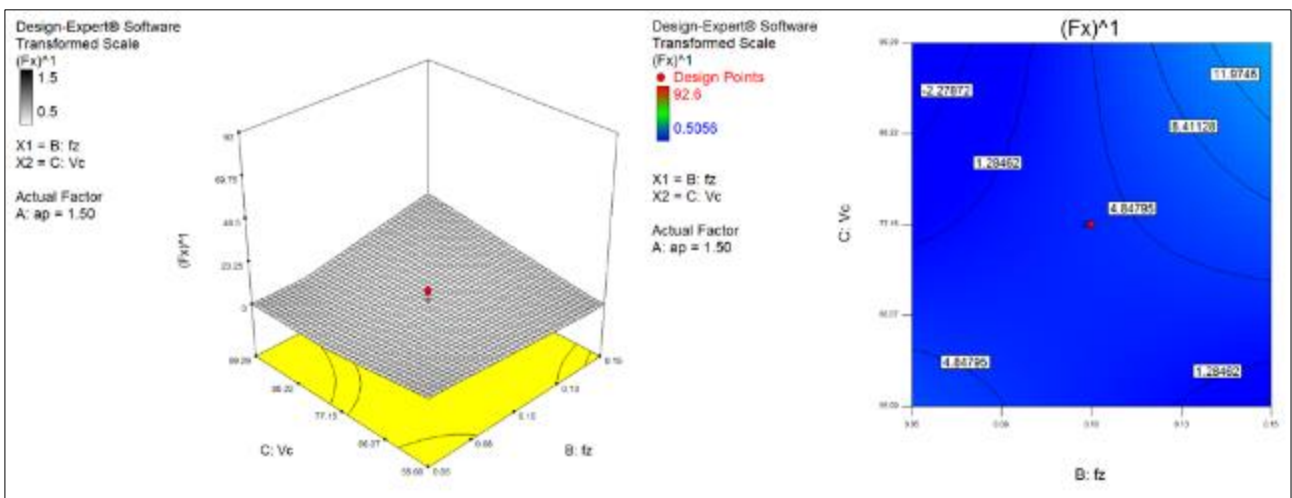
Figure 74: Response surface and contour plot for feedrate and cutting speed interaction

5.6 CONCLUSIONS AND RECOMMENDATIONS

The experimental data collected for the tangential cutting force follows a left-skewed normal distribution and had to be transformed with application of a power transformation for modeling and analysis purposes. A first-order model provided a significant fit to the data at the 95% confidence level, but was unable to predict tangential cutting forces at low levels. The alternative research hypothesis was statistically significant, while the null hypothesis was rejected. The presence of significant curvature means that: "A first-order model represents a response surface different than the optimum of tangential cutting forces". Hence a second-order model was fitted to the data. The second-order model significantly represents a response surface with curvature that is close to the optimum response surface. The second-order equation can be used to predict cutting forces within the design space at a 95% confidence level.

The model can be improved to represent the optimal response surface for this process through augmentation towards a central composite design. Six axial or star points can be added to the existing experimental data, which means that six additional experiments should be conducted. These six additional experiments are to be performed under the exact conditions as the first set of experiments, i.e. the same work material, milling machine setup, cutting tools and cutting strategy.

The examination of machinability factors such as surface finish, tool wear rate and chip control revealed no abnormalities. The surface finish achieved during experimentation is comparable to the surface finish requirements for finishing in some cases. Therefore the Kennametal KSRM63A04RC20BB cutter with RCGX2006M0SGF inserts is recommended for roughing as successive finishing operations would be kept to a minimum. Tool wear followed a uniform pattern for the majority of cutting experiments and is evident of cutting under normal conditions. The analysis of cutting chips verified findings from literature and provided evidence about the temperature and chip evacuation at the cutting interface.

CHAPTER 6

PRACTICAL WORK WITH INDUSTRY PARTNER

6.1 INTRODUCTION

The funding contract for this study requires technology transfer to an industrial partner. The goal of this part of the project is therefore to transfer academic knowledge in a practical way to improve the productivity of the industry partner's current processes. Hence, the project is focused on a larger volume product, where improvements, if any, would make the largest impact on overall productivity.

The chosen component for the project is a lug machined from stainless steel (Figure 75). Daliff Precision Engineering manufactures an annual volume of approximately 100 lugs for Airbus. Daliff Engineering also has contracts with companies such as Denel and Boeing, though annual volumes for these clients are lower. The project had to coincide with a scheduled production window at the workshop.

The component for comparison (Figure 75) is machined from Aubert & Duval's X15U5W 15-5 PH Stainless Steel. The Stainless Steel was hardened for four hours at 550°C. Its Brinell hardness factor is 357 HBW and tensile strength is 1126 N/mm^2. These material characteristics are similar to Ti-6Al-4V (336 HBW, 950 N/mm^2), with the exception of the difference in thermal conductivity. X15U5W 15-5 PH Stainless Steel has a thermal conductivity of 16 W.m/m^2. °C, compared to the thermal conductivity of Ti-6Al-4V (6.7 W.m/m^2.°C) [39] [86]. The forces and power required for machining the two materials is expected to be similar, with accelerated tool wear for Ti-6Al-4V.
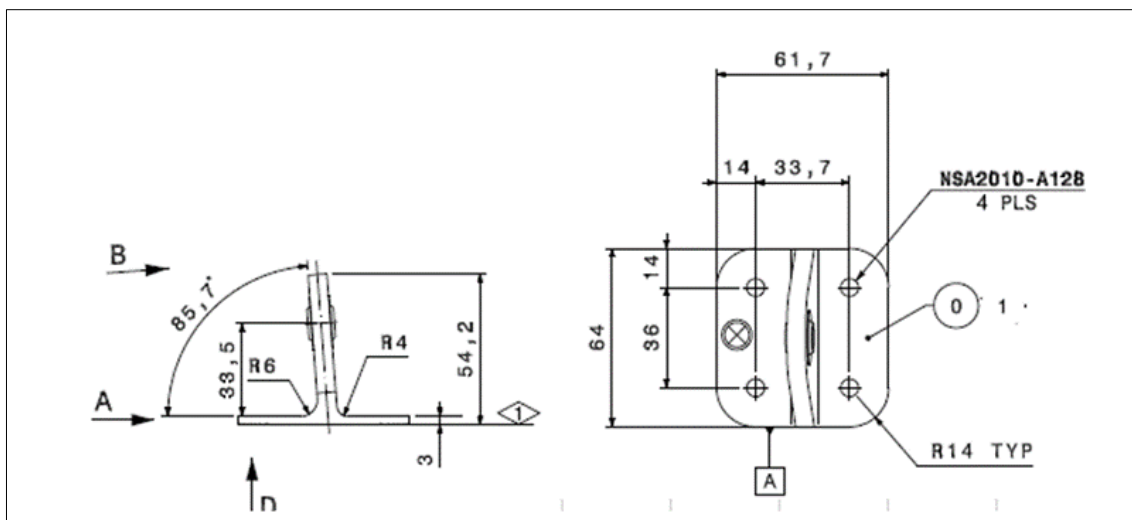
Figure 75: Airbus lug component, 15-5 PH Stainless Steel (dimensions in mm)

The lug is currently fabricated on a Deckel Maho DMU 60, 5-axis milling machine. The Deckel Maho has an initial investment cost of R4.5M. The current process times for machining the component on the Deckel Maho are summarised in Figure 76. The roughing process occupies 73% of the current total machining time.

CHAPTER : PRACTICAL WORK WITH INDUSTRY PARTNER

Therefore this project is focused on improving the roughing process and subsequently reducing the required machining time of the Airbus lug.

Machining Process	Process Time (hh:mm)
Roughing	01:53
Surface finishing	00:03
Drill (Bottom)	00:04
Milling (Angle)	00:07
Milling (Curve)	00:03
Surface finishing	00:11
Drill (Bearing)	00:04
Measure, re-drill	00:02
De-burring	00:08
Total Time	02:35
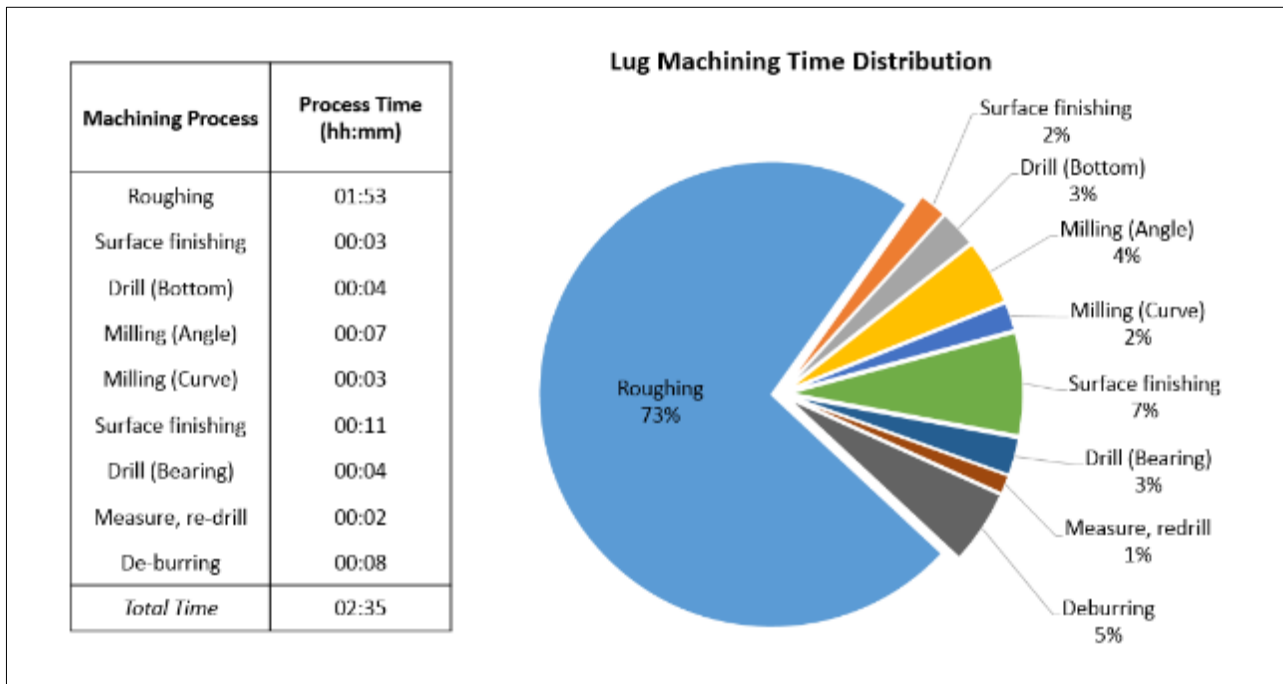
Figure 76: Current machining processes and times for Airbus lug

6.2 MACHINE TOOL, INSERTS AND WORKPIECE MOUNTING

In addition to the Deckel Maho, Daliff Precision Engineering has a Leadwell V-50L (3-axis) milling machine in the workshop. The Leadwell milling machine's cost is considerably less than the Deckel Maho at R1.6M, and was therefore utilised for the purpose of comparative testing during this project. The Deckel Maho's 5-axes are not essential for the machining of the Airbus lug if recent developments are utilised in cutting tools and hence process design. Migration of the roughing process to the Leadwell alone, already provides a 2.8 times saving due to the difference in machine cost per hour.

Figure 77: Kennametal Beyond Blast KSRM cutter ad RCGX round inserts

Roughing tools for the project are the Kennametal (Figure 77) and ISCAR (Figure 78) cutters with their respective inserts. The ISCAR cutter has a positive-neutral geometry. Each cutter that was tested has four

inserts. The Kennametal cutter has through spindle and split tool cooling. The Leadwell V-50L is able to produce three bar pressure for nozzle and through spindle cooling.
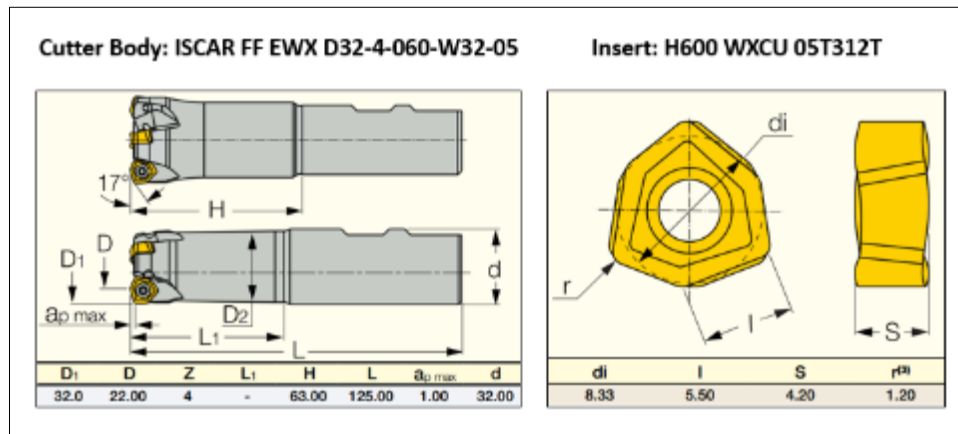
Figure 78: ISCAR EWX cutter and H600 hexagonal inserts

The 15-5 PH stainless steel billets for the Airbus lugs were clamped to a pedestal that was clamped to the machine bed (Figure 79). The pedestal and clamp is manufactured from mild steel. The billet is attached to the pedestal by four screws in the bottom of the flange assembly. The flange is held together with two M12 screws (one in each opposing corner).The four holes in the bottom of the billet are pre-drilled. The pedestal is then attached to the machine bed with two M10 screws (also one in each opposing corner).
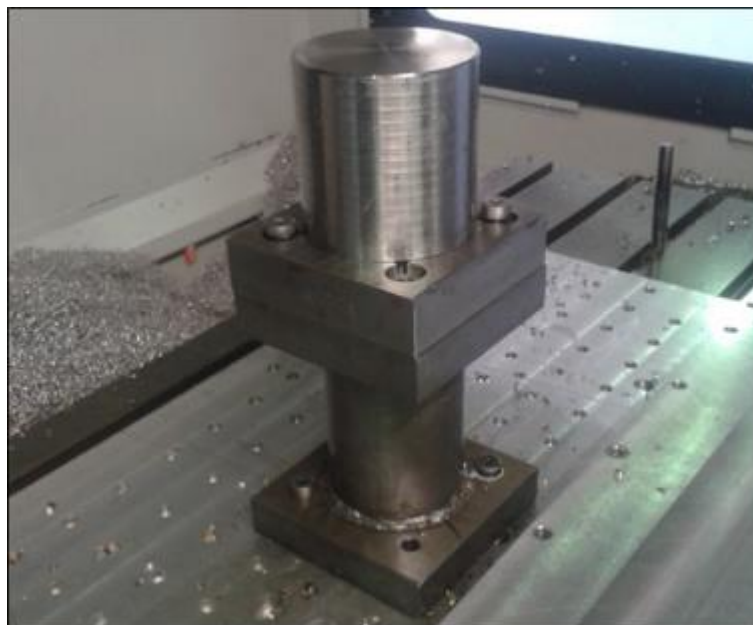
Figure 79: Airbus "lug" clamping method on Leadwell V-50L

The cutting parameters such as feed per tooth (f_z), ADOC (a_p) and revolutions per minute (n) required process improvement for operation with the Leadwell machine to ensure more productive cutting conditions.

6.3 PRODUCTIVITY CALCULATIONS

Productivity formulae are often provided by the tool manufacturer in the technical section of the cutting tool manuals for practical application in the workshop. In addition it was found that online productivity calculators on the tool manufacturer websites employ the same formulae. These formulae are required to calculate tool-specific productivity factors such as MRR, table feed, cutting speed, and cutting power for example.

6.3.1   Tool Wear Factor

The tool wear factor is a constant that corresponds to different tool wear rates with varying cutting forces. The tool wear factor (C_w) is needed for further cutting force related calculations. The tool wear factor for a determined cutting operation can be referenced from Table 18, as prepared by Oberg [87]:

Table 18: Tool wear factors [87]

Milling type	a_p (mm)	f_z (mm)	C_w
Light	0.5 to 2.5	0.08 to 0.15	1.1
Medium	2.5 to 5	0.15 to 0.25	1.2
Heavy Duty	5 to 10	0.25 to 1.0	1.3

6.3.2   Effective Cutting Diameter

The cutting speed is dependent on the effective cutting diameter (D_{max}) at a specific axial depth (a_p). With the Kennametal inserts, the effective cutting diameter (D_{max}) is dependent on the ADOC. The equation for effective cutting diameter for the Kennametal cutter at a specific depth is [80]:

$$D_{max.R} = D_c + \sqrt{D_i{}^2 - (D_i - 2a_p)^2}$$

[Eq. 6.1]

Where $D_{max.R}$ is the effective cutting diameter (mm), D_c is the cutter body diameter (mm), D_i is the insert diameter (mm) and a_p is the ADOC (mm). This equation is only applicable for use with round inserts, hence the addition of "R" in the notation.

6.3.3   Radial Engagement Ratio and Machinability Factor

This ratio is the relationship of the radial depth of cut (RDOC) of the cutting tool and workpiece, based on effective cutting diameter. For example: The machinability factor (C_m) is assumed to be 1.20 for a W/D ratio of 0.67 ≤ W/D ≤ 1.0 for Ti-6Al-4V milling as shown in Table 19.

Table 19: Kennametal machinability factor table [80]

Machinability Factor (C_m)	W/D ≤ 0.67	0.67 ≤ W/D ≤ 1.0	W/D = 1.0
Carbon & Alloy Steels	1.0	1.15	1.3
Stainless Steel	2.0	2.15	2.3
Grey Cast Iron	1.0	1.15	1.3
Titanium Alloys	1.0	1.20	1.4

| Aluminium Alloys | 1.0 | 1.05 | 1.1 |

Figure 80 illustrates how the W/D engagement factor is calculated by using the ratio of the RDOC to the maximum effective diameter of the cutter.
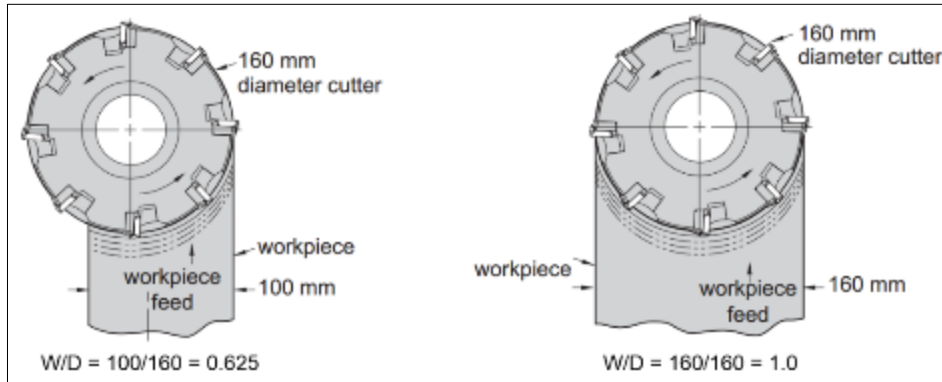
Figure 80: Top view of cutter bodies - Engagement factor of 0.625 (left) and 1.0 (right)

Radial engagement is formulated as follows:

$$\frac{W}{D} = \frac{a_e}{D_{\max}}$$

[Eq. 6.2]

6.3.4   Engagement Angle and Number of Teeth in Cut

Number of teeth in cut (Z_c) is a calculated factor for how many inserts are in the cut and is used in calculating the tangential cutting force (F_x). The amount of inserts in the cut is dependent on the following parameters: Effective cutting diameter (D_{max}), Width of cut (a_e), Engagement angle (α), Angle between cutter centre line and cutter radius to the peripheral point of exit or entry (α_1), and number of inserts in the cutter body (Z_n). For all force and power related calculations, the effective cutter diameter (D_{max}) needs to be used. The effective cutting diameter should not be confused with the cutter body diameter (D_c). There are two different scenarios for calculating the number of inserts in the cut. The first formula assumes that:

$$\frac{D_{max}}{2} < a_e < D_{max}$$

[Eq. 6.3]

The cutter is engaged with the workpiece by more than half of the effective cutting diameter as illustrated in Figure 81.
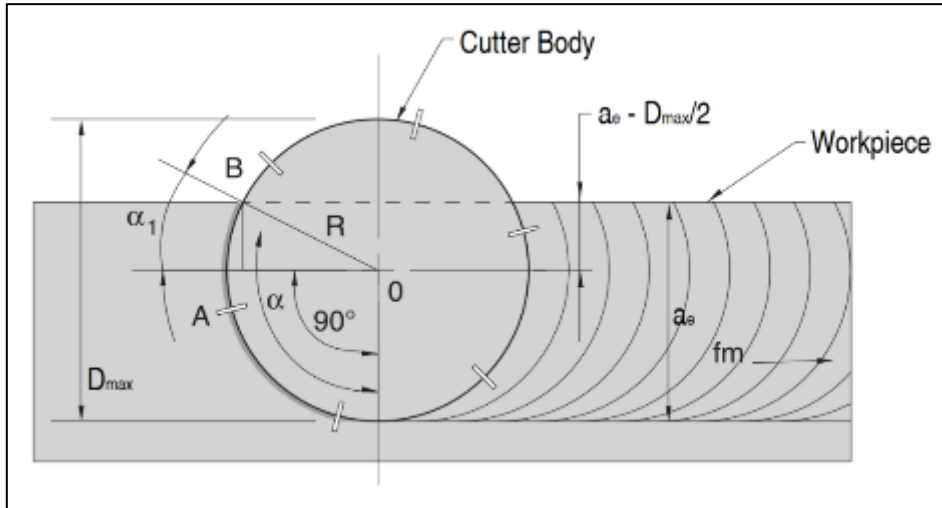
Figure 81: Engagement Angle and number of inserts in cut for $D_{max}/2 < a_e < D_{max}$ [82]

Z_c for $D_{max}/2 < a_e < D_{max}$ is formulated as:

$$Z_c = \frac{z\left[90° + sin^{-1}\left(\frac{2a_e - D_{max}}{D_{max}}\right)\right]}{360°}$$

[Eq. 6.4]

Where:

$$Z_c = \frac{z \times \alpha°}{360°}$$

And:

$$\alpha = 90° + \alpha_1$$

Thus:

$$sin\alpha_1 = \frac{AB}{OB} = \left[\frac{a_e - \left(\frac{D_{max}}{2}\right)}{\left(\frac{D_{max}}{2}\right)}\right] = \frac{2\left[a_e - \left(\frac{D_{max}}{2}\right)\right]}{D_{max}} = \frac{2a_e - D_{max}}{D_{max}}$$

Hence:

$$\alpha_1 = sin^{-1}\frac{2a_e - D_{max}}{D_{max}}$$

The second formula assumes that the cutter is engaged with the workpiece by less than half of the effective cutting diameter as illustrated in Figure 82. The formula is given as:

$$a_e < \frac{D_{max}}{2}$$

[Eq. 6.5]
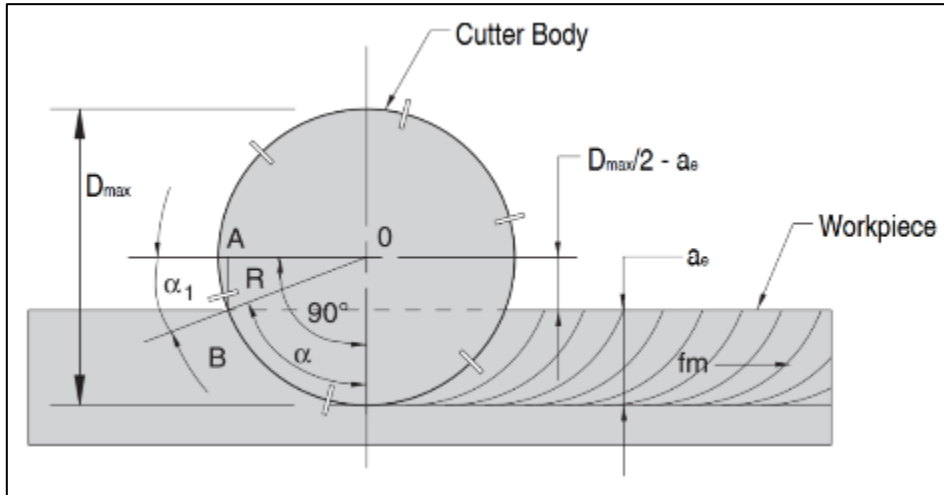
Figure 82: Engagement Angle and number of inserts in cut for a_e < D_max/2 [82]

Z_c for $a_e < D_{max}/2$ is formulated as:

$$Z_c = \frac{z\left[90° - sin^{-1}\left(\frac{D_{max} - 2a_e}{D_{max}}\right)\right]}{360°}$$

[Eq. 6.6]

Where:

$$Z_c = \frac{z \times \alpha°}{360°}$$

And:

$$\alpha = 90° - \alpha_1$$

Thus:

$$sin\alpha_1 = \frac{AB}{OB} = \left[\frac{\left(\frac{D_{max}}{2}\right) - a_e}{\left(\frac{D_{max}}{2}\right)}\right] = \frac{2\left[\left(\frac{D_{max}}{2}\right) - a_e\right]}{D_{max}} = \frac{D_{max} - 2a_e}{D_{max}}$$

Hence:

$$\alpha_1 = sin^{-1}\frac{D_{max} - 2a_e}{D_{max}}$$

6.3.5 Cutting Force Required at the Spindle

To calculate the required tangential cutting force, (f_x) the formula used is:

$$F_x = S \times A \times Z_c \times C_m \times C_w$$

[Eq. 6.7]

Where S = Ultimate strength of Ti-6Al-4V (N/mm²), A is average cross sectional area of the chip (mm²), Z_c is number of inserts in cut (Not to be confused with z), C_m is machinability factor is a constant 1.2 (factor), C_w is tool wear factor is a constant for Ti-6Al-4V milling = 1.2 [80].

6.3.6 Cutting Speed

The cutting speed equation is:

$$v_c = \frac{D_c \times \pi \times n}{1000}$$

[Eq. 6.8]

Where, v_c is the cutting speed in m/min, D_c is the cutter body diameter, π is the constant of which the first six digits are 3.14159 and n is the spindle speed (rpm). The cutting speed is also referred to as the chip velocity and is the speed at which chips are removed at the cutting interface. The cutting interface is subjected to increased friction in cases where the cutting speed is high.

6.3.7 Table Feed

Table feed is the speed at which the tool is moving in the cutting direction. It is expressed as mm/min. The table feedrate is formulated as:

$$v_f = f_z \times n \times z$$

[Eq. 6.9]

Where v_f is the table feed in mm/min, f_z is feed per tooth (mm), n is spindle speed (rpm), z is the number of inserts in cutter body. Feed per tooth is the thickness of chip material that each tooth removes with one pass as per Figure 83. The number of revolutions per minute is represented by n (rpm).
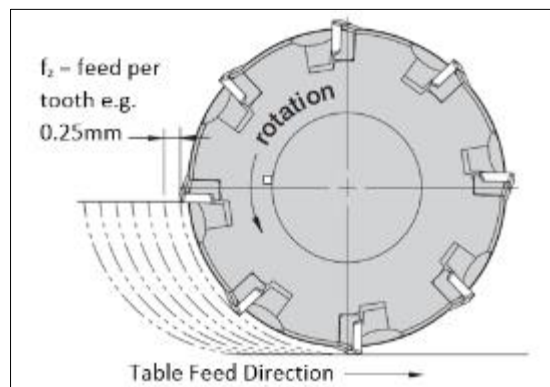
Figure 83: Top view of an example of a face milling cutter body with z = 8 and f$_z$ = 0.25

6.3.8 Average Cross Sectional Area of Chip

The average cross sectional area of the chip is a dynamic value calculated by the product of the instantaneous cutting depth and feed per tooth at any given moment during the cut.
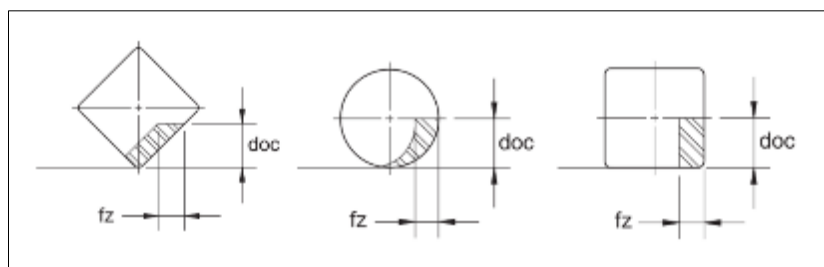
Figure 84: Average cross sectional area of chip according to insert geometry

The average cross sectional area of the chip is calculated as [82]:

$$A = a_p \times f_z$$

[Eq. 6.10]

6.3.9   Material Removal Rate

The material removal rate (MRR) is usually measured in cm³/min and resembles the volume of material that is removed by the machining process per minute. Material removal rate can be formulated as:

$$MRR = \frac{a_p \times a_e \times n \times f_z \times z_n}{1000}$$

[Eq. 6.11]

Where a_p is ADOC (mm), a_e or W is the radial width of cut, often referred to as RDOC (mm), n is the number of revolutions per minute (rpm), f_z is feed per tooth (mm) and z_n is the number of inserts in the cutter body.

6.4 ISCAR TOOL CONSIDERATIONS

6.4.1   Tool Wear Factor Selection

The ISCAR insert is limited to an ADOC of 0.85 mm. The feed per tooth of the tool is limited to 1.0 mm. Therefore a tool wear factor of 1.2 for medium milling was selected as per Table 18.

6.4.2   Sinamics 1PH8133-1DF02-0LA1 Spindle Torque and Power

The model takes into consideration the maximum allowable cutting power (P_{max}) and torque (T_{max}) for the Sinamics 1PH8133-1DF02-0LA1 spindle motor with which the Leadwell V-50L is equipped. The maximum torque curve is constant at 140 Nm for 0 rpm to 1500 rpm.
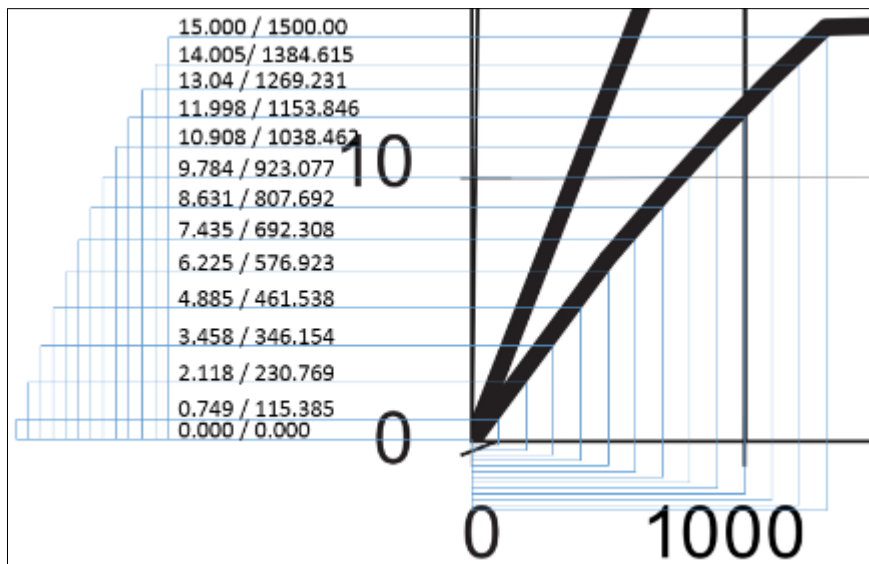
Figure 85: Sinamics 1PH8133-1DF02-0LA1 drive power curve [88]

The power curve (Figure 85) tends to become complex to express analytically. Improvement of cutting parameters requires a mathematical function to base the constraints upon. The equation for the spindle power delivery was derived by means of a regression line through the plotted points on the power curve as provided in the drive manual [88]. The nonlinear power function is an approximation.
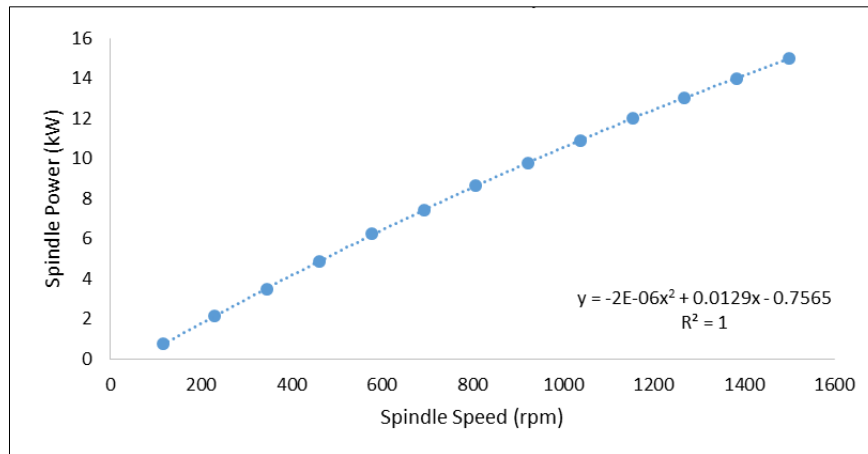
Figure 86: Sinamics SH 130 power vs. spindle speed function

The approximate equation for the maximum allowable spindle power is (from Figure 86):

$$P_{max} = -2E^{-6}x^2 + 0.0219x + 0.7565$$
[Eq. 6.12]

Where P_{max} is the maximum allowable spindle power and x is revolutions per minute at any given point.

6.4.3 Effective Cutting Diameter

The effective cutting diameter for the KSRM cutter and RCGX inserts is determined through the application of equation 6.1. On the other hand, the effective cutting diameter for the ISCAR cutter is calculated from the geometric characteristics of its inserts and how they seat in the cutter body. The equation for effective cutting diameter for the ISCAR insert at a specific depth can be derived as:

$$D_{max.H} = D_c + \left[2\left(\frac{a_p}{\tan 17}\right)\right] + (3.46a_p)$$
[Eq. 6.13]

Where $D_{max.H}$ is effective cutting diameter (mm), a_p is the ADOC, D_c is the diameter of cutter body (mm), $\tan 17$ is the tangent of the rake angle of the insert. Note the "H" added to the D_{max} notation to specify reference to the hexagonal ISCAR insert.

6.4.4 Other Cutting Parameters

The machinability factor for 15-5 PH Stainless steel is 2.15 (from Table 19), taking into account an average W/D ratio of 0.67 ≤ W/D ≤ 1.0 for the machining operation. The engagement angle and the number of teeth in the cut is represented by equations 6.3 to 6.6 The cutting force required at the spindle is formulated by using equation 6.7 and the cutting speed is calculated with equation 6.8. The table speed is determined through equation 6.9 and the average cross sectional area of the undeformed chip is represented by equation 6.10 with reference to Figure 84 and taking into account the insert geometry.

Material removal rate is calculated with equation 6.11 and the cutting power required at the spindle is determined by substituting values for cutting speed and force into equation 6.14. The cutting torque

required at the spindle is calculated using the required force and effective cutting diameter of a tool with hexagonal inserts:

$$T_s = \frac{F_c \times D_{max.H}}{2000}$$
[Eq. 6.14]

Where T_s is the torque required at the spindle (Nm), F_c is the cutting force and D_{max} is the effective cutting diameter of the round or hexagonal inserts (m), depending on which cutter is in use [45].

6.5 ISCAR EXPERIMENTS

Scope for the adjustment of machining parameters according to the outputs from the nonlinear program was provided by Daliff Engineering.

The computer-aided manufacturing (CAM) milling program followed a helical path down the outside of the billet as shown in Figure 87. This was the case for both the ISCAR and Kennametal cutters.

Figure 87: Helical milling path for roughing of the billet

6.5.1 Nonlinear Programming

The problem of maximising the material removal rate for the ISCAR cutter, depending on operational constraints can be formulated as follows: Let: Z_n = 4; S = 1126; D_c = 22; a_e = 28.5; C_w = 1.2; C_m = 2.15. Equation 6.13 is used to calculate the $D_{max.H}$ and equation 6.12 is used to calculate the power constraint placed by the spindle. Equations 6.2 - 6.11 and 6.14 are used to calculate values for the cutting parameters.

Maximise:

$$MRR = \frac{a_p \times a_e \times n \times f_z \times z_n}{1000}$$
[Material Removal Rate]

Subject to:

$$P_{max} = -2E^{-6}x^2 + 0.0219x + 0.7565$$
[Spindle Power]

$$T_{max} = \frac{F_c \times D_{max.H}}{2000}$$ [Spindle Torque]

$$n = \frac{1000 \times v_c}{\pi \times D_c}$$ [Spindle Speed]

For: $0 \leq a_p \leq 0.85; 0 \leq f_z \leq 1; 0 \leq n \leq 1100; 0 \leq T_{max} \leq 140; 0 \leq P_{max} \leq 17.83 \ (at \ 1100 \ rpm)$

6.5.2 Sensitivity Analysis of Nonlinear Programming Results

The following values were used in the nonlinear model: $z_n = 4; S = 1126; D_c = 22; a_e = 28.5; \frac{W}{D} = 0.934; C_m = 2.15; C_w = 1.2$. Nonlinear program results are shown in Table 20:

Table 20: Nonlinear program results and sensitivity analysis

Parameter	Type	Value	Status	Slack	Lagrange Multiplier
MRR	Objective	81.28 cm^3/min	Obj. Function	NA	0
$a_p \geq 0$	Variable	0.85 mm	Not Binding	0.85	0
$a_p \leq 0.85$	Variable	0.85 mm	Binding	0	38.35
$f_z \geq 0$	Variable	0.76 mm	Not Binding	0.76	0
$f_z \leq 1$	Variable	0.76 mm	Not Binding	0.24	0
$n \geq 0$	Variable	1100 rpm	Not Binding	1100	0
n ≤ 1100	Variable	1100 rpm	Binding	0	0.05
$T_{max} \leq 140$	Parameter	47.97 Nm	Not Binding	92.03	0
$P_{max} \leq 17.83$	Parameter	17.83 Kw	Binding	0	4.56

Binding factors were the maximum allowable ADOC, spindle speed and available power at the spindle. Slack values are 0.24 for the feed per tooth and 92.03 Nm for the available torque. The model returned a maximum MRR of 81.28 cm^3/min, while satisfying all constraints.

6.5.3 Experimental Results

The cutting parameters for the ISCAR FF EWX D32-4-060-W32-05 cutter were programmed into the Leadwell V-50L PLC. The parameters were taken from the nonlinear program outputs. They are: f_z = 0.75 mm; a_p = 0.85 mm; n = 1100 rpm with a theoretically calculated MRR of 81.28 cm^3/min.

Four billets were roughed out with the same inserts, not indexed between experiments. Parameters remained unchanged between experiments. The total cutting time of the four billets was 18:54 minutes, which results in an average of 4:43 minutes per billet. A surface roughness in excess of 320 μm, which is the maximum measureable roughness for the Mitutoyo SJ-201P, was recorded. The experiments are tabulated in Table 21:

CHAPTER : PRACTICAL WORK WITH INDUSTRY PARTNER

Table 21: ISCAR tabulated experimental results

#	a_p	f_z	n	T_{max}	P_{max}	$D_{max.H}$	Z_c	v_c	MRR	T_s	P_s	Time (mm:ss)	R_a (µm)
1	0.85	0.75	1100	140	17.83	30.5	1.67	76.0	81.29	47.97	17.8	04:38	> 320
2	0.85	0.75	1100	140	17.83	30.5	1.67	76.0	81.29	47.97	17.8	04:40	> 320
3	0.85	0.75	1100	140	17.83	30.5	1.67	76.0	81.29	47.97	17.8	04:45	> 320
4	0.85	0.75	1100	140	17.83	30.5	1.67	76.0	81.29	47.97	17.8	04:55	> 320

The parameters for a_p, f_z and n are inputs. T_{max} and P_{max} are constraints for the nonlinear program. The values underlined in the table are theoretically calculated. Cutting time was measured using a stopwatch to indicate the time from cutter engagement with material to disengagement. Due to dry cutting during this experiment, it is likely that chips were re-cut. The inserts were numbered and removed for microscope analysis.

6.5.4   Microscope Analysis of ISCAR H600 WXCU 05T312T Inserts

Uniform flank wear was observed on the minor flanks of each of the four inserts (VB 1). Localized wear (VB 3) was observed on the major flank of all four inserts in the form of notches. Table 22 shows the measured tool wear type detected on each flank face. Rake face wear was also inspected.

Cratering (KT 1) was found to have formed on all the insert rake faces. These phenomena could not be quantified with respect to its dimensions, but the flank wear amounts could be measured using an Olympus GX51 Microscope. The inserts were removed after the fourth experiment to examine tool wear over the total cutting time of 18:54 minutes. The GX51 was set to 20x magnification (50 µm).

Table 22: ISCAR average uniform tool wear and maximum chip size (µm)

Insert #	Minor Flank, Uniform Wear (VB 1)	Major Flank, Localized Wear (VB 3)
1	30.82	171.52
2	37.59	178.88
3	41.13	176.96
4	43.26	100.80
Average	38.20	157.04

Testing time of approximately 20 minutes is classified as "short" in ISO 8988-1 : 1989 [55]. The standard prescribes that under short testing, VB 1 of 200 µm is the maximum allowable wear for useful tool life. Furthermore, VB 3 is limited to 1000 µm. Therefore the results obtained during the ISCAR tests fall well within the guidelines set forth by the international standard for milling tool wear testing.
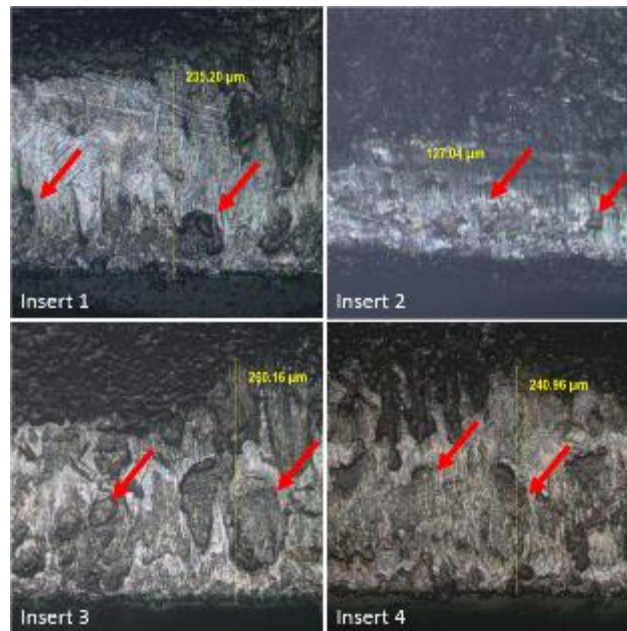
Figure 88: ISCAR H600 WXCU 05T312T cratering on rake face (at 50 µm)

The cratering phenomena on the rake faces are indicated with red arrows in Figure 88. This is an indication of high temperatures at the cutting interface due to the absence of coolant.

6.6 KENNAMETAL EXPERIMENTS

The KSRM63A04RC20BB cutter with four new RCGX2006M0SGF inserts was mounted on the Leadwell V-50L. The workpiece was mounted using the existing pedestal clamping system as shown in Figure 89.

Figure 89: KSRM cutter and four new RCGX inserts on the Leadwell V-50L

Through spindle coolant was used for cutting experiments with the HPTSC-ST cutter. The maximum coolant pressure provided by the Leadwell V-50L is 3 bar and is therefore not appropriate for use with the KSRM cutter. Kennametal specifies a coolant pressure of at least 30 bar for all Beyond Blast applications [89].

6.6.1 Nonlinear Programming

A maximum spindle speed of 900 rpm was selected for the first test to examine the cutter performance at lower rpm's due to the low coolant pressure. The problem of maximising the material removal rate for the KSRM cutter, depending on operational constraints can now be formulated. Let: Z_n = 4; S = 1126; D_c = 43; a_e

= 28.5; C_w = 1.2; C_m = 2.15. Eq. 6.25 is used to calculate the power constraint placed by the spindle. Eq. 6.1 is now used to calculate $D_{max.R}$. Equations 6.1 - 6.12 and 6.14 are used to calculate values for the cutting parameters.

Maximise:

$$MRR = \frac{a_p \times a_e \times n \times f_z \times z_n}{1000}$$ [Material Removal Rate]

Subject to:

$$P_{max} = -2E^{-6}x^2 + 0.0219x + 0.7565$$ [Spindle Power]

$$T_{max} = \frac{F_c \times D_{max.R}}{2000}$$ [Spindle Torque]

$$n = \frac{1000 \times v_c}{\pi \times D_c}$$ [Spindle Speed]

For: $0 \leq a_p \leq 4.0; 0 \leq f_z \leq 0.2; 0 \leq n \leq 900; 0 \leq T_{max} \leq 140; 0 \leq P_{max} \leq 15.63 \ (at \ 900 \ rpm)$

6.6.2 Sensitivity Analysis of Nonlinear Programming Results

The following values were used in the nonlinear model: $z_n = 4; S = 1126; D_c = 43; a_e = 28.5; \frac{W}{D} = 0.4831; C_m = 2.15; C_w = 1.2$. The nonlinear program results are shown in Table 23:

Table 23: Nonlinear program results and sensitivity analysis

Parameter	Type	Value	Status	Slack	Lagrange Multiplier
MRR	Objective	62.24 cm^3/min	Obj. Function	NA	0
$a_p \geq 0$	Variable	4.0 mm	Not Binding	4.0	0
$a_p \leq 4.0$	Variable	4.0 mm	Binding	0	1.0
$f_z \geq 0$	Variable	0.15 mm	Not Binding	0.15	0
$f_z \leq 0.2$	Variable	0.15 mm	Not Binding	0.05	0
$n \geq 0$	Variable	900 rpm	Not Binding	900	0
n $\leq$ 900	Variable	900 rpm	Binding	0	0.05
$T_{max} \leq 140$	Parameter	50.87 Nm	Not Binding	89.13	3.98
$P_{max} \leq 15.63$	Parameter	15.63 Kw	Binding	0	0

Binding factors were the maximum allowable ADOC, spindle speed and available power at the spindle. Slack values are 0.05 mm for the feed per tooth, and 89.13 Nm for the available torque. The model returned a maximum MRR of 62.24 cm^3/min, while satisfying all constraints.

The cutting parameters were adjusted for each one of the five experiments with the KSRM cutter. The total cutting time during the first experiment was 7:37 minutes. The inserts were indexed after every experiment.

The cutting parameters were adjusted for experiment two as shown in Table 24. According to theoretically calculated values, T_s does not exceed T_{max}. The spindle power was theoretically calculated to be upon the threshold of the approximated maximum allowable spindle power. During experiment two, the cutter ceased in the cut, shattering the four inserts. As a results, tool wear could not be measured for experiment one and two. Although undesirable for production purposes, the shattering inserts verify the calculated theoretical power limit.

Table 24: Kennametal tabulated experiment results

#	a_p	f_z	n	T_{max}	P_{max}	$D_{max.H}$	Z_c	v_c	MRR	T_s	P_s	Time (mm:ss)	R_a (µm)
1	4.00	0.15	900	140	15.63	59.0	0.98	121.6	62.24	50.87	15.63	07:37	0.57
2	5.66	0.32	683	140	12.80	61.0	0.99	131.0	141.69	170.70	12.21	NaN	NaN
3	2.50	0.15	1953	140	22.72	56.2	1.02	345.0	87.22	7.54	1.54	05:24	0.57
4	2.50	0.17	2110	140	22.83	56.2	1.02	372.7	101.56	8.76	1.94	04:40	0.57
5	2.50	0.20	1500	140	21.03	56.2	1.02	265.0	87.00	12.72	2.00	05:10	0.57

The machine was reset, new inserts were attached and experiment three was initiated with different machining parameters as shown in Table 24. The underlined values in the table are theoretically calculated. During experiment three there was significant chatter, which caused chipping of the rake face on the RCGX inserts. It was suspected that the pedestal clamp caused deflection and therefore the pedestal was removed after experiment three and the workpiece was mounted directly to the machine bed.

During experiment four and five chatter was decreased, but tool chipping was still encountered. An average surface roughness of 0.57 µm was measured on the inside diameter of billets one and three to five, using the on-site laboratory's Mitutoyo SJ-201P roughness tester. The total machining time for the four successfully cut billets was 22:51 minutes with an average of 05:42 minutes per billet.

As a result of the low coolant pressure provided to the KSRM cutter, it is likely that chips were re-cut, because adequate evacuation was not possible. In addition, effective chip lifting effect (Figure 14) could not be achieved as the recommended minimum coolant pressure for this specific tool is 35 bar.

6.6.3   Microscope Analysis of Kennametal RCGX2006M0SGF Inserts

Inserts one to four were removed and analysed using an Olympus GX51 Microscope set to 5x magnification (200 µm). Tool wear was measured for every experiment from the third experiment onwards. Due to the inserts shattering during experiment two, it was impossible to recover these inserts for microscope

analysis. However, inserts from experiments three, four and five provide tool wear evidence. Uniform flank wear (VB 1) was observed on the minor flank and localised notching (VB 3) was observed on the major flank as shown in Table 25.

Table 25: RCGX2006M0SGF insert wear

Insert	EXPERIMENT 3		EXPERIMENT 4		EXPERIMENT 5	
	Minor Flank, Uniform Wear (VB 1)	Major Flank, Localized Wear (VB 3)	Minor Flank, Uniform Wear (VB 1)	Major Flank, Localized Wear (VB 3)	Minor Flank, Uniform Wear (VB 1)	Major Flank, Localized Wear (VB 3)
1	102.84	560.64	65.00	1040.64	33.85	211.20
2	72.41	691.20	61.04	839.68	34.61	515.84
3	74.34	1214.72	55.04	678.40	35.84	194.56
4	93.82	1018.88	63.98	529.92	38.11	157.44
Ave.	85.85	974.93	61.27	772.16	35.60	269.76

There is a reduction in the average uniform tool wear on the minor flank (VB 1) from experiment three to experiment four due to the removal of the pedestal clamp. VB 1 was further reduced from experiment four through five by application of more conservative cutting parameters. Similarly, the average size of the localized notching observed on the major flanks was reduced from experiment three to five as shown in Table 25. According to ISO 8988-1 : 1989 [55], the total uniform wear criteria falls under "short" testing, because the average machining time per experiment was approximately five minutes. Therefore, the specified criteria for the uniform tool wear on the minor flank (VB 1) is 200 μm and the localized wear (VB 3) limit is 1000 μm. In terms of these criteria, the RCGX2006M0SGF inserts conform to the ISO standard.

However, analysis of the rake faces revealed localized, macro chipping (CH 3) [55] as shown in (Figure 90 b). The average chip length observed on the rake face is reduced from experiment three to five, due to aforementioned factors as shown in Table 26.

Table 26: RCGX2006M0SGF insert chipping size (μm)

Insert #	Exp. 3	Exp. 4	Exp. 5
1	1246.72	1268.48	none
2	1331.20	771.84	736.00
3	812.80	642.52	none
4	1112.32	505.60	none
Average	1125.76	797.11	736.00

ISO 8988-1 : 1989 [55] specifies the maximum chip length for macro chipping during a small testing time at 300 to 1000 μm. In terms of this criteria and also taking into consideration the observed degree of chipping on the rake faces of the inserts, conditions for the RCGX2006M0SGF are not ideal.
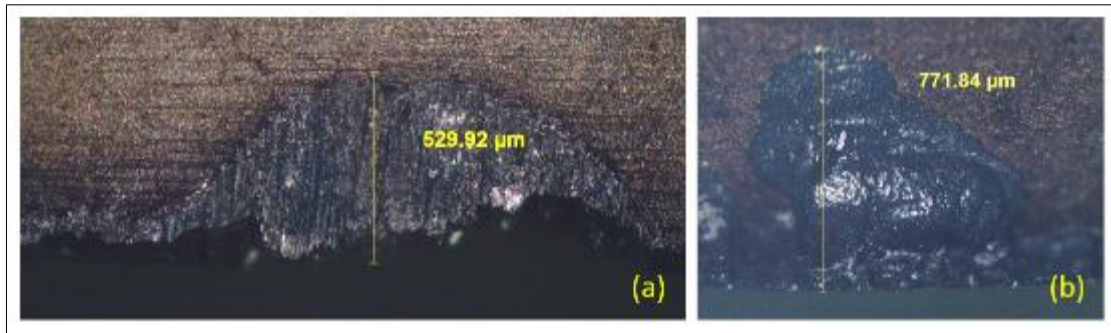
Figure 90: Kennametal tool wear: (a) Grooving, insert 4, exp. 4 (b) Flaking, insert 2, exp. 4 (at 200 μm)

The absence of rigid clamping and sufficient coolant pressure are the major contributing factors. The removal of the pedestal clamping device did not eliminate the tool chipping, but the average chipping size on the tool rake face was reduced.

6.7 PRODUCTIVITY AND SAVINGS

The KSRM cutter is not a feasible solution for roughing on the Leadwell V-50L mainly because of the lack of proper coolant pressure. Savings are interpreted in terms of the improvement of cutting parameters for the ISCAR cutter. Figure 91 illustrates the effect of the reduced roughing time on total lug machining time. The roughing time was reduced to an average of five minutes. This is a saving of 108 minutes per lug. It is an annual time saving of 172.8 hours, based on an annual volume of 96 units. A total time saving of 95.57% is achieved.
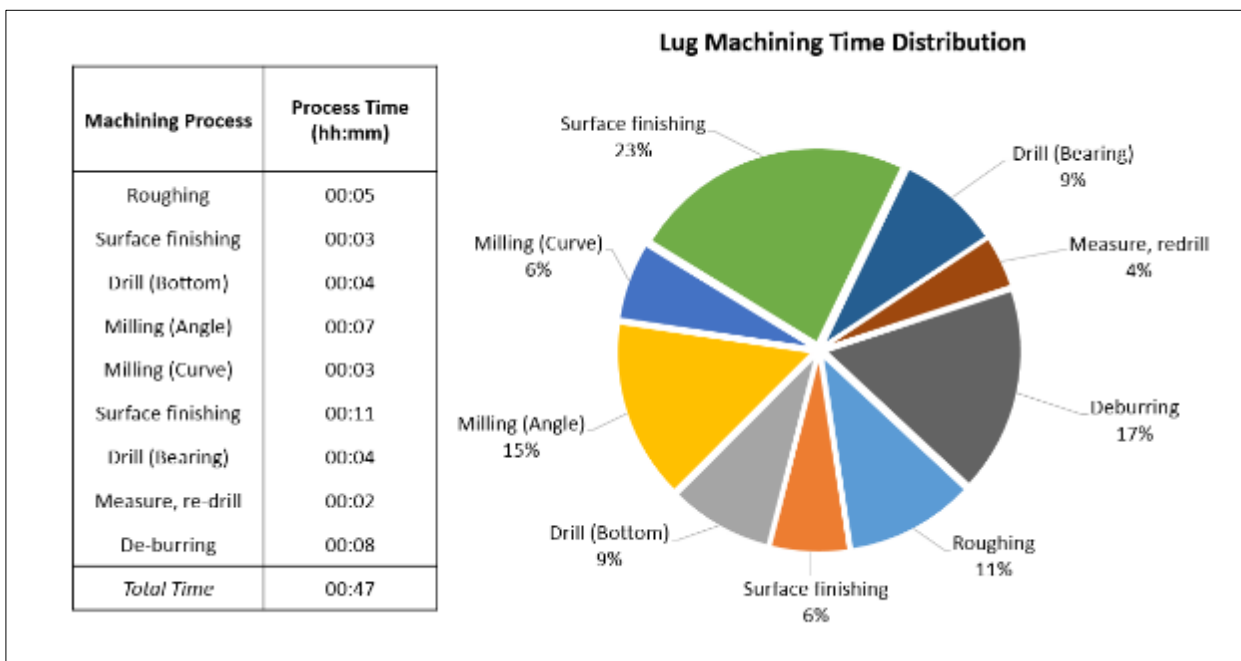
Figure 91: Airbus lug improved roughing time as percentage of total machining time

Taking into consideration the entire machining process of the Airbus lug (Figure 91) it is evident that the roughing process now occupies 11% of the total time required to machine the component. This paves the way for further improvement of other milling processes that occupy large quantities of time, such as the

second surface finishing process (23%). Further improvements can be achieved in the exact same method as was done with the ISCAR tool, keeping in mind that the tool geometry should be adapted to suit the new milling tool in question. This is necessary so that an accurate D_{max} value can be calculated, which subsequently dictates the accuracy of force, power and torque estimations at any given machining parameters.

6.8 ECONOMIC FEASIBILITY

The economic feasibility of split tools can be determined by comparing the ISCAR cutter's cost model to that of the split tools. The basis for comparison used is the cost per cm^3 (In Rand currency) removed for each tool. This can be expressed by the following formula as also used by Boeing Phantom Works during tool life and feasibility experiments [90]:

$$R/cm^3 = \frac{\left[\frac{T_c}{T_L} + \frac{R_m}{60} + \left(\frac{R_L}{60} \times \frac{T}{T_L}\right)\right]}{MRR}$$

[Eq. 6.15]

Where T_c is the tool cost of the inserts, T_L is the tool life in minutes (total), calculated by multiplying the amount of insert edges or indexing positions with the tool life per edge, R_m is the milling machine's hourly rate, R_L is the labour rate per hour and T is the tool change time in minutes. The data collected for milling the Airbus lug is used to populate Table 27 and Table 28. The cost/cm^3 is calculated by substituting values into equation 6.15.

Table 27: ISCAR cutter cost calculations

T =	15	Tool change time (min)
T_c =	R 928.40	Tool cost
T_L =	114	Tool life (min)
R_m =	R 450.00	Machine hourly rate (R/hr)
R_L =	R 50.00	Labour hourly rate (R/hr)
MRR =	81.28	cm^3/min
Cost/cm^3 =	R 0.19	(from eq. 6.15)

Table 28: Kennametal split tool cost calculations

T =	15	Tool change time (min)
T_c =	R 348.48	Tool cost
T_L =	30	Tool life (min)
R_m =	R 450.00	Machine hourly rate (R/hr)
R_L =	R 50.00	Labour hourly rate (R/hr)
MRR =	62.24	cm^3/min
Cost/cm^3 =	R 0.31	(from eq. 6.15)

The hourly machine rate and labour costs were obtained from the industry partner and the MRR's used for calculation were taken from the experimental results. Tool change time was measured during machining of the Airbus lugs and recorded as an average of 15 minutes per cutter. This is the time required to index all four inserts on each cutter. The ISCAR cutter provides a 63.16% reduction in cost per cm^3. This difference in cost can be attributed to the better tool life of the ISCAR inserts, compared to the split tool inserts, despite the lower cost of the split tool inserts (62.47% lower).

CHAPTER 7

CONCLUSIONS AND RECOMMENDATIONS

7.1 CONCLUSIONS

The examination of machinability factors such as surface finish, tool wear rate and chip control revealed no abnormalities. Uniform tool wear was observed during experimentation with negligible occurrences of non-uniform wear. Shearing of chips was observed at high cutting speeds, but according to findings from literature, this is a beneficial phenomenon when machining Ti-6Al-4V as surface finish is improved during shearing. Precision Coolant Technology assisted with chip lifting and evacuation. Further analysis of the cut chips provided evidence about the low temperatures and thorough chip removal at the cutting interface.

The cutting experiments generated useful data for modeling of tangential cutting forces with split tools. The primary research hypothesis was answered and the null hypothesis rejected. The research question regarding the predictive tangential cutting force model is answered satisfactorily and a second-order model fits the data at 95% confidence level. The predicted values show good agreement with experimental data and the model can therefore be used to navigate the experimental design space. The existing experiment design can be augmented by the addition of six star points to form a central composite design. This design is preferred, when significant curvature is present as shown by the first-order model. A model fitted to the data delivered by the central composite design will have to be tested for optimality, but evidence from significant curvature suggests that the existing full factorial design was already rather close to the optimal response surface. A model fitted to the optimal response surface would be valuable for predicting tangential cutting forces for the entire process without being limited to the design space.

The ANOVA for the second-order model gives a clear indication of the significant factors that affected cutting forces during experimentation. The interaction plots and 3-D response surfaces also show how these factors affect each other by indicating interactions. The factors affecting cutting force are (1) ADOC, (2) feedrate, and (3) cutting speed, respectively and in that order of significance. Regression analysis revealed no relationship between cutting force vs. tool wear or cutting force vs. surface roughness.

The surface finish achieved during laboratory experimentation is highly satisfactory. The maximum surface roughness on the outside diameter of the cut was reported as 1.26 micron that is below the requirement for the final surface finish for the selected industry partner component. The high material removal rate achieved during high levels of ADOC, feedrate and cutting speed promotes the feasibility of this cutter as a roughing tool as successive finishing operations would be reduced. It should be added that the large inserts and cutter diameter will limit the use of the tool to roughing out of large surface areas with large radius corners.

7.2 RECOMMENDATIONS FOR INDUSTRY PARTNER

The ISCAR FF EWX cutter provided a higher MRR than the Kennametal KSRM on the Leadwell V-50L. The improved MRR can be attributed to the ISCAR FF EWX cutter's smaller effective tool diameter compared to the Kennametal KSRM cutter (32mm vs. 63mm). Effective diameter directly affects the number of teeth in the cut (Z_c) for a given radial engagement (a_e). Since number of teeth in cut is a factor in calculating MRR, it proves that higher radial immersion ratios (W/D) are more productive than smaller radial immersions when only MRR is considered. Hence, in this case, due to the geometry of the component, the smaller diameter cutter proved more efficient.

The measured tool wear of the ISCAR FF EWX (VB 1 and VB 3) after experiments 1-4 fall within the ISO 8988-1 : 1989 criteria for face milling tool testing [55]. Notching was observed on the major flank and cratering was found on the rake face. It is recommended that coolant be used to improve tool life, more specifically to reduce the cratering in the rake face of the ISCAR H600 WXCU 05T312T inserts.

The measured tool wear of the Kennametal RCGX inserts after experiments 3-5 is not in agreement with the ISO 8988-1 : 1989 criteria. More specifically, the average chip size. The initial workpiece clamping method contributed to the chipping of the Kennametal RCGX inserts during experiments one, two and three.

Furthermore, the coolant pressure of 3 bar that is provided on the Leadwell V-50L is not sufficient for roughing at high feedrates with the Kennametal KSRM cutter. These cutters are designed for use with pressures of 30 bar and upward. Evidence suggests that adequate chip lifting was not achieved and therefore chips were re-cut, accelerating the tool wear rate through elevated temperatures at the cutting interface.

Notching was observed during experimentation with both cutters. According to the literature review, notching occurs in cases where previously machined sections are re-machined [56]. This is the case with a helical milling path as shown in Figure 87.

ISCAR tools cost 62.47% less per cm^3 of material removed. For the purpose of this particular machining process, taking into consideration operational and economic feasibility factors, it is recommended that the ISCAR FF EWX D32-4-060-W32-05 cutter and H600 WXCU 05T312T inserts be utilized for future use. The average major localized flank wear on the H600 WXCU 05T312T inserts was 157 µm for 18 minutes of machining. This falls well within the tool life requirements set by the industry partner and ISO standards.

A 95.57% time saving was achieved by increasing the cutting parameters of an existing roughing process. Other milling processes at Daliff Precision Engineering may be improved by means of the nonlinear programming model that was created for this project. The model for this project was created using MS Excel in a way that allows easy modification to accommodate different spindle power curves and cutter

geometries. The report explains in detail what is required to apply these changes for other processes. The time required for adjusting the model is negligible compared to the savings that are made as a result.

In terms of the research problem, it is recommended that it becomes common practice for Daliff Precision Engineering to analytically consider machining processes, if world class aerospace component machining is desired. The feasibility of split tool milling at the industry partner was explored and it can be concluded that it is not a feasible alternative at the moment, due to coolant pressure limitations on the Leadwell V-50L. The operating characteristics of the KSRM cutter were explored in laboratory experiments and in practice. The geometry of the selected aerospace component provides a challenge for the KSRM cutter. Despite these findings, laboratory experiments provide evidence that suggests that the Kennametal KSRM cutter holds the potential to save roughing time and reduce subsequent finishing processes. The KSRM cutter provides a surface finish that matches the industry partner's final finish requirement.

LIST OF REFERENCES

[1] H. Sibum, "Titanium and Titanium Alloys - From Raw Material to Semi-finished Products," *Advanced Engineering Materials,* vol. 5, no. 6, pp. 393-398, 4 July 2003.

[2] C. Cui, B. Hu, S. Liu and L. Zhao, "Titanium Alloy Production Technology, Market Prospects and Industry Development," *Materials & Design,* vol. 32, no. 3, pp. 1684-1691, March 2011.

[3] D. J. de Beer, "Establishment of Rapid Prototyping/Additive Manufacturing in South Africa," *The Journal of The Southern African Institute of Mining and Metalurgy,* vol. 111, no. 1, pp. 211-215, March 2011.

[4] G. Herlihy, "Metals Week," *Platts,* vol. 83, no. 16, p. 22, 16 April 2012.

[5] R. Singh, Introduction to Basic Manufacture Process and Workshop Technology, Darya Ganj, New Delhi: New Age International Publishers, 2006, p. 117.

[6] G. Lutering and J. C. Williams, Titanium (Engineering Materials and Processes), Berlin: Springer-Verlag Berling Heidelberg, 2007, p. 60.

[7] J. C. Aurich and D. Dornfield, "Burrs - Analysis, Control and Removal," in *Proceedings to the CIRP International Conference on Burrs*, University of Kaiserslautern, 2009.

[8] D. Koen, *Investigation of Novel Cooling Methods to Enhance Aerospace Component Manufacturing Practices,* Stellenbosch, Western Cape: Stellenbosch University, 2011, pp. 13, 47-52.

[9] G. A. Oosthuizen, *Innovative Cutting Materials for Finish Shoulder Milling Ti-6Al-4V,* Stellenbosch, Western Cape: Stellenbosch University, 2009, pp. 38, 58-60, 101.

[10] B. North, "Why Metalcutting (Especially in Aerospace) is Such and Exciting Field," in *5th Annual Americas HTEC CNC Educators Conference*, Phoenix, 2011.

[11] J. Cagan and C. M. Vogel, Creating Breakthrough Products: Revealing the Secrets that Drive Global Innovation, New Jersey: Pearson Education, FT Press, 2012.

[12] H. Jeong, D. Y. Lee, M. G. Lee, S. W. Lee, K. H. Park and G. D. Yang, "Eco-Friendly Face Milling of Titanium Alloy," *International Journal of Precision Engineering and Manufacturing,* vol. 15, no. 6, pp. 1159-1164, June 2014.

[13] E. Chiapinni, M. Monno, Q. Semeraro, M. Strano and S. Tirelli, "Experimental Comparison Between Traditional and Cryogenic Cooling Conditions in Rough Turning of Ti-6Al-4V," *Key Engineering Materials,* vol. 611, pp. 1174-1185, 2014.

[14] VOLUMILL, "US Air Force Announces Sustainable Manufacturing Successes," Wright-Patterson Air Force Base, Fairborn, 2011.

[15] Y. Ding and S. Y. Hong, "Cooling Approaches and Cutting Temperatures in Cryogenic Machining of Ti-6Al-4V," *International Journal of Machine Tools and Manufacture,* vol. 41, no. 10, pp. 1417-1437, 2001.

[16] F. Klocke, D. Lung, T. Cayli, B. Dobbeler and H. Sangermann, "Evaluation of Energy Efficiency in Cutting Aerospace Materials with High-Pressure Cooling Lubricant Supply," *International Journal of Precision Engineering and Manufacturing,* vol. 15, no. 6, pp. 1179-1185, June 2014.

[17] J. Bernardin and I. Mudawar, "Experimental And Statistical Investigation Of Changes In Surface Roughness Associated With Spray Quenching," *International Journal of Heat and Mass Transfer,* vol. 39, no. 10, pp. 2023-2037, 1996.

[18] J. Bonney, R. B. da Silva, E. O. Ezugwu, Á. R. Machado and F. Wisley, "Tool Life and Wear Mechanisms in High Speed Machining of Ti-6Al-4V Alloy with PCD Tools Under Various Coolant Pressures," *Journal of Materials Processing Technology,* vol. 213, no. 8, pp. 1459-1464, August 2013.

[19] E. O. Ezugwu, "Key Improvements in the Machining of Difficult-to-cut Aerospace Superalloys," *Machine Tools & Manufacture,* vol. 45, no. 12-13, pp. 1353-1367, 2005.

[20] U. Heisel, M. Lutz, D. Spath, U. Walter and R. A. Wassmer, "Application Of Minimum Quantity Cooling Lubrication Technology In Cutting Processes," *Production Engineering II,* vol. 1, no. 2, pp. 49-54, 1994.

[21] T. Aoyama, "Development Of A Mixture Supply System For Machining With Minimal Quantity Lubrication," *CIRP Annals-Manufacturing Technology,* vol. 51, no. 1, pp. 289-292, 2002.

[22] T. Aoyama, T. Ichikawa, Y. Saikawa and T. Takada, "High Speed Drilling and Tapping Using the Technique of Spindle Through MQL Supply," *Key Engineering Materials,* vol. 257, no. 1, pp. 559-564, 2004.

[23] M. Aoki, T. Aoyama, Y. Kakinuma and M. Yamashita, "Development Of A New Lean Lubrication System For Near Dry Machining Process," *CIRP Annals-Manufacturing Technology,* vol. 57, no. 1, pp. 125-128, 2008.

[24] W. Liu, Q. Liu, L. Yan and S. Yuan, "Effects of Cooling Air Temperature on Cryogenic Machining of Ti-6Al-4V Alloy," *Journal of Materials Processing Technology,* vol. 211, no. 3, pp. 356-362, 2011.

[25] M. Dhananchezian and M. Pradeep Kumar, "Cryogenic Turning Of The Ti-6Al-4V Alloy With Modified Cutting Tool Inserts," *Cryogenics,* vol. 51, no. 1, pp. 34-40, 2011.

[26] Y. Kaynak, "Evaluation of Machining Performance in Cryogenic Machining of Inconel 718 and Comparison with Dry and MQL Machining," *International Journal of Advanced Manufacturing Technology,* vol. 72, no. 5-8, pp. 919-933, 2014.

[27] K. Rajurkar and Z. Wang, "Cryogenic Machining of Hard-to-cut Materials," *Wear,* vol. 239, no. 2, pp. 168-175, 2000.

[28] M. Gowrishankar, A. Nandy and S. Paul, "Some Studies On High-pressure Cooling In Turning of Ti-6Al-4V," *International Journal of Machine Tools and Manufacture,* vol. 49, no. 2, pp. 182-198, 2009.

[29] M. Bermingham, M. Dargusch, D. Kent and S. Palanisamy, "A Comparison of Cryogenic and High Pressure Emulsion Cooling Technologies on Tool Life and Chip Morphology in Ti–6Al–4V Cutting," *Journal of Materials Processing Technology,* vol. 212, no. 4, pp. 752-765, 2012.

[30] T.-H. Chang, Z.-M. Chen, C.-C. Du, S.-Y. Hsu and C.-C. Lin, "Coolant Through Spindle Device". USA

Patent US Patent 5,327,979, 12 July 1994.

[31] E. Ezugwu and Z. Wang, "Titanium Alloys And Their Machinability - A Review," *Journal of Materials Processing Technology,* vol. 68, no. 3, pp. 262-274, 1997.

[32] M. Nalbant and Y. Yildiz, "A Review of Cryogenic Cooling in Machining Processes," *International Journal of Machine Tools and Manufacture,* vol. 48, no. 9, pp. 947-964, 2008.

[33] J. Bonney, E. Ezugwu and Y. Yamane, "An Overview Of The Machinability Of Aeroengine Alloys," *Journal of Materials Processing Technology,* vol. 134, no. 2, pp. 233-253, 2003.

[34] MAG, "Cryogenics," 1 August 2010. [Online]. Available: http://www.mag-ias.com/en/mag/technologies/cryogenics.html. [Accessed 14 February 2014].

[35] Sandvik Coromant, "Metal Cutting Technical Guide - Milling," 30 January 2006. [Online]. Available: http://www2.coromant.sandvik.com/coromant/pdf/metalworking_products_061/tech_d_1.pdf. [Accessed 14 February 2014].

[36] M. Heuwinkel and A. Richter, "Let's Talk Radial," *Walter USA Inc.,* vol. 57, no. 5, pp. 1-3, 1 May 2005.

[37] M. P. Groover, Fundamentals of Modern Manufacturing, 3rd ed., New York: John Wiley & Sons, 2010, pp. 82-86, 543-549.

[38] S. Kalpakjian, H. Musa and S. R. Schmid, Manufacturing Engineering and Technology, 6th ed., London: Prentice Hall, 2009, pp. 574-583.

[39] R. Boyer, E. Colling and G. Welsch, Materials Properties Handbook: Titanium Alloys, 4th ed., Novelty, OH: ASM International, 2007, pp. 483-484, 515.

[40] H. M. Cetin, E. Demirbas, E. Kuram and B. Ozcelik, "Experimental Investigations of Vegetable Based Cutting Fluids with Extreme Pressure During Turning of AISI 304L," *Tribology International,* vol. 44, no. 2011, p. 1865, 2011.

[41] M. Estrems, F. Faura and P. Franco, "Influence of Radial and Axial Runouts on Surface Roughness in Face Milling with Round Insert Cutting Tools," *International Journal of Machine Tools & Manufacture,* vol. 44, no. 2004, pp. 1555-1565, 2004.

[42] D. K. Baek, H. S. Kim and T. J. Ko, "Optimization of Feedrate in a Face Milling Operation Using a Surface Roughness Model," *International Journal of Machine Tools & Manufacture,* vol. 41, no. 2001, pp. 451-461, 2000.

[43] S. Rawal, J. Brantley and N. Karabudak, "Additive Manufacturing of Ti-6Al-4V Alloy Components for Spacecraft Applications," Lockheed Martin Space Systems, 1 January 2014. [Online]. Available: http://www.techbriefs.com/component/content/article/7-ntb/tech-briefs/manufacturing-and-prototyping/18883. [Accessed 30 June 2014].

[44] Mitutoyo America Corporation, "Brochures," 1 Dec 2009. [Online]. Available: http://www.mitutoyo.com/wp-content/uploads/2012/11/1984_Surf_Roughness_PG.pdf. [Accessed 30 June 2014].

[45] Kennametal, "Catalog Archives: Milling 6050 Master Catalog - Metric," 24 April 2007. [Online]. Available: http://www.kennametal.com/en/resources/catalogs-and-literature/catalog-archives.html. [Accessed 18 June 2014].

[46] F. Klocke and A. Kuchle, Manufacturing Processes 1, 1st ed., Aachen: Springer Science & Business Media, 2011, pp. 54-55.

[47] M. E. Martellotti, "An Analysis of the Millign Process," *ASME Transactions,* vol. 64, no. 8, pp. 677-700, 9141.

[48] P. G. Benardos and G. C. Vosniakos, "Predicting Surface Roughness in Machining: A Review," *International Journal of Machine Tools & Manufacture,* vol. 43, no. 2003, pp. 833-844, 2002.

[49] P. G. Benardos and G. C. Vosniakos, "Prediction of surface roughness in CNC face milling using neural networks and Taguchi's design of experiments," *Robotics and Computer Integrated Manufacturing,* vol. 18, no. 2002, pp. 343-354, 2002.

[50] M. Bayramoglu and B. Ozcelik, "The Statistical Modeling of Surface Roughness in High-speed Flat End Milling," *International Journal of Machine Tools & Manufacture,* vol. 46, no. 2006, pp. 1395-1402, 2005.

[51] M. Gostimirovic, P. Kovac, V. Pucovsky, D. Rodic and B. Savkovic, "Application of Fuzzy Logic and Regression Analysis for Modeling Surface Roughness in Face Milling," *Journal of Intelligent Manufacturing,* vol. 24, no. 4, pp. 755-762, 2013.

[52] T. Ozel and M. Sima, "Modified Material Constitutive Models for Serrated Chip Formation Simulations and Experimental Validation in Machining of Titanium Alloy Ti-6Al-4V," *International Journal of Machine Tools & Manufacture,* vol. 50, no. 2010, pp. 943-960, 2010.

[53] R. Komanduri and B. F. von Turkovich, "New Obseravations on the Mechanism of Chip Formation when MAchining Titanium Alloys," *Wear,* vol. 69, no. 1981, pp. 179-188, 1981.

[54] R. K. Rajput, A Textbook of Manufacturing Technology, 1st ed., New Delhi: Firewall Media, 2007, pp. 363-364.

[55] International Organization for Standardization, *Tool Life Testing in Milling - Part 1: Face Milling,* 1st ed., Vols. ISO 8688-1, Genève: International Organization for Standardization, 1989.

[56] Sandvik Coromant, "Wear on Cutting Edges," Sandvik Coromoant, 20 February 2002. [Online]. Available: http://www.sandvik.coromant.com/en-gb/knowledge/materials/cutting_tool_materials/wear_on_cutting_edges/pages/default.aspx. [Accessed 4 July 2014].

[57] International Organization for Standardization, *Tool Life Testing in Milling - Part 2: End Milling,* 1st ed., Vols. ISO 8688-2, Genève: International Organization for Standardization, 1989.

[58] V. Marinov, Manufacturing Processes for Metal Products, 2nd ed., Dubuque: Kendall Hunt Publishing Company, 2010, pp. 77-80.

[59] A. Devillez, S. Lesko and W. Mozer, "Cutting Tool Crater Wear Measurement with White Light

Interferometry," *Wear,* vol. 256, no. 1-2, pp. 56-65, 2004.

[60] G. S. Hong, W. H. Wang and Y. S. Wong, "3D Measurement of Crater Wear by Phase Shifting Method," *Wear,* vol. 261, no. 2, pp. 164-171, 2006.

[61] H. Kato, K. Kubota, Y. Morimoto, K. Nakagaki, T. Shikimura and K. Shintani, "Study on High-Efficiency Finish Turning of Carburized Hardened Steel with Driven Rotary Cutting," *International Journal of Automation Technology,* vol. 7, no. 3, pp. 321-328, 2013.

[62] A. Abdullah, C. H. Che-Haron and A. Jawaid, "Tool Wear Characteristics in Turning of Titanium Alloy Ti-6246," *Journal of Materials Processing Technology,* Vols. 92-93, no. 1, pp. 329-334, 1999.

[63] E. Merchant, "Mechanics of the Metal Cutting Process II. Plasticity Conditions in Orthogonal Cutting.," *Journal of Applied Physics,* vol. 16, no. 1945, pp. 318-324, 1945.

[64] SECO, "Education (STEP)," SECO, 4 September 2008. [Online]. Available: http://www.secotools.com/CorpWeb/north_america/STEP_training/STEP_1_web.html. [Accessed 30 June 2014].

[65] B. Winegard, "Application Support and Training, SECO," SECO, Detroit, 2012.

[66] V. Chandrasekharan, R. E. DeVor and S. G. Kapoor, "A Mechanistic Approach to Predicting the Cutting Forces in Drilling: With Application to Fiber-Reinforced Composite Materials," *Journal of Engineering for Industry,* vol. 117, no. 4, pp. 559-570, 1995.

[67] P. K. Baro, S. S. Joshi and S. G. Kapoor, "Modeling of Cutting Forces in a Face-Milling Operation with Self-Propelled Round Insert Milling Cutter," *International Journal of Machine Tools & Manufacture,* vol. 45, no. 7-8, pp. 831-839, 2005.

[68] Y. Huang and S. Y. Liang, "Modeling of Cutting Forces Under Hard Turning Conditions Considering Tool Wear Effect," *Journal of Manufacturing Science and Engineering,* vol. 127, no. 2, pp. 262-270, 2005.

[69] C. C. Hsieh, A. J. Shih and J. S. Strenkowski, "An Analytical Finite Element Technique for Predicting Thrust Force and Torque in Drilling," *International Journal of Machine Tools and Manufacture,* vol. 44, no. 12-13, pp. 1413-1421, 2004.

[70] T. Altan and T. Özel, "Process Simulation Using Finite Element Method — Prediction of Cutting Forces, Tool Stresses and Temperatures in High-Speed Flat End Milling," *International Journal of Machine Tools and Manufacture,* vol. 40, no. 5, pp. 713-738, 2000.

[71] M. R. Hossan and L. Qian, "Effect on Cutting Force in Turning Hardened Tool Steels with Cubic Boron Nitride Inserts," *Journal of Materials Processing Technology,* vol. 191, no. 1-3, pp. 274-278, 2007.

[72] H. Hocheng and C. C. Tsao, "Parametric Study on Thrust Force of Core Drill," *Journal of Materials Processing Technology,* Vols. 192-193, no. 1, pp. 37-40, 2007.

[73] N. Amin, W. F. Faris and A. Patwari, "Prediction of Tangential Cutting Force in End Milling of Medium Carbon Steel by Coupling Design of Experiment and Response Surface Methodology," *Journal of Mechanical Engineering,* vol. 40, no. 2, pp. 95-103, 2009.

LIST OF REFERENCES

[74] K. Bouacha, T. Mabrouki, J.-F. Rigal and M. A. Yallese, "Statistical Analysis of Surface Roughness and Cutting Forces Using Response Surface Methodology in Hard Turning of AISI 52100 Bearing Steel with CBN Tool," *International Journal of Refractory Metals and Hard Materials,* vol. 28, no. 3, pp. 349-361, 2010.

[75] D. C. Montgomery, Design and Analysis of Experiments, 8th ed., New Jersey: John Wiley & Sons, Inc., 2013.

[76] D. C. Montgomery and G. C. Runger, Applied Statistics and Probability for Engneers, 4th ed., New Jersey: John wiley & Sons, 2007.

[77] B. S. El-Haik and K. Yang, Design for Six Sigma, Chapter 17 - Response Surface Methodology, Part 17, 2nd ed., New York: Mcgraw-Hill, 2009, pp. 611-678.

[78] A. I. Khuri, Response Surface Methodology and Related Topics, 1st ed., New Jersey: World Scientific, 2006, pp. 409-427.

[79] E. Isakov, "Tackling Titanium," *Cutting Tool Engineering,* vol. 61, no. 6, p. 1, 1 June 2009.

[80] Kennametal, "Metalworking Catalog Archive," 15 January 2013. [Online]. Available: http://www.kennametal.com/content/dam/kennametal/kennametal/common/Resources/Catalogs-Literature/Metalworking/Metalworking%20Catalog%20Archive.html. [Accessed 15 05 2014].

[81] A. Horling, L. Hultman, L. Karlsson, T. Larsson, H. P. Mayrhofer, C. Mitterer and J. Sjolen, "Self-organized Nanostructures in the Ti-Al-N System," *Applied Physics Letters,* vol. 83, no. 10, pp. 2049-2051, 2003.

[82] Kennametal, "Innovations Master Catalogue," 30 March 2012. [Online]. Available: http://www.kennametal.com/en/promotions/kennametal-master-catalog-2013.html. [Accessed 17 June 2014].

[83] H. Tschätsch and A. Reichelt, Applied Machining Technology, 8th ed., New York: Springer, 2010, pp. 173-195.

[84] M. J. Anderson and P. J. Whitcomb, DOE Simplified: Practical Tools for Effective Experimentation, Second ed., London: Taylor & Francis, 2007, pp. 3-1 to 3-23.

[85] C. M. Anderson-Cook, D. C. Montgomery and R. H. Myers, Response Surface Methodology, 2nd ed., New Jersey: John Wiley & Sons, 2011.

[86] Aubert & Duval, "Our Materials," 11 October 2010. [Online]. Available: http://www.aubertduval.com/uploads/tx_obladygestionproduit/X15U5W_GB.pdf. [Accessed 7 July 2014].

[87] E. Oberg, Machinery's Handbook, 29th Edition, 29 ed., South Norwalk: Industrial Press, 2012, p. 1086.

[88] Siemens Automation, "Sinumerick & Sinamics," 15 January 2010. [Online]. Available: www.ad.siemens.com.cn. [Accessed 12 May 2014].

[89] Kennametal, "Catalogs and Literature," 20 March 2012. [Online]. Available:

http://www.kennametal.com/content/dam/kennametal/kennametal/common/Resources/Catalogs-Literature/Industry%20Solutions.html. [Accessed 7 July 2014].

[90] Boeing Technology Phantom Works, "High Performance Ti Machining," The Boeing Company, St. Louis, 2008.

APPENDICES

APPENDIX A

Table V   Percentage Points of the F-Distribution (continued)

$f_{0.05,v_1,v_2}$

Degrees of freedom for the numerator (v_1)

v_2	1	2	3	4	5	6	7	8	9	10	12	15	20	24	30	40	60	120	∞
1	161.4	199.5	215.7	224.6	230.2	234.0	236.8	238.9	240.5	241.9	243.9	245.9	248.0	249.1	250.1	251.1	252.2	253.3	254.3
2	18.51	19.00	19.16	19.25	19.30	19.33	19.35	19.37	19.38	19.40	19.41	19.43	19.45	19.45	19.46	19.47	19.48	19.49	19.50
3	10.13	9.55	9.28	9.12	9.01	8.94	8.89	8.85	8.81	8.79	8.74	8.70	8.66	8.64	8.62	8.59	8.57	8.55	8.53
4	7.71	6.94	6.59	6.39	6.26	6.16	6.09	6.04	6.00	5.96	5.91	5.86	5.80	5.77	5.75	5.72	5.69	5.66	5.63
5	6.61	5.79	5.41	5.19	5.05	4.95	4.88	4.82	4.77	4.74	4.68	4.62	4.56	4.53	4.50	4.46	4.43	4.40	4.36
6	5.99	5.14	4.76	4.53	4.39	4.28	4.21	4.15	4.10	4.06	4.00	3.94	3.87	3.84	3.81	3.77	3.74	3.70	3.67
7	5.59	4.74	4.35	4.12	3.97	3.87	3.79	3.73	3.68	3.64	3.57	3.51	3.44	3.41	3.38	3.34	3.30	3.27	3.23
8	5.32	4.46	4.07	3.84	3.69	3.58	3.50	3.44	3.39	3.35	3.28	3.22	3.15	3.12	3.08	3.04	3.01	2.97	2.93
9	5.12	4.26	3.86	3.63	3.48	3.37	3.29	3.23	3.18	3.14	3.07	3.01	2.94	2.90	2.86	2.83	2.79	2.75	2.71
10	4.96	4.10	3.71	3.48	3.33	3.22	3.14	3.07	3.02	2.98	2.91	2.85	2.77	2.74	2.70	2.66	2.62	2.58	2.54
11	4.84	3.98	3.59	3.36	3.20	3.09	3.01	2.95	2.90	2.85	2.79	2.72	2.65	2.61	2.57	2.53	2.49	2.45	2.40
12	4.75	3.89	3.49	3.26	3.11	3.00	2.91	2.85	2.80	2.75	2.69	2.62	2.54	2.51	2.47	2.43	2.38	2.34	2.30
13	4.67	3.81	3.41	3.18	3.03	2.92	2.83	2.77	2.71	2.67	2.60	2.53	2.46	2.42	2.38	2.34	2.30	2.25	2.21
14	4.60	3.74	3.34	3.11	2.96	2.85	2.76	2.70	2.65	2.60	2.53	2.46	2.39	2.35	2.31	2.27	2.22	2.18	2.13
15	4.54	3.68	3.29	3.06	2.90	2.79	2.71	2.64	2.59	2.54	2.48	2.40	2.33	2.29	2.25	2.20	2.16	2.11	2.07
16	4.49	3.63	3.24	3.01	2.85	2.74	2.66	2.59	2.54	2.49	2.42	2.35	2.28	2.24	2.19	2.15	2.11	2.06	2.01
17	4.45	3.59	3.20	2.96	2.81	2.70	2.61	2.55	2.49	2.45	2.38	2.31	2.23	2.19	2.15	2.10	2.06	2.01	1.96
18	4.41	3.55	3.16	2.93	2.77	2.66	2.58	2.51	2.46	2.41	2.34	2.27	2.19	2.15	2.11	2.06	2.02	1.97	1.92
19	4.38	3.52	3.13	2.90	2.74	2.63	2.54	2.48	2.42	2.38	2.31	2.23	2.16	2.11	2.07	2.03	1.98	1.93	1.88
20	4.35	3.49	3.10	2.87	2.71	2.60	2.51	2.45	2.39	2.35	2.28	2.20	2.12	2.08	2.04	1.99	1.95	1.90	1.84
21	4.32	3.47	3.07	2.84	2.68	2.57	2.49	2.42	2.37	2.32	2.25	2.18	2.10	2.05	2.01	1.96	1.92	1.87	1.81
22	4.30	3.44	3.05	2.82	2.66	2.55	2.46	2.40	2.34	2.30	2.23	2.15	2.07	2.03	1.98	1.94	1.89	1.84	1.78
23	4.28	3.42	3.03	2.80	2.64	2.53	2.44	2.37	2.32	2.27	2.20	2.13	2.05	2.01	1.96	1.91	1.86	1.81	1.76
24	4.26	3.40	3.01	2.78	2.62	2.51	2.42	2.36	2.30	2.25	2.18	2.11	2.03	1.98	1.94	1.89	1.84	1.79	1.73
25	4.24	3.39	2.99	2.76	2.60	2.49	2.40	2.34	2.28	2.24	2.16	2.09	2.01	1.96	1.92	1.87	1.82	1.77	1.71
26	4.23	3.37	2.98	2.74	2.59	2.47	2.39	2.32	2.27	2.22	2.15	2.07	1.99	1.95	1.90	1.85	1.80	1.75	1.69
27	4.21	3.35	2.96	2.73	2.57	2.46	2.37	2.31	2.25	2.20	2.13	2.06	1.97	1.93	1.88	1.84	1.79	1.73	1.67
28	4.20	3.34	2.95	2.71	2.56	2.45	2.36	2.29	2.24	2.19	2.12	2.04	1.96	1.91	1.87	1.82	1.77	1.71	1.65
29	4.18	3.33	2.93	2.70	2.55	2.43	2.35	2.28	2.22	2.18	2.10	2.03	1.94	1.90	1.85	1.81	1.75	1.70	1.64
30	4.17	3.32	2.92	2.69	2.53	2.42	2.33	2.27	2.21	2.16	2.09	2.01	1.93	1.89	1.84	1.79	1.74	1.68	1.62
40	4.08	3.23	2.84	2.61	2.45	2.34	2.25	2.18	2.12	2.08	2.00	1.92	1.84	1.79	1.74	1.69	1.64	1.58	1.51
60	4.00	3.15	2.76	2.53	2.37	2.25	2.17	2.10	2.04	1.99	1.92	1.84	1.75	1.70	1.65	1.59	1.53	1.47	1.39
120	3.92	3.07	2.68	2.45	2.29	2.17	2.09	2.02	1.96	1.91	1.83	1.75	1.66	1.61	1.55	1.50	1.43	1.35	1.25
∞	3.84	3.00	2.60	2.37	2.21	2.10	2.01	1.94	1.88	1.83	1.75	1.67	1.57	1.52	1.46	1.39	1.32	1.22	1.00

Degrees of freedom for the denominator (v_2)